THE UNIVERSITY OF CHICAGO

DATA AND THEORY ON THE SPATIAL ECOLOGY OF AN INSECT-BACULOVIRUS INTERACTION ACROSS SCALES

A DISSERTATION SUBMITTED TO
THE FACULTY OF THE DIVISION OF THE BIOLOGICAL SCIENCES
AND THE PRITZKER SCHOOL OF MEDICINE
IN CANDIDACY FOR THE DEGREE OF
DOCTOR OF PHILOSOPHY

DEPARTMENT OF ECOLOGY AND EVOLUTION

BY
WILLIAM T KOVAL

CHICAGO, ILLINOIS
DECEMBER 2024

Copyright © 2024 by William T Koval

All Rights Reserved

For my parents

who gave me the world.

and for Paula

who made it come alive.

TABLE OF CONTENTS

LIST OF FIGURES

LIST OF TABLES

ACKNOWLEDGMENTS

I'm under no illusion that dissertations are the effort of an individual. This work has taken an enormous effort of intellectual and emotional labor from those who have supported me throughout my life and academic career.

I would first like to acknowledge my advisor, Greg Dwyer, who has created a research environment that not only supports but inspires the union of theory, data, and practice. My approach to research has been greatly shaped by this philosophy and I appreciate all of the time he has made for me to ensure that I have the tools to make this ideal a reality. I would not have been able to complete any of this research without his careful guidance and warm introduction to mathematical biology.

I also would like to acknowledge my thesis committee. I'd like to thank my committee chair, Sarah Cobey, who's computational lab handbook and wealth of knowledge allowed this work come to fruition. I would also like to thank Matthias Steinrüken, who was a great source of clarification and advice on tricky issues with mathematical writing. Finally, I'd like to thank Carlos Polivka for his guidance in making sure that my theoretical results stayed grounded in practical applications and for opening up his lab to me for conducting field work. This work would not have been possible without the tremendous efforts he made along with his research tema at the Wenatchee Pacific Northwest Research Station.

Next I need to thank the wonderful students in the Dwyer lab who have been colleagues, confidants, co-conspirators, and life-long friends. So many thanks to the spongy moth gang, Sophia Horigan, Bonnie Mendelson, Jiawei Liu, and Juan Santos Rosas, who have provided advice and friendship during hard times. I'd particularly like to thank Katie Dixon, who has been in the lab the entire time I have been. It is through her friendship, knowledge, and advice that I have been able to come this far. I will always be thankful to her for passing through the gauntlet of Douglas-fir tussock moth research first and for her grace in showing me the ropes.

Next I want to thank our wonderful collaborators. I would like to thank the tremendous field team who collected the data used in this study, namely Amy Gannon, Laurel Haavik, August Kramer, Chelsea Miller, and Kate-Lynn Logan. I'd also like to thank Mary Johnson and Luis Marmolejo who coordinated the package deliveries during a difficult year. Vanja Dukic always provided insightful feedback on all things statisitcs, and I want to thank her for being such a warm and brilliant person to work with. Mark Kot likewise provided great conversations to guide the integrodifference equations work, which would not have been possible without his expertise.

I would like to thank the ARCS Foundation, the American Museum of Natural History, and the Hinds Fund for providing research funds to accomplish this work. I was supported for three years by the National Science Foundation Ecology and Evolution of Infectious Diseases panel under grant DEB 2109774. I was also supported on the National Institutes of Health training grant for two years. I'd also like to thank the Research Computing Center and the Center for Research Informatics here at the Univeristy of Chicago for providing tremendous computational resources and IT services through Midway3 and RANDI, respectively.

I would also like to thank Jeff Wisniewski, Bonnie Brown, Susan Hu, Connie Homan, and Mike Guerra for a lot of their work behind the scenes. Thanks to Marcy Hochberg who offered administrative and emotional support. Many thanks to Audrey Aronowsky who guided me from day zero, when I arrived at Midway airport, through to today and made this an enjoyable journey with so much behind the scenes work. I'd like to thank UChicago Student Wellness Mental Health for providing counsel to get me through two crucial points in my life that allowed me to carry on.

I would like to thank the wonderful students of EE and the Darwinian cluster who made this a vibrant and fun place to work. Big thanks to my friends not yet mentioned: Megan, Laura, Hope, Laura, Santi, Ricardo, Deanna, Jacob, Lila, Abhimanyu, Sofia, Gwen, Brandon, Caroline, Caroline, Alex, Alex, Alex, and Hannah.

My family has been a solid source of support and source of questions related to biological fields I am nowhere near in. Thanks to my extended family, my sister Laura, and my parents; frequent calls and visits made the distance to you all feel a lot shorter. Thank you for letting me be myself around you and never failing to be there for me.

My thanks to Paula, my partner in all senses of the word, for being exceptionally brilliant, hilarious, mischievous, and caring. This couldn't have happened without you because there's no me without you.

ABSTRACT

Spatial structure influences ecological interactions but it is not well understood how ecological interactions drive spatial patterns across scales of observation. We combined spatial models at two scales to understand how spatial patterning results from host-pathogen interactions in the Douglas-fir tussock moth, *Orgyia pseudotsugata*, and what the consequences of spatial structure are for transmission rates and host heterogeneity. We first combine spatial infection rate data from multiple tussock moth populations with spatial transmission models to understand how limited dispersal drives pathogen dynamics and informs the extent of insect tree damage. We then assess how tree damage patterns observed at larger spatial scales can be explained by eco-evolutionary dynamics over longer time frames. We found that locally, patchy pathogen distributions generate hotspots of transmission that shape overall pathogen dynamics and increase the severity of tree damage caused by Douglas-fir tussock moth larvae. We observed that this spatial structure constitutes the majority of infection risk variation, but that accounting for the heritable proportion of infection risk variation in eco-evolutionary models was necessary to explain the accelerating waves of multiple interacting *O. pseudotsugata* populations over larger spatial scales. Therefore, both small-scale diffusion between trees and heritable host infection risk are important for determining the intensity and location of insect outbreaks at meta-population scales. Our research, founded in model comparisons that confront theory with data, represents a novel synthesis on Douglas-fir tussock moth disease ecology at two spatial scales and provides insight into general host-pathogen theory for understanding pathogen dynamics in nature.

CHAPTER 1

OVERVIEW

1.1 Spatial ecology across scales

A simple assumption often made to predict population changes over time is to assume that individuals mix perfectly and that spatial location is unimportant . It is nonetheless true that organisms exist in spatial contexts. The rates at which individuals interact with each other and the rates at which populations interact with each other are therefore not uniform (Shigesada and Kawasaki [1997], Hanski and Simberloff [1997], Okubo and Levin [2001]). Spatial ecology seeks to understand what level of detail is necessary to include in order to better represent population dynamics (Levin [1992], Chave [2013], Elderd et al. [2022]).

The rate at which individuals interact can vary due to limited dispersal, which results in the uneven distribution of individuals over space. Even though dispersal, a trait comprised of movement capacity and behavioral choices, is an action taken by individuals, it can also be understood as a statistical process (Skellam [1951], Durrett and Levin [1994]). For example, deterministic dispersal models like reaction-diffusion equations emerge from treating the collective behavior of individuals within an infinite population that has density over space (Shigesada and Kawasaki [1997], Okubo and Levin [2001]). As individuals move, their average dispersal is reflected at the population level, which can ultimately affect the average population dynamics and fundamentally alter ecological processes (Durrett and Levin [1994]). Further, unique to spatial models is the ability to explain range expansions (Williamson [1996], Kot et al. [1996]). Range expansions can occur for invasive species or for any species that has new access to environmental shifts or competition release that allows for populations to spread (Williamson [1996], Melbourne and Hastings [2009], Erm and Phillips [2020]). Even though these environmental or ecological factors open up available habitat for population spread, ultimately range expansions stem form dispersal capacity and spatial

structure (Shigesada and Kawasaki [1997]).

The uneven distribution of individuals over space can be due to solely limited dispersal, environmental differences that filter populations, or a combination of both (Hanski and Ovaskainen [2000], Abbott and Dwyer [2008], Severns et al. [2019]). Often, whether environment or dispersal is more important for determining the spatial distribution of populations depends on the scale of observation (Levin [1992], Real and Biek [2007]). At small spatial scales without environmental differences, ecological interactions and limited dispersal can lead to patchiness (Weiner and Conte [1981], Durrett and Levin [1994], Bolker and Pacala [1997], Dumonteil et al. [2013]). For example, competing species can coexist more readily in spatial models than in perfectly mixing models (Chesson [2000]). Space can also provide refugia for prey when interacting with predators (Crowley [1981], Chesson and Murdoch [1986]), more easily permitting the sustained cycles of predator-prey dynamics that otherwise would lead to stable populations or extinction. Introducing space in these models thus decreases the rate of interaction between different species and shifts the ecological dynamics, even in the absence of environmental differences (Hanski [1994], Shigesada and Kawasaki [1997]).

At larger scales, spatial patterns can be explained by a combination of both dispersal and environmental factors (MacArthur [1972], Williamson [1996], Real and Biek [2007]). For example, synchrony between neighboring population dynamics can be understood as a result of correlations in their variable environments, but dispersal can strengthen such effects (Peltonen et al. [2002], Abbott and Dwyer [2008]). Just as higher interaction rates can strengthen degrees of synchrony, alternating dynamics or wave-like patterns that are characteristic of asynchronous populations can be explained using limited dispersal (Shigesada and Kawasaki [1997]). Frequently, however, these explanations invoke non-linear ecological interactions rather than environmental correlates to explain spatial patterning (Crowley [1981], Chesson [2000], Bjørnstad et al. [2002], Severns et al. [2019]). For example, asynchronous

travelling waves can also occur at smaller scales, such as those that occur through the uneven mixing of reaction-diffusion systems used to describe predator-prey interactions (Shigesada and Kawasaki [1997], Okubo and Levin [2001], Sherratt [2001]). Therefore, it is known that the degree of spatial structure in the environment and amongst populations can generate synchrony or asynchrony, but syntheses across scales are rare.

Spatial patterns such as synchrony and travelling waves are commonly observed in nature (Shigesada and Kawasaki [1997]), and with repetition comes some level of predictability (MacArthur [1972]). It has therefore been the goal of spatial ecology to understand the sources and consequences of spatial structure that drive these patterns and, crucially, to determine the important levels of detail or scale of spatial observation to do so (Levin [1992], Wilson et al. [2019]). Often, the effects of spatial structure at various scales differ and the relevance of detail at each scale is case-specific (Chave [2013]). However, there is still a need for general theory of how spatial scales interact. Identifying the relationship between long-term, long-distance models and short-term, local models is necessary to determine how large scale patterns emerge from small scale interactions (Levin [1992]).

1.2 Structure in host-pathogen interactions

Host-pathogen interactions present interesting systems in which to address the role of spatial structure as they often show spatial patterning at large scales but depend on close individual-to-individual interactions (Real and Biek [2007], Wilson et al. [2019], Severns et al. [2019]). These systems possess population structure at various levels, such as host heterogeneity of infection risk, pathogen variability, and spatial structure (Hudson et al. [2002], Grenfell et al. [2004], Tack et al. [2012], Britton et al. [2020]). In diseases of wildlife and plants, host ecology and host traits can be altered by pathogen presence in the absence of spatial structure (Hudson et al. [2002], Wilson et al. [2019]). Pathogens have been shown to regulate population cycles observed in much of the host population biology (May and Anderson [1979],

Real and Biek [2007]). Thus, the ecological dynamics of hosts are fundamentally linked to their pathogens.

The theory of host-pathogen interactions is widely used in public health (Viboud et al. [2006], Cobey [2020]), agriculture (Severns et al. [2019]), wildlife management (White et al. [2018]), and silviculture (Mihaljevic et al. [2020]). There is a general understanding of how spatial structure can influence disease spread (Severns et al. [2019]), but the importance of spatial structure amidst other types of population structure is still unclear (Wilson et al. [2019]). Although to some extent the role of spatial structure has been explored in human disease systems, the more limited dispersal of plants and animals has led to a larger focus on spatial structure for wildlife disease (Severns et al. [2019]). Indeed, the idea of epidemic thresholds that consider well-mixing populations are thought to be less relevant due to lower levels of mixing and smaller populations in animal pathogens (Lloyd-Smith et al. [2005b]). Further, the mechanisms that cause some areas to show up-regulated pathogen transmission while other areas show low levels of transmission are difficult to disentangle (Brown et al. [2013b], Tian et al. [2018], Mancy et al. [2022], Vazquez-Prokopec et al. [2023]. Multiple modes of transmission and host heterogeneity can obscure the effects of spatial structure (Breban et al. [2009]). This is especially when environmental variability is invoked both the introduce spatial structure and alter transmission rates (Grenfell et al. [2001], Real and Biek [2007], Brown et al. [2013b]). Therefore, it is important to understand the role of spatial structure at multiple scales in the host-pathogen system of interest and to confront models with data in order to compare models at each scale (Wilson et al. [2019]).

Importantly, pathogens place high selective pressure on hosts and their immune systems, such that trait distributions shift during or after pathogen outbreaks (Dwyer et al. [2000], Grenfell et al. [2004]). In humans, the co-evolution of immune response and pathogen strains can be used to identify epidemiological dynamics (Gupta et al. [1998], Gog and Grenfell [2002]). Animal host infection risks also vary across individuals, and pathogens may place

stronger selective pressures on these host populations than in humans. As these evolutionary processes occur over ecological times scales, the altered interaction rates in spatial contexts can influence the traits of individuals (Dwyer et al. [2000], Grenfell et al. [2004]). However, the degree to which eco-evolutionary processes influence the spatial patterning of disease is unclear across scales (Wilson et al. [2019]).

1.3 The Douglas-fir tussock moth, *Orgyia pseudotsugata*, and its baculovirus

Insects are ideal model systems to explore host-pathogen interactions (Cory and Myers [2003], Elderd and Dwyer [2019]). Some of the first mechanistic transmission models were developed to explain the forest insect outbreak cycles using host-pathogen theory and continue to inform predictions of their population dynamics (May and Anderson [1979], Dwyer et al. [2000], Myers and Cory [2013], Dwyer et al. [2022]). Many Lepidopterans (species of butterflies and moths) are afflicted by pathogens that greatly alter population dynamics (Elderd and Dwyer [2019]). For example, a generalist fungus *Entomophaga maimaiga* has been shown to greatly reduce outbreaks of the invasive spongy moth, *Lymantria dispar*, since the introduction of the fungus in North America (Smitley et al. [1995], Liu et al. [2023]). While parasitoids and generalist predators have also been shown to be important for regulating Lepidopteran populations (Chesson and Murdoch [1986], Dahlsten et al. [1977], Bjørnstad et al. [2002], Dwyer et al. [2004], Hughes et al. [2015], a group of specialist viruses known as baculoviruses have been shown to fundamentally drive eco-evolutionary dynamics in multiple species (Cory and Myers [2003], Thézé et al. [2018].

Baculoviruses are a clade of specialists that are host-specific, evnironmentally-transmitted, and obligate lethal pathogens of many Lepidopteran species (Cabodevilla et al. [2011], Thézé et al. [2018]). The specific genus of baculoviruses that afflict Lepidopteran hosts are known as nucleopolyhedroviruses (NPV). Although there is some evidence that NPV baculoviruses can

infect multiple hosts, these are likely spillover events and transmission predominantly occurs within a single Lepidopteran species (Cory and Myers [2003]). As they are environmentally-transmitted, hosts are exposed to NPV particles, known as "occlusion bodies", by consuming contaminated material, either while emerging from contaminated eggs or while foraging on plants (Myers and Cory [2015], Cabodevilla et al. [2011]). Larvae are thus the only stage susceptible to the baculovirus infection, but pupae can also suffer NPV-induced mortality after having fed on contaminated material as larvae (Cory and Myers [2003]). Occlusion bodies are made of durable polyhedron protein shells that contain multiple virions, which open inside the basic environment of the insect gut (Cabodevilla et al. [2011]). Larvae have general innate immune response to baculoviruses, in which melanin globules bind foreign bodies to prevent viral proliferation (Wu et al. [2016]). If occlusion bodies are not bound by the innate immune system in the gut, however, virions enter insect cells to replicate within the nuclei (Cabodevilla et al. [2011]). Once a critical mass of cells have replicated the baculovirus, the cells rupture to release occlusion bodies into the environment through the host cadaver. Therefore acquired immunity does not occur if innate immunity is overwhelmed (Cory and Myers [2003], Myers and Cory [2013]).

The Douglas-fir tussock moth, *Orgyia pseudotsugata*, is a moth native to the conifer stands of western North America (Brookes et al. [1978]). Douglas-fir tussock moths reproduce annually, undergoing diapause as eggs during the winter. Eggs typically hatch in late May, with southern latitude populations hatching later and northern latitude populations hatching earlier (Dennis et al. [1986], Shepherd et al. [1988]). Larvae emerge to sync up with flush foliage presence on their preferred tree hosts: Douglas-firs (*Pseudotsuga menziesii*) and true firs,*Abies* spp. (Beckwith [1976], Mason [1996]). From late July (males) to early August (females), pupation occurs followed by adult emergence (Brookes et al. [1978]). As females of the species are flightless, mating occurs when flying male moths follow pheromone cues to encounter adult females (Mason et al. [1977]). Female moths then lay fertilized eggs onto

their own pupal casings and die on top of the egg mass.

Because females are flightless, Douglas-fir tussock moth individuals can only disperse as larvae. They do so through two mechanisms at two spatial scales. Larvae undergo long distance dispersal prior to feeding, as they produce silken strands to increase buoyancy if they do not quickly find foraging material (Mitchell [1979]). This behavior known as "ballooning" occurs only once upon hatch before feeding. Ballooning can thus lead to the population spread in a single generation, although the degree to which dispersal can shape population movement is contested (Mitchell [1979], Shepherd et al. [1988]). Larvae then can disperse between trees or amongst branches after ballooning, but this movement is greatly restricted in comparison to the distances travelled after hatch.

Although tussock moth populations are frequently at undetectable densities, populations will periodically reach high, outbreaking densities (Mason [1970, 1996]). During high-intensity insect outbreaks, in which insect densities are increased by several orders of magnitude, larval herbivory can lead to extensive tree damage and, ultimately, tree mortality (Shepherd et al. [1988], Alfaro and Shepherd [1991], Mason et al. [1997]). Therefore, tussock moth populations are monitored as a target for pest management by the US Forest Service. The baculovirus specializing on Douglas-fir tussock moth, *Op*NPV, is therefore both observed by forest managers and used in integrated pest management strategies (Hughes and Addison [1970], Williams and Otvos [2005]). As a bio-control agent, the NPV baculovirus isolate known as Tussock Moth Bio-control 1 (TMB-1) is occasionally sprayed aerially on outbreaking Douglas-fir tussock moth populations (Mihaljevic et al. [2020]). The efficacy of TMB-1 and identifying the scenarios when it would be most useful, however, is still an active area of research (in prep). This is particularly complicated by the issue of identifying when and how quickly tussock moth populations would otherwise collapse due to natural baculovirus outbreaks (Mason [1996]).

One factor that remains uncertain for identifying the course of Douglas-fir tussock moth

epizootics, the epidemics of animals, is the role of spatial structure. Despite early work on larval dispersal and baculovirus spread (Dwyer [1992]), no studies have attempted to apply spatial models to tussock moth infection rate data in natural populations, nor have any studies attempted to understand the spatial patterning of host populations at meta-population scales using transmission models. It is well-understood that Douglas-fir tussock moths possess population structure through variable infection risk across individual hosts, but it is unknown how the infection risk distribution can be dissected into intrinsic infection risk and spatially-structured interaction rates (Mihaljevic et al. [2020], Elderd and Dwyer [2019], Dwyer et al. [2022]). Although investigated experimentally in other Lepidopterans (Dwyer and Elkinton [1995], Parker et al. [2010]), this question has yet to be investigated using spatial transmission models, leaving the role of spatial structure in host infection risk heterogeneity unclear.

1.4 Chapter summaries and conclusions

In Chapter 2, we combined infection rate data over space with spatial transmission models to understand the most important factors for predicting the spatial patterns of infection. We generated a spatially referenced dataset of baculovirus infection rates in several populations of Douglas-fir tussock moth and compared a suite of spatial disease models to explain our infection data. The best model, a novel reaction-diffusion system accounting for host infection risk heterogeneity, demonstrated that transmission hotspots emerge from the initial pathogen distribution, but that host dispersal is required to understand the transition of low-intensity transmission coldspots into late-season transmission hotspots. In addition to the indirect observation of these bimodal sub-epizootics, we show that environmental stochasticity and agent-based models provide no predictive performance gains over the deterministic reaction-diffusion model with random initial conditions, challenging the contemporary emphasis on stochastic modelling. Our new understanding of shifting transmission hotspots has impli-

cations for the management of Douglas-fir tussock moth through the ability of our spatial larval herbivory intensity projections to predict defoliation tree damage observed during the study.

In Chapter 3, we developed eco-evolutionary host-pathogen models to understand the spatial patterning of defoliation and the changes in host infection risk heterogeneity over time. We built integrodifference models that generated accelerating waves due to either individuals with exceptional long-distance dispersal or evolving host infection risk at the wave front. Our eco-evolutionary models of host infection risk variation were able to better explain the spatial distribution of outbreak density tussock moth populations than exceptional dispersal. We found that such evolutionary models could reproduce defoliation patterns, even in the wake of invasion. We also determined that intermediate heritability of infection risk variation was sufficient and necessary to explain defoliation data behind the wave front. Importantly, we demonstrate that dispersal between fluctuating, asynchronous populations contributes to the maintenance of host infection risk variation under balancing selection. Our research thus presents one of the first studies to track host trait variation during an accelerating wave in a host-pathogen system.

We conclude that both heritable host heterogeneity and imperfect mixing at local scales drives local defoliation severity and the spatial patterning of insect outbreaks at multiple scales. Both small-scale diffusion between trees and long-distance dispersal over the landscape are important for determining both the intensity and location of insect outbreaks. However, the importance of effects by individual hosts, either through exceptional long-distance travel at meta-population scales or through stochastic transmission at local scales, proved to be unnecessary detail for understanding the spatial patterns of tussock moth populations. Our work, driven by model comparison and empirical data, thus represents a synthesis of Douglas-fir tussock moth disease ecology at two spatial scales.

CHAPTER 2

DATA AND THEORY SHOW THAT HOST DISPERSAL ALONE MEDIATES SHIFTING TRANSMISSION HOTSPOTS

2.1 Introduction

The theory of host-pathogen interactions provides crucial tools for managing animal and plant diseases, principally in the form of mathematical models that can be used to predict or explain disease dynamics (Keeling and Rohani [2008], Mollison [1995]). A significant branch of this work has demonstrated that spatial structure can play a pivotal role in shaping pathogen spread (Durrett and Levin [1994], Peltonen et al. [2002], Murray et al. [1986], Lalley [2009], Wood and Thomas [1996]). Theory has shown that spatial structure and limited dispersal similarly alter average pathogen dynamics in a variety of disease systems, with consequences for the estimation of critical metrics such as the effective reproductive number and pathogen persistence times (Tkachenko et al. [2021], Britton et al. [2011], Wood and Thomas [1996]). Even in systems with high levels of mixing, such as directly transmissible human diseases, the effects of spatial structure are often easily detectable (Grenfell et al. [2001], O'Neill et al. [2000], Giles et al. [2020]). Spatial structure may thus be important for understanding disease spread in general and particularly important for understanding the environmentally transmitted pathogens of plants and animals, as hosts have more limited mobility and heterogeneous environments strongly alter transmission rates (Dwyer and Elkinton [1995], Deeth and Deardon [2016], Bonnell et al. [2016]). However, direct applications of spatial theory to disease spread in nature remain limited, and so the utility of spatial epidemic theory for explaining disease data remains uncertain.

The study of spatial disease dynamics is constrained by the logistical challenges of collecting spatial disease data. For example, both continuous and discrete spatial models predict that epidemics will spread through travelling waves (Bjørnstad et al. [2002], Grenfell et al.

[2001], Dwyer [1992]), but empirical evidence of these patterns requires the observation of pathogen spread into unexposed populations. Such observations using temporal infection rate data are rare, with notable exceptions such as the COVID-19 pandemic (Tkachenko et al. [2021]), Dengue serotype replacements (Harish et al. [2024], Teoh et al. [2013], Vazquez-Prokopec et al. [2023]), or novel chytrid invasions (Longo et al. [2023], Lips et al. [2006]). Furthermore, endemic disease models predict that pathogen dynamics should at least sometimes show synchrony over space (Tian et al. [2018], Peltonen et al. [2002], Woods et al. [1991], Boender et al. [2014]), but analyzing the extent of spatial synchrony in pathogen dynamics requires that infection data is collected at the same scales over which hosts disperse (Deeth and Deardon [2016], Dwyer and Elkinton [1995]).

To provide a framework for identifying pathogen establishment and the extent of infection rate synchrony over space, we collected a spatially referenced data set of pathogen dynamics over time in an insect host-pathogen system. We estimated infection rates across space in multiple populations of the Douglas-fir tussock moth, *Orgyia pseudotsugata*, each of which were undergoing epizootics (the epidemics of animals) of a fatal, environmentally transmitted baculovirus. Within each study population, we sampled larvae, the only life stage susceptible to the baculovirus, and monitored their infection status at time of collection (Mason [1977], Otvos et al. [1989]). As larvae readily move between branches but more rarely move between trees, we expected that spatial structure at the tree scale would strongly affect baculovirus dynamics (Mason [1977]). We therefore quantified infection rate variation over space by recording the tree of origin for each larva.

Another obstacle to understanding disease data using spatial theory is the need for computationally intensive methods with which to compare spatially explicit models with spatially variable data (He et al. [2010], Lessler et al. [2017], Ensoy et al. [2013]). While non-spatial models of pathogen transmission can often provide reasonable approximations to pathogen dynamics (Keeling and Rohani [2008]), it remains unclear whether non-spatial models can

explain spatially explicit data sets. Due to the computational challenges involved in the quantitative comparison of spatial models to data, mechanistic, spatial disease models are rarely used to analyze spatial data sets. Instead, differences between sub-population infection rates are recorded and compared to environmental covariates using static, linear regression models (Dowdy et al. [2012], Boender et al. [2014], Lessler et al. [2017]). This is particularly true of the literature addressing the importance of areas with increased infection rates known as transmission "hotspots". Hotspots are widely invoked to explain the inherent variation of pathogen dynamics and receive intense speculation for disease management, but establishing causation for their presence or absence is difficult with standard approaches (Lessler et al. [2017], Brown et al. [2013b]). However, statistical regression analyses are increasingly being supplemented by the use of high-performance computing, which allows for the parameterization and simulation of spatial transmission models that can provide deeper insights into the mechanisms that drive epidemiological data (Touloupou et al. [2020], O'Neill et al. [2000], Mancy et al. [2022], He et al. [2010], Bretó et al. [2009], Ensoy et al. [2013]). Here, we took a mechanistic spatial modelling approach to understand the importance of transmission hotspots in baculovirus dynamics.

We conducted a formal, quantitative assessment of the performance of multiple spatial models, we built competing spatial models fitted to our spatial infection rate data. Each of our models makes different assumptions about the importance of stochasticity, spatial structure, and limited dispersal. In contrast with the abundance of non-spatial disease models for forest insects (Peltonen et al. [2002], Bjørnstad et al. [2002], Dwyer et al. [2000]), few studies have explored the effects of small-scale spatial dynamics in these systems (but see Dwyer and Elkinton [1995], Dwyer [1992]). Most spatial studies of forest insects have instead focused on large scales, assuming high levels of local mixing within continental-scale meta-population models (Myers and Cory [2013], Peltonen et al. [2002]). Tracking pathogen infection rates at the scale of individual trees allowed us to instead test whether

spatial models that incorporate dispersal at the scale of daily larval movements are able to reproduce the observed spatial variation in baculovirus infection rates.

Studies of pathogen dynamics have only recently begun to rigorously confront spatial models with data (Mancy et al. [2022], Tian et al. [2018], Ensoy et al. [2013], Koeijer et al. [2020], Boender et al. [2014]). Despite this progress, but infection rate data is rarely used to compare stochastic spatial models to one another. Our work therefore represents what is, to our knowledge, the first model comparison that quantifies the relative importance of spatial structure and stochasticity on the dynamics of a host-pathogen system in nature. Moreover, because the baculovirus is important for the control of Douglas-fir tussock moth outbreaks, we aim to show how a general understanding of spatial disease spread can generate useful models for controlling forest pest populations.

2.2 Methods

2.2.1 Data collection

The Douglas-fir tussock moth, *Orgyia pseudotsugata*, is a defoliator of western North American conifer stands. Frequently at undetectable densities, Douglas-fir tussock moth populations periodically rise to high densities that are easily detected and sampled. High density tussock moth outbreaks are typically terminated by epizootics of specialist baculoviruses that are host-specific, environmentally-transmitted, and obligately lethal. However, high density populations can still persist after low-infection epizootics.

We identified seven Douglas-fir tussock moth populations undergoing outbreaks through egg mass surveys and flight trap counts collected by ongoing surveillance projects of the US Forest Service (figure 2.1). We selected our seven study populations based on the detectable presence of adult Douglas-fir tussock moth males in the fall of 2019 (figure 2.1). All detectable populations had some level of baculovirus presence, regardless of host population

density. Pine 3 (PIN3) in Wallowa-Whitman National Forest, Oregon and Cracker Jack Mine (CRKJ) in Payette National Forest, Idaho had similar mortality trends, despite a distance of approximately 30 km. Two sites in Frenchtown Face (FR01, FR12) in Lolo National Forest, Mt. Jumbo (MTJM), and Barmeyer (BARM) also seemed to be a grouping of similar trends, but these sites were far closer to each other in the Missoula, Montana area 2.3. Chesaw (CHSW) in the Okanogan National Forest, Washington was a low-level outbreak with limited mortality. We were unable to identify populations ahead of the larval season for sampling unless males were detected in flight traps the preceding fall, which restricts the set of dynamics that we can capture. However,this still allowed for the inclusion of the Chesaw study population that was near the estimated host disease density threshold and we were able to estimate the variable initial pathogen conditions that generated different temporal dynamics for the higher density host sites.

Transmission begins at the start of the summer when hatching tussock moth larvae consume egg mass material contaminated with baculovirus occlusion bodies. In our models, we consider these exposed first instars to be the initial cadaver densities that instigate within-season transmission. We sampled larvae in our seven study sites over the course of June to August, which reflects the time period when larvae are present after hatch but have not yet pupated or died during epizootic population collapse (figure 2.3). Larvae were collected by using a beat sheet to expel larvae from branches at breast height in the mid crown of conifers suitable for larval growth Mason [1977]. To avoid the effects of larval removal, we did not necessarily sample the same trees over the course of our study, but all sampled trees in a given study population were within a 10m radius of one another.

We selected trees at random within a 10 meter radius of one another to form a tree cluster comprising a time point sample within a given study population. As we selected these trees at random, sampling three branches from each tree, sometimes individual trees yielded no insects. We continued sampling until finding three trees that possessed insects,

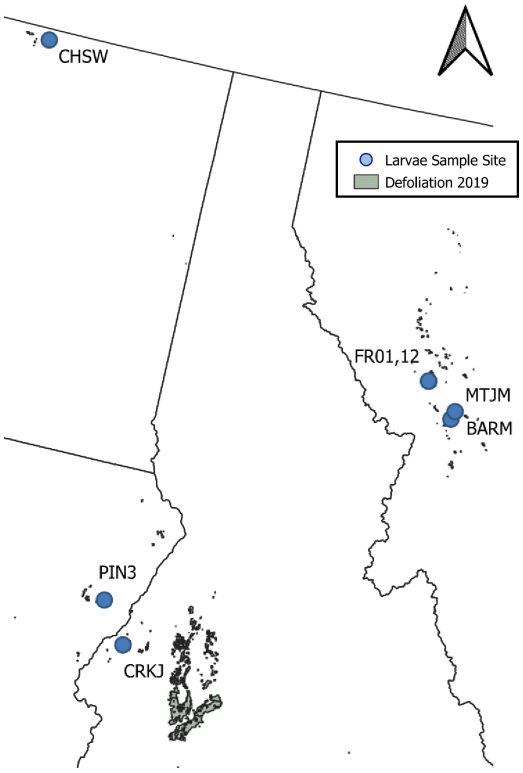

Figure 2.1: Map of our seven study sites in USFS Regions 1 and 6. Defoliation of the previous year is shown in green, denoting proximity to previous Douglas-fir tussock moth outbreaks.

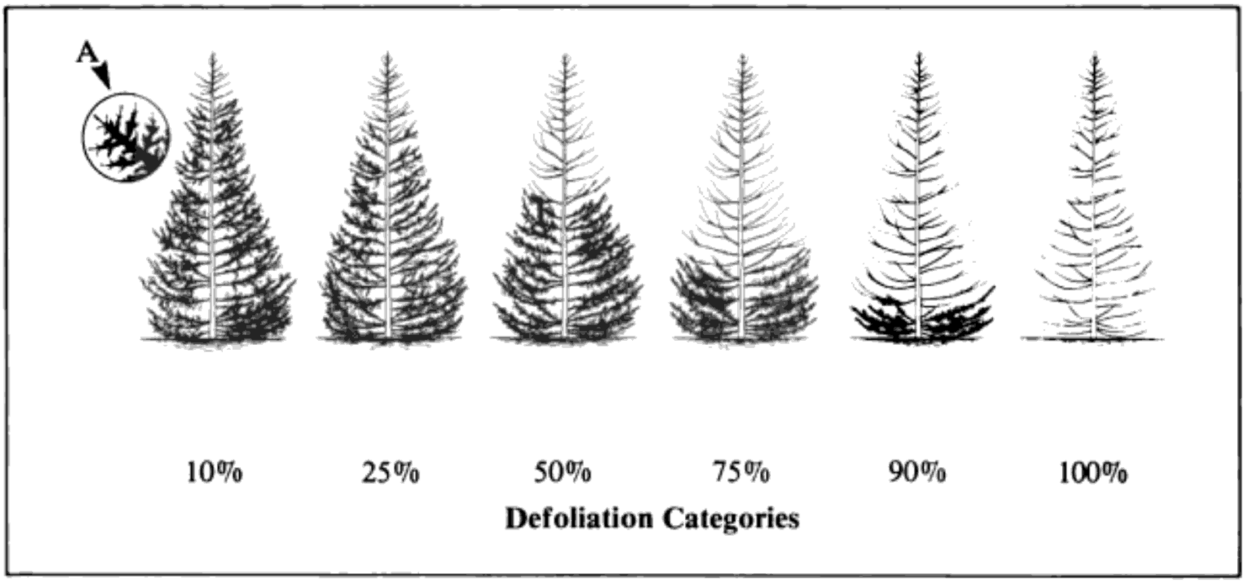

Figure 2.2: Reproduced figure from Brookes et al. [1978], showing the categorical defoliation severity levels.

to a maximum of ten trees per tree cluster. We always sampled a minimum of three trees per tree cluster for the time point sample of a given study population, collecting four time points from each of our seven study populations in total.

Throughout our infection rate study, we collected categorical defoliation severity data from each tree sampled for larvae, where the field team noted either 0%, 10%, 25%, 50%, 75%, or 90% following figure 2.2 (reproduced from Brookes et al. [1978]). the maximum observed severity level on any given tree in our study was 75%.

2.2.2 Small-scale spatial transmission models

Our models made varying assumptions about host and pathogen mobility, spatial structure, stochasticity, and host heterogeneity in susceptibility. These component mechanisms were included in isolation and in combination so that we could identify the most important drivers of pathogen dynamics in our spatial infection data.

We began with a non-spatial ordinary differential equation system (ODE) model as a plausible null alternative model against which to test our spatial models. The non-spatial

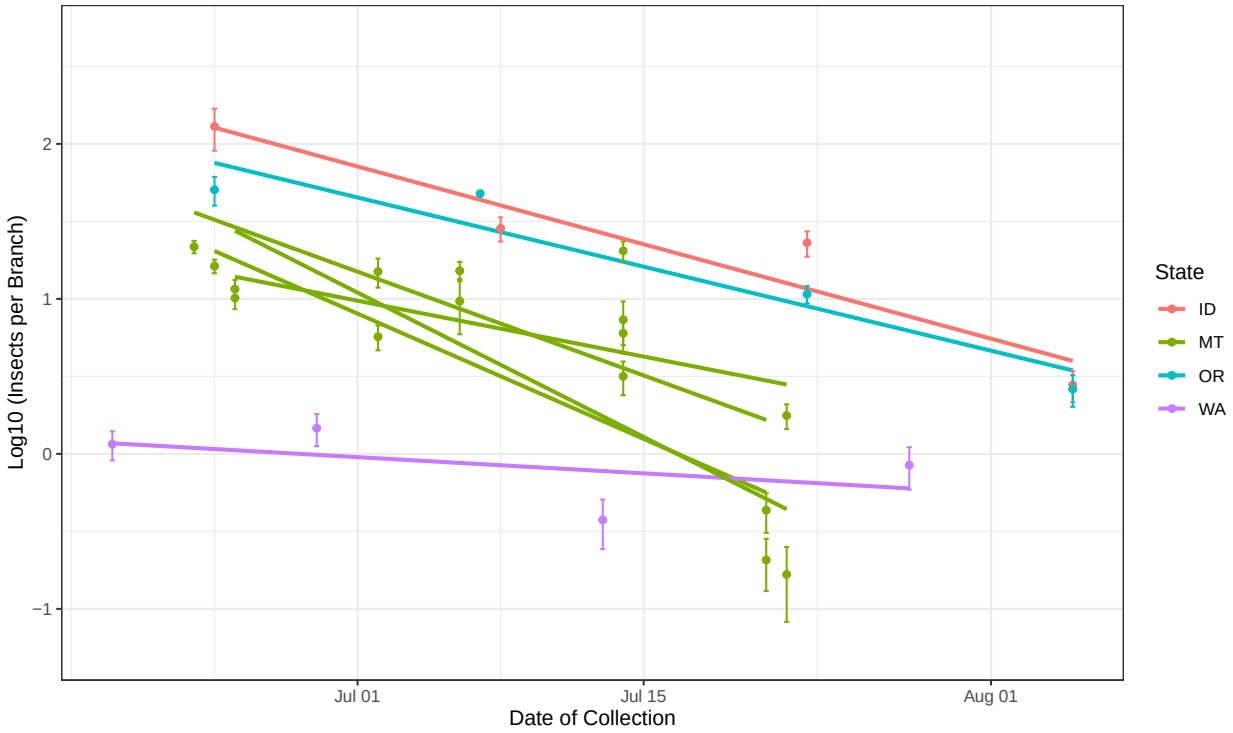

Figure 2.3: Estimated log insect branch density grouped by state, with population collapse due to baculovirus epizootics shown as linear models.

model is an $SEIR$ model from human epidemiology (equations 2.1-2.4, Keeling and Rohani [2008], Mihaljevic et al. [2020]).

$$\frac{dS}{dt} = -\bar{\nu} S P \left(\frac{S(t)}{S(0)} \right)^{C^2} \tag{2.1}$$

$$\frac{dE_1}{dt} = \bar{\nu} S P \left(\frac{S(t)}{S(0)} \right)^{C^2} - m\delta E_1 \tag{2.2}$$

$$\frac{dE_i}{dt} = m\delta E_{i-1} - m\delta E_i \qquad i = 2, ..., m \tag{2.3}$$

$$\frac{dP}{dt} = m\delta E_m - \mu P. \tag{2.4}$$

Here, susceptible hosts $S(t)$ that become infected move through a series of non-infectious exposed classes $E_{1..m}(t)$ until dying and becoming infectious cadavers $P(t)$, which contaminate foliage to transmit the baculovirus to feeding uninfected host larvae and then decay at rate μ. As there is no acquired immunity in this system, and there is only one generation per year, the density of susceptible hosts never increases. A key component of all our models is that we allow susceptible hosts $S(t)$ to vary in their infection risk. The mean infection risk $\nu(t)$ at time t decreases over the epizootic because hosts with higher risk are removed through infection sooner. The coefficient of variation C determines the shape of the infection risk distribution, with higher values generating a more skewed distribution. Using a moment closure approximation of the changing distribution of individual heterogeneity over time, we assume that shape parameter C is constant (Appendix A).

The non-spatial model assumes that dispersal is sufficiently high such that spatial structure has no effect on pathogen dynamics. To instead allow for spatial structure, we began with the opposing extreme case in which initial conditions varied over space, but dispersal was low enough to be neglected. The resulting model consists of multiple independent ODEs that were arranged spatially but that were not connected by dispersal. For this model, and for all of the spatial models, we initialized host and pathogen populations by assigning

integer densities to each grid point according to a multinomial distribution. Because the initial host and pathogen densities had equal probability over space, the models assume no overdispersion at the outset of the epizootic.

To allow for a full consideration of spatial structure and host dispersal, we next constructed a version of the $SEIR$ model in which larvae diffused between spatial locations. Because the mean infection risk $\nu(x,t)$ changes as a function of local host $S(x,t)$ and pathogen $P(x,t)$ densities, larval dispersal can affect the spatial distribution of mean infection risk $\nu(x,t)$ over time. We therefore derived a spatial reaction-diffusion model that accounted for the effects of larval dispersal on mean infection risk using a spatial moment closure approximation (Appendix A).

Previous work using the non-spatial form of the moment closure approximation showed that the mean infection risk $\nu(t)$ decreases according to a convenient analytical solution as a function of coefficient of variation C and the fraction of hosts $S(t)$ surviving, $\nu(t) = \bar{\nu}\left(\frac{S(t)}{S(0)}\right)^{C^2}$ (equation 2.1). In contrast, the effects of host movement in the reaction-diffusion model are sufficiently complicated that the model instead requires a separate equation to describe the changes in average infection risk $\nu(x,t)$ over space and time. Unusually, this equation includes a cross-diffusion term, such that

$$\frac{\partial S(x,t)}{\partial t} = -\nu SP + D\frac{\partial^2 S}{\partial x^2} \tag{2.5}$$

$$\frac{\partial \nu(x,t)}{\partial t} = -\nu^2 C^2 P + \frac{D}{S}\left[S\frac{\partial^2 \nu}{\partial x^2} + 2\frac{\partial \nu}{\partial x}\frac{\partial S}{\partial x}\right]. \tag{2.6}$$

This model allows for non-zero, limited dispersal. The diffusion equations for exposed classes are closely analogous to the equation 2.5 for the susceptible host class and are therefore not shown here. The spatial models with dispersal have periodic boundaries that represent a 2-dimensional slice of the forest canopy. The 2D simulation more realistically reflects how

we collected our data at breast height within each study population.

In addition to making different assumptions about the importance of host dispersal and spatial structure, we also made different assumptions about sources of stochasticity. We first allowed for environmental stochasticity, the random fluctuations that affect all individuals in a population. To do this, we multiplied the transmission rate $\bar{\nu}$ by a coefficient $\exp \epsilon_\tau$ for each day τ. The coefficients $\exp \epsilon_\tau$ were drawn from a log-normal distribution that had an expectation of one and variance term σ. In an effort to describe the relationship between average host and pathogen densities quantitatively, Mihaljevic et al., 2020 Mihaljevic et al. [2020] developed a non-spatial, mechanistic transmission model that assumed infection rate variation arose from sampling error and environmental stochasticity added to equations 2.1-2.4, which we here use as our non-spatial null model.

To next allow for demographic stochasticity, the random events that befall individuals, we constructed agent-based models that tracked individual life histories within the total population. In contrast to the PDE models, which describe individual variation using a continuous distribution, agent-based models are exact simulations of heterogeneous infection risk in a discrete population. We therefore assigned individual hosts their own infection risk values. Because infectious cadavers consist of a large number of infectious virion particles known as "occlusion bodies", we also included hybrid models that tracked susceptible and exposed hosts as individuals but assumed infectious cadavers to be infinitely divisible densities rather than countable individuals. For each model variant, we considered implementations with or without environmental stochasticity.

We then fit the models using a Markov chain Monte Carlo Gibbs sampler (MCMC). To maximize computational efficiency, we used iterative PCA-adjusted proposal distributions that accounted for posterior parameter correlations (Appendix B, Kennedy and Dwyer [2018]). To compare the predictive ability of different models to explain our spatial infection data, we used a statistical model comparison technique known as Pareto-smoothed impor-

tance sampling leave-one-out cross-validation (PSIS-LOO-CV, see Table 2.1). Using PSIS-LOO-CV through the `loo` package in the programming language `R` (Vehtari et al. [2024a]), we systematically validated each model by excluding one data point at a time and calculating the probability density of that data point conditioned on the rest of the data (Vehtari et al. [2017]). The resulting expected log pointwise predictive density (ELPD) allowed us to quantify how well our current data on spatial infection rates would generalize to future data. The ELPD information criterion for model comparison quantifies the average predictive accuracy of each model while PSIS uses the posterior variance of the log predictive density to reduce bias in ELPD estimation. PSIS-LOO-CV therefore provides a comprehensive performance evaluation that is more robust than the parameter penalty of BIC or the variance penalty of WAIC, even in the case of weak priors and influential data points (Appendix B, Vehtari et al. [2024b, 2017]).

2.2.3 Defoliation regression models

In order to have a predictor for defoliation observed on each tree in our study populations, we calculated the integrated host density over time

$$H(\tau) = \frac{1}{n}\sum_{i=0}^{n}\int_0^{\tau}(S(i,t)+E(i,t))dt \tag{2.7}$$

for each of n discretized spatial grid points. In order to arrive at the posterior distribution of herbivory intensity $\pi(H(\tau))$, we drew 150 random samples from the transmission parameter posterior $\pi(\vec{\theta}$ and calculated $H(\tau)$ for each 64 realizations across a grids search of initial conditions combinations. These values of $H(\tau = 40)$ are shown in figure 3A of the main text. We then constructed linear models of the form

$$H(\tau) \sim \bar{\nu} * C * \bar{S}(0) * \bar{P}(0) * \tau, \tag{2.8}$$

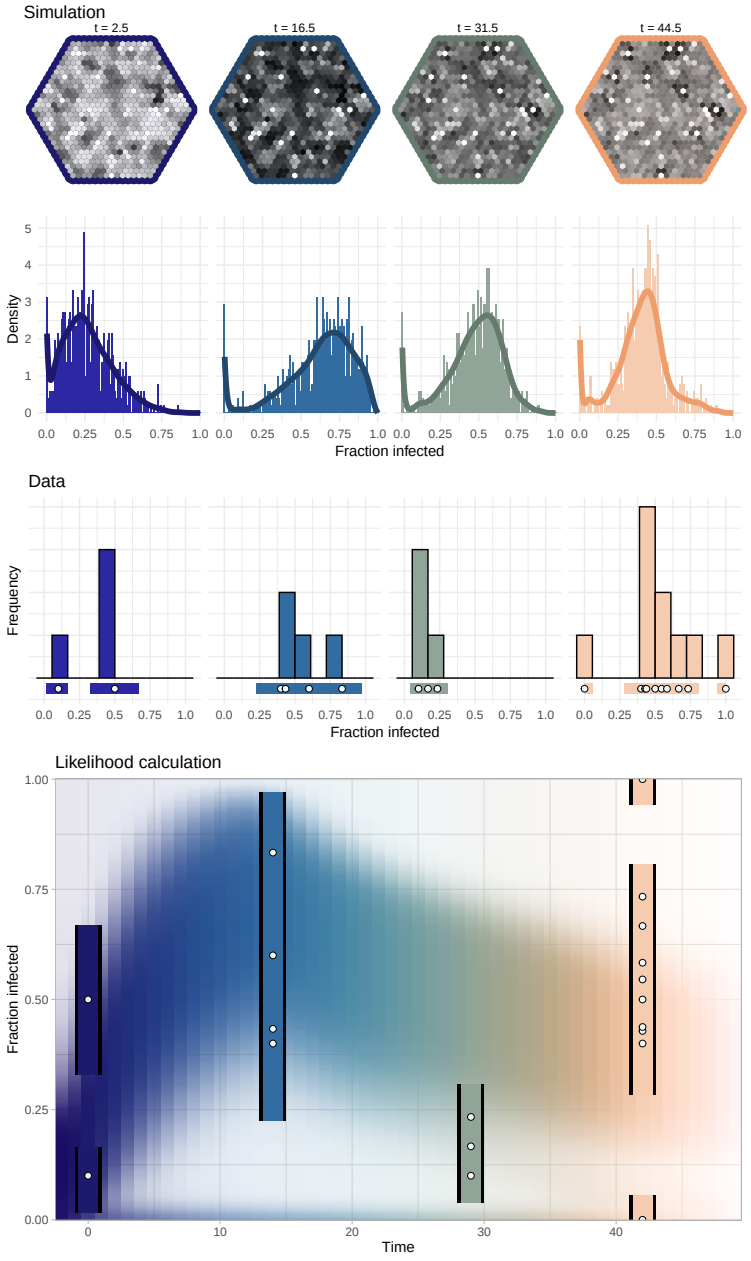

Figure 2.4: Conceptual figure showing the likelihood calculation approach. Top panels show the spatial simulation where each point is an individual tree. Histograms then show the distribution of fractions infected at each of the four likelihood score evaluation time points, with kernel density estimator $K(i)$ overlayed. The observed data from one study population is then shown in the third row as a histogram with empirical kernel density estimators of high probability shown as bars around singular data points. Data and the continuous time kernel density estimator are then plotted jointly to represent the jernel-binomial likelihood function described in detail in Appendix B

to integrate over simulations and posterior draws. The linear models of $H(\tau)$ captured the majority of the variation over the posterior ($R^2 = 0.98$). We next selected 124 independent samples from the posterior for initial conditions and transmission parameters within each study site, using the maximum integrated auto-correlation time across chains to determine sample size. We then used the linear model from equation 2.8 to generate expected values $H(\hat{\tau})$ for each study site over time, where $\hat{\tau}$ is the time of observation based on sample time and the fitted time of first observation t_0 for each study site.

We next constructed logistic regression models using the expected herbivory intensity $H(\tau)$ and time of observation for each sample time $\hat{\tau}$ as predictors. For each data point, which represented either the percent of foliage consumed (severity) or whether a tree had any defoliation present (extent), we therefore had 124 ($H(\hat{\tau})$) predictor values in order to integrate over the entirety of the posterior $\pi(H(\hat{\tau}))$. We compared the BIC scores for each individual model posterior draw (figure B.11) to determine quantitative differences in predictive power. We likewise compared a logistic regression model in which we modeled severity and extent as functions of cumulative insects sampled, generating an analogous approach for calculating $H(\tau)$ empirically. We excluded study site FR01 from all defoliation regression models, as defoliation from the previous year was included in the severity estimates and values were therefore indeterminately inflated for the whole time series.

2.3 Results

The average infection rates in our seven study populations were similar to those observed in previous insect-baculovirus studies (Woods and Elkinton [1987], Otvos et al. [1989], Mihaljevic et al. [2020], Woods et al. [1991]). As is typical of baculovirus epizootics, infection rates consistently increased during the early larval season, whereas late-season infection rates were more variable across populations (figure 2.5, Woods and Elkinton [1987]). The high peak infection rates and variable late-season trajectories that we observed can be at least quali-

tatively explained in terms of average larval densities, where study sites with higher larval densities tended to have a more rapid population collapse (figure 2.3, Woods and Elkinton [1987], Woods et al. [1991], Otvos et al. [1989]).

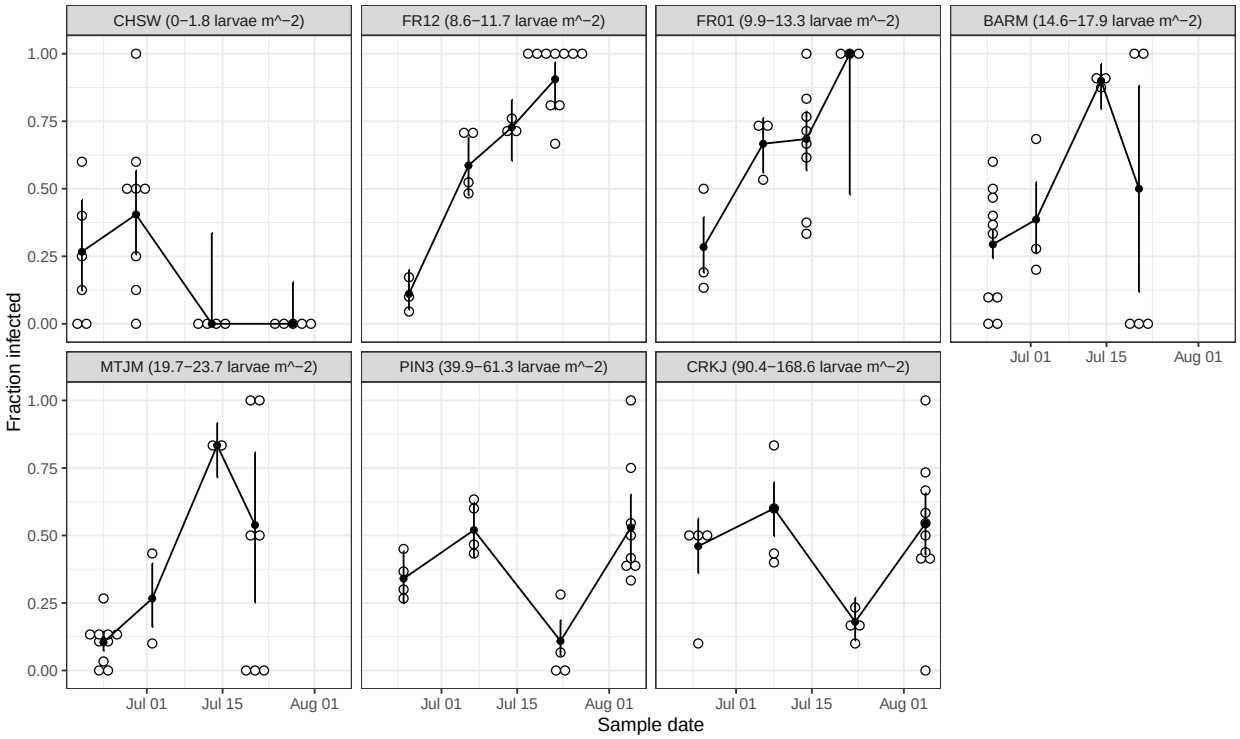

Figure 2.5: Mean fraction infected (black points and lines) and binomial confidence intervals (error bars) and tree-level infection rates (white circles) over time in our seven study populations. The seven study populations are arranged by increasing observed initial average larval densities, with the site name shown and then the branch density given in parentheses. Larval densities at the start of the season ranged from approximately 1 larva per m^2 (CHSW, top left) to approximately 135 larvae per m^2 (CRKJ, bottom right).

As a result, the non-spatial model with environmental stochasticity provides a reasonable fit to our data (figure 2.6), as it did in Mihaljevic et al. [2020]. This result quantitatively demonstrates the importance of average initial host and pathogen densities in explaining a significant portion of the variation in baculovirus infection rates (Mihaljevic et al. [2020], Woods and Elkinton [1987]).

2.3.1 Transmission hotspots and host dispersal drive pathogen dynamics

In contrast to previous studies explaining variation over pooled, spatially averaged infection rates, however, the models needed to explain the variation in baculovirus infection rates across trees to have strong predictive performance. Our spatially referenced data allowed us to show that spatial models indeedprovide a much better explanation for our data, such that the ELPD difference between the best model and the non-spatial model is $\widehat{\Delta\text{ELPD}} = -24.21 \pm 8.21$ (table 2.1). This large difference between the ELPD estimates demonstrates the strong predictive performance of the best spatial model relative to the non-spatial model (Appendix B, Vehtari et al. [2017]). The best model is the deterministic reaction-diffusion model, which explains variation around the mean infection rate by invoking a random initial distribution of susceptible hosts and infectious cadavers across space, in combination with modest amounts of larval host movement between spatial locations. We therefore conclude that when hosts have limited mobility, spatial models are likely to provide substantially better explanations for pathogen dynamics than non-spatial models.

The spatial models provide better explanations for our data because they easily replicate the bimodal pattern of sub-epizootic infection rates over space, which cannot be easily detected from infection rates that are averaged across trees. Projections from the best spatial model show that infection rates diverge across trees, where some spatial locations in an epizootic are transmission hotspots that experience high-intensity sub-epizootics, while others are coldspots that experience low-intensity sub-epizootics (figure 2.6). Because the estimated host disease density threshold is low relative to observed and posterior larval densities, whether or not a location in a spatial simulation will be a transmission hotspot depends on the initial pathogen distribution. Nevertheless, trees that start out as transmission coldspots can have late-season infection rate increases due to exposed hosts dispersing from early season transmission hotspots with high densities of infected larvae. Due to these dispersal-mediated hotspot shifts, the projected overdispersion of infection rates in the

spatial models more closely matches the overdispersion of our infection data (figure B.1), mechanistically demonstrating the improved ability of spatial models to explain infection rate variation.

The effect of dispersal-mediated delayed infection is most obvious in the case of our second-highest density study population, which showed the strongest divergence and sharpest increases of infection rates in coldspots that became late-season hotspots (figures 2.6, SB.6). Importantly, however, we can also distinguish study sites where this late-season shift did not occur. In our highest density site, which had a higher estimated initial pathogen density and therefore a more spatially uniform initial pathogen distribution, the spatial model projected that there were only a few coldspot sub-epizootics. Thus, the infection rates over space in our highest-density site were mostly small deviations from a single high-intensity average infection rate. Although the non-spatial model projections, by the nature of lacking bimodality, also showed that infection rates across realizations were small deviations from the average for our highest density population, the spatial model projections still had lower variation across realizations, which visually demonstrates the improved performance of the spatial models as quantified by LOO-CV (figure 2.6).

2.3.2 Stochasticity worsens predictive performance

Like the best model, the second-best model included space, but, in contrast, did not allow for host movement between spatial locations, instead explaining infection rate variation by invoking environmental stochasticity. Although the difference $\widehat{\Delta\text{ELPD}} = -2.31 \pm 3.26$ from the best model is substantial, the relatively large standard error of differences yields a confidence interval that overlaps zero, meaning that the data cannot easily distinguish between the second best model and the best model, the deterministic PDE (Piironen et al. [2020], Yates et al. [2023]). However, because this model assumes that dispersal can be neglected, it cannot reproduce the late-season infection rate increases that occurred in the

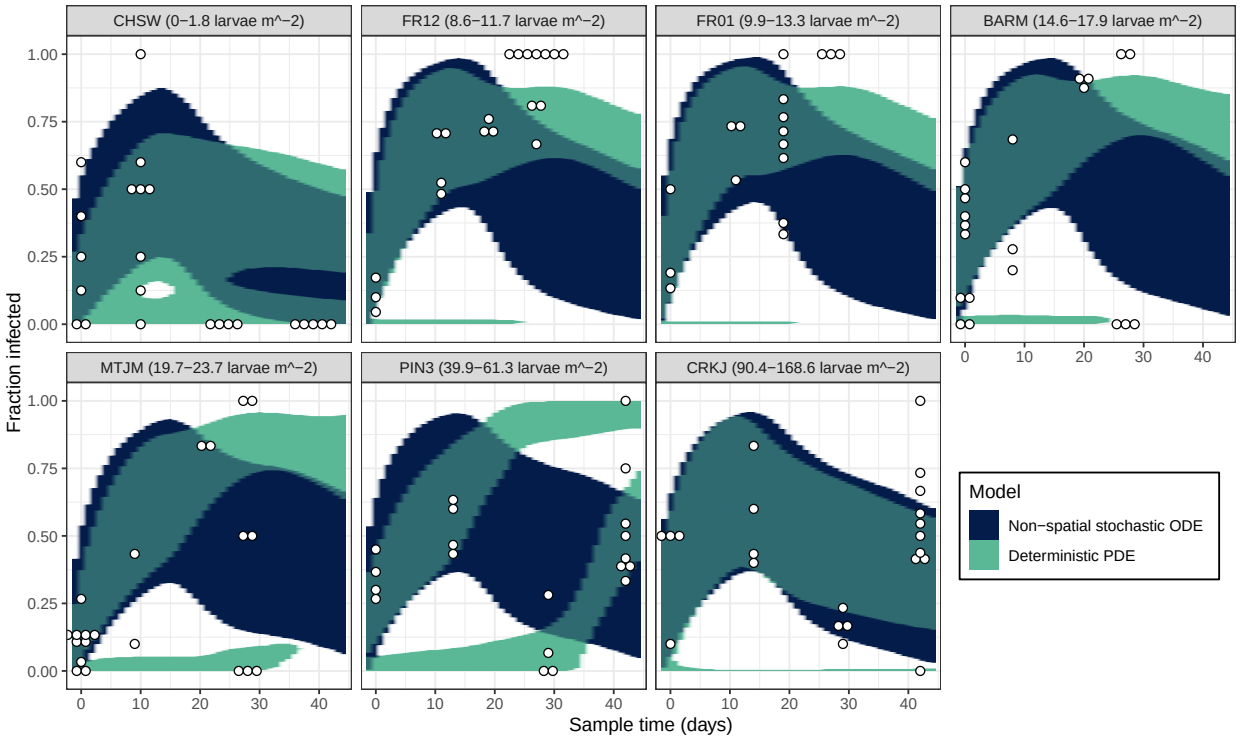

Figure 2.6: Posterior estimates of epizootic temporal dynamics for the deterministic PDE model (teal) and the non-spatial ODE model with environmental stochasticity (dark blue) plotted against the spatial distribution of infection rates observed in tree-level infection rates (white circles). The seven panels show posterior model projections and data from our seven study populations, showing the study site name and the insect branch density estimate (larvae per meter squared) in parentheses. Filled areas represent areas of high posterior probability from fitted model simulations, where more than 50% of simulations drawn from the posterior had high kernel density estimates $k(i,t) \geq 0.7$ for a given fraction infected i at a given time t.

coldspot sub-epizootics of some populations (figure B.6).

Moreover, the second-best model requires environmental stochasticity to explain our infection data, but key evidence from our model comparison suggests that environmental stochasticity is unlikely to be helpful for understanding baculovirus epizootics in natural populations. To begin, in the non-spatial model, the posterior estimate of the stochasticity parameter σ is roughly twice as high as the corresponding estimates in spatial models incorporating environmental stochasticity (table 2.1). This difference suggests that the non-spatial model uses environmental stochasticity to account for the effects of limited dispersal

and spatial structure, albeit ineffectively. Additional support for this reasoning comes from previous studies that have shown baculovirus epizootics are typically insensitive to weather, the presumed driver of environmental stochasticity (D'Amico and Elkinton [1995], Woods and Elkinton [1987]). Adding environmental stochasticity therefore serves mostly to spread out model trajectories until they include the data, rather than providing information that is otherwise missing from a model.

Further, the third-best model, which consists of the best model plus environmental stochasticity, had a difference of $\widehat{\Delta\text{ELPD}} = -2.53 \pm 1.62$. The fit of the third-best model is thus only slightly worse than the fit of the second-best model, but, in contrast, the data can distinguish the fit of the PDE model with environmental stochasticity to be worse than the fit of the best model. Crucially, the Bayesian stacking weight, the estimated percentage of the log predictive density that is better explained by a given model, was 0.00 for the third-best model. This stacking weight indicates that the stochastic model adds no new information to a composite model that already contains its deterministic analog, which is the best model. In addition, the remaining models consisted of model pairs that were identical except that one included environmental stochasticity while the other did not. In every paired case, the model that included environmental stochasticity had a worse model selection score than its analog that did not include environmental stochasticity. Model selection based on PSIS-LOO-CV therefore definitively rejects the hypothesis that allowing for environmental stochasticity improves the ability of our models to explain the data.

A more surprising result from our model-selection analysis is the poor performance of agent-based models, which allow for demographic stochasticity. Like environmental stochasticity, the inclusion of demographic stochasticity consistently lowered the selection score of models attempting to explain the infection rate variation in our data (table 2.1). Hybrid models with agents for hosts and differential equations for pathogens offered more predictive power than fully agent-based models, while both performed more poorly than the analogous

differential equations models (table 2.1). This result contradicts the widely held belief in spatial ecology theory that individual-based models are more realistic and therefore always more useful to understand data (Durrett and Levin [1994], DeAngelis and Grimm [2014]). It is worth noting, however, that unlike models incorporating environmental stochasticity, models incorporating demographic stochasticity were able to perform well for at least some of our study sites. Combining the non-zero Bayesian stacking weights shows that hybrid agent-based models accounted for $\sim 33\%$ of the log predictive density in a composite model, indicating that agent hosts, but not agent pathogens, can offer some predictive power (table 2.1).

Population-level cross validation showed that, in populations with higher larval host densities, agent-based models were indistinguishable from the best model (figure B.14). This result may at first appear counter-intuitive, given the greater importance of demographic stochasticity at smaller population sizes (He et al. [2010], Alonso et al. [2006], Britton et al. [2011]). However, it is important to realize that agent-based models are sensitive to exact population sizes, population sizes change rapidly once epizootics begin, and the variation induced by demographic stochasticity is strongest at the outset of the epizootic, when pathogen and exposed host populations are smaller (Britton et al. [2011], Lalley [2009], Andersson and Britton [1998]). From these points, it is clear that the variation induced by demographic stochasticity is sensitive to the uncertainty in initial host and pathogen densities, especially in smaller population sizes. Therefore, the uncertainty in our host density estimates has drastically stronger effects on model projections in populations with a posterior mean of one larva/m^2 than 100 larvae/m^2. This effect increased the variability of likelihood scores across realizations and thus lowered the performance of agent-based models relative to differential equations models, especially for early time points across populations (figure B.15). Agent-based models therefore have lower predictive power in smaller populations because their projections are more variable than those of PDE models.

2.3.3 Spatial transmission models provide a deeper understanding of insect tree damage

The mechanisms underlying baculovirus transmission dynamics are a research priority for forest pest management because Douglas-fir tussock moth outbreaks have severe consequences for forests in western North America (Mihaljevic et al. [2020], Mason [1977]). Although previous, non-spatial baculovirus transmission models have offered some insights into defoliation (Mihaljevic et al. [2020]), the tree damage caused by grazing insects, such models typically project high mortality when fit to baculovirus epizootic data. Observed defoliation is often also high, making the correlation between tussock moth mortality and observed defoliation unclear.

Rather than classical approaches that use insect densities or the ultimate fraction of hosts surviving to predict defoliation, we instead predicted tree damage using projected herbivory intensity from our mechanistic transmission models. We calculated the cumulative herbivory intensity $H(\tau)$ by summing projected larval densities from time $t = 0$ to $t = \tau$. Although the cumulative fraction of hosts infected was comparable between the spatial and non-spatial models, the coldspots in spatial models created refugia that allowed for high larval host densities outside of hotspots with active transmission. Even during severe epizootics with mortality exceeding $\sim 99\%$ of the host population, refugia greatly increased the average herbivory intensity at middle stages of the epizootic, after hosts in transmission hotspots began to die off but prior to dispersal-mediated establishment of baculovirus in coldspots. The average herbivory intensity over space was therefore up to 1.5 times greater than the average across non-spatial model simulations for the same insect and pathogen density initial conditions (figure 2.7A). Herbivory intensity $H(\tau)$ projected by the best spatial model was only lower than that of the non-spatial model when host densities were below the disease density threshold and pathogen densities were high. Although we did not directly observe such scenarios in our study populations due to the cryptic nature of extremely low Douglas-fir

tussock moth larval densities, this case is not likely to inform defoliation mitigation strategies because such populations do not cause detectable tree damage.

To determine if the posterior distribution of $H(\tau)$ could be useful for understanding observed defoliation patterns, we constructed logistic regression models that used projected herbivory to predict defoliation severity, the average percent of foliage lost in the tree canopy (figure 2.7B), and to predict defoliation extent, the percent of trees with defoliation (Appendix A). If the increased herbivory intensity due to susceptible hosts in coldspot refugia was mechanistically driving observed defoliation, we would expect that defoliation severity would be better predicted by the herbivory intensity from spatial model projections. Hosts surviving for longer would have more time to consume foliage, therefore increasing defoliation severity in coldpsot refugia, the average severity overall, and the risk of tree mortality. Defoliation extent predictions should be comparable across models, however, because the presence of defoliation across trees is related to initial insect densities prior to any mortality due to baculovirus exposure.

The herbivory projections of the best spatial model provided a reasonable fit to both defoliation extent ($R^2 = 0.29 \pm 0.06$) and severity ($R^2 = 0.38 \pm 0.04$). Crucially, the best spatial model was able to predict the higher maximum severity that we observed in high mortality study populations (figure 2.7B). Observed insect branch densities alone provided similar fits to defoliation extent ($R^2 = 0.29$, $\Delta\text{BIC} = (+14.2, -8.0)$), but provided a worse fit for severity ($R^2 = 0.23$, $\Delta\text{BIC} = (+1.2, +0.9)$), in line with the refugia hypothesis. The non-spatial model also had a worse fit to defoliation severity data ($R^2 = 0.33 \pm 0.08$, $\Delta\text{BIC} = (+1.1, 0.0)$), while having comparable predictions for extent ($R^2 = 0.31 \pm 0.04$, $\Delta\text{BIC} = (-4.1, +1.3)$, figure B.11). We thus concluded that, in addition to improving model fit for infection data, the hotspot and coldspot sub-epizootics that are a key feature of the best spatial model have important implications for herbivory intensity, and provide useful predictions of previously-unexplained, severe defoliation.

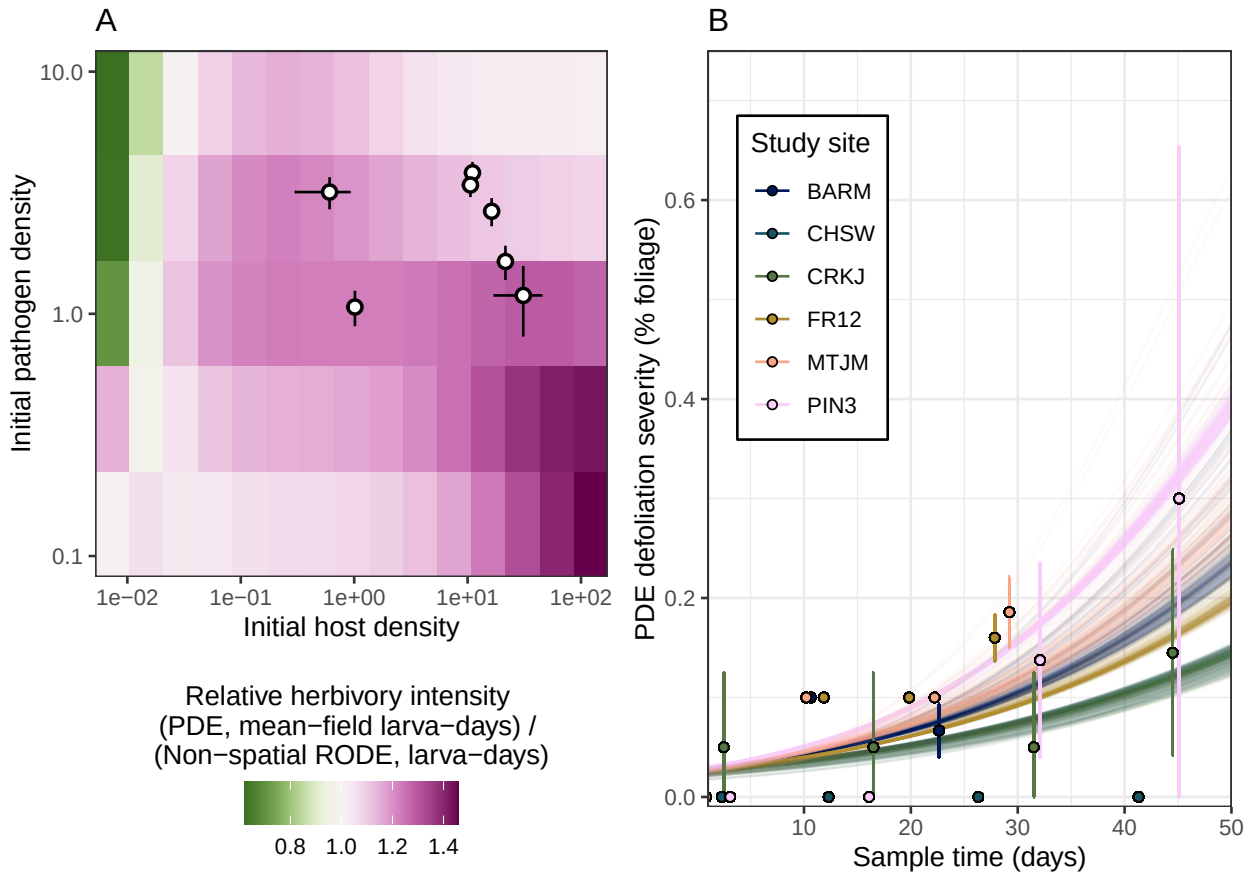

Figure 2.7: A) shows the relative expected herbivory intensity for initial host and pathogen densities, where herbivory intensity accumulates over time as larva-days per m^2. We use the mean-field herbivory intensity for the PDE model, which shows much higher intensity than expected under the non-spatial model for high host densities and low pathogen densities. Points and error bars show the credible intervals of initial host and pathogen densities estimated from the PDE. B) shows the observed defoliation severity (points) against the logistic regression predictions from PDE herbivory $H(\tau)$. Each study population is shown as a different color. Although the regression is a function of time t, defoliation severity predictions from each line is a draw from the posterior distribution over $H(\tau)$.

Because the divergent sub-epizootic trajectories of hotspots and coldspots are due to patchy initial pathogen distributions, Douglas-fir tussock moth defoliation severity mitigation can only be achieved through higher, and more uniform, pathogen densities (figure 2.7A). One pest management strategy able to provide such an effect is Tussock Moth Biocontrol (TMB), a natural isolate of the baculovirus produced by the US Forest Service and aerially sprayed to manage Douglas-fir tussock moth populations (Williams and Otvos

[2005]). Although criticized for having more rapid decay than naturally occurring infectious cadavers (Mihaljevic et al. [2020]), the benefits of reducing coldspot refugia may have outsize effects to reduce herbivoyr intensity, thereby reducing defoliation severity and increasing tree survivorship during *O. speudotsugata* outbreaks.

2.4 Discussion

Our work provides strong evidence for the occurrence of shifting transmission hotspots in baculovirus epizootics, affirming the importance of spatial theory for insect-baculovirus interactions. Diverging hotspot and coldspot sub-epizootics are not unique to baculovirus dynamics (Tian et al. [2018], Nassuato et al. [2013], Dowdy et al. [2012]), but the transmission models used to understand them are rarely spatial and are often not subjected to rigorous model comparison within single studies (Lessler et al. [2017], Ensoy et al. [2013], Lane-deGraaf et al. [2013]). Here we identify the causal mechanisms of hotspot occurrence in baculovirus epizootics for the first time, showing that they exacerbate the well-known phenomenon of delayed late-season peaks in larval baculovirus infection that result from exposure incubation periods (Woods and Elkinton [1987]). We indirectly observed the late-season establishment of baculovirus in patchy areas with previously unexposed host sub-populations, highlighting the importance of pathogen densities and host dispersal for determining the uneven rate of infection spread over space. Moreover, our model projections provide mechanistic explanations for spatial infection rate patterns and simultaneously offer explanations for the high levels of defoliation caused by tussock moth outbreaks that should otherwise collapse due to high average infection rates.

Our best spatial model explains the spatial variation of infection rates over time by invoking only variable initial conditions and limited host dispersal. However, even the worst spatial models outperformed the non-spatial model, underscoring the importance of comparing multiple spatial models to one another. The assessment of a spatial model in isolation

risks the inappropriate validation of additional assumptions tacked onto models that account for spatial structure. This concern is heightened by the marked qualitative differences between the spatial model projections over time (figure B.6) and their large variation in predictive performance (table 2.1). For example, through our model selection analysis we rigorously quantified by ELPD that stochasticity always lowered the predictive performance of the spatial models, whether such stochasticity was environmental or demographic (table 2.1).

The lack of improvement when we included effects of environmental stochasticity is perhaps unsurprising, but it suggests that models incorporating environmental stochasticity may obscure the important effects of spatial heterogeneity on pathogen dynamics, especially when fitted to non-spatial data. Whether in baculoviruses (Mihaljevic et al. [2020], Dwyer et al. [2022]) or other pathogens (Alonso et al. [2006], Andersson and Britton [1998]), stochastic modeling is ubiquitous in contemporary disease modeling as it is considered essential for robust inferences (He et al. [2010], Funk and King [2020]). However, our work shows that for baculovirus epizootics, and perhaps for other environmentally transmitted diseases, the strength of stochasticity to account for variation in the mechanisms included within a model could also validate incorrect assumptions about the role of limited dispersal in the absence of rigorous spatial model comparison.

Given the better performance of PDE models relative to agent-based models, our study emphasizes the utility of deterministic moment closure approximations, which can incorporate variability introduced by individual fates without being sensitive to exact densities over time (figure B.14). Further, the selection of the reaction-diffusion model over agent-based simulations drives the rate at which coldspot sub-epizootics become late-season transmission hotspots. In the best model, point releases of infectious material generate travelling waves that propagate even at the low diffusion rate we estimated as the true rate of larval host movement. In the agent-based models, however, dispersal rates were greatly inflated because

travelling waves at slower rates stopped due to drift (figure E.2). Premature termination of travelling waves due to demographic stochasticity made the agent-based models incorporating limited host dispersal closely resemble the agent-based models assuming no dispersal in a wide range of scenarios.

The advancing waves of baculovirus establishment in coldspot sub-spizootics we found to be key to understanding baculovirus transmission are in fact related to an early criticism of diffusion models. Because reaction-diffusion equations depend on infinitesimal exposed host densities to establish pathogen populations, such models were thought to be irrelevant for describing natural systems subject to demographic stochasticity (Anderson et al. [1981], Murray et al. [1986], Mollison [1991]). Although originating in rabies, where this critique may be more reasonably applied, this debate continues to receive generalized theoretical attention, both analytically (Fowler [2021], Lobry and Sari [2015]) and through the advocacy for using discrete agents to represent demographic processes (Durrett and Levin [1994], DeAngelis and Grimm [2014], Alonso et al. [2006]). The success of our hybrid models, where pathogens are infinitely divisible densities, as compared to the fully agent-based models, where infectious cadavers are discrete individuals, demonstrates that, for at least baculovirus transmission, occlusion body virions are the discrete individual units that propagate disease spread.

We therefore suggest that the utility of demographic stochasticity is not a universal truth, and that infinitesimal infectious densities and dispersal-mediated sub-epizootic dynamics are highly useful for understanding infection data through the establishment and propagation of transmission hotspots. With the growing recognition of environmental transmission as a major mode of directly transmissible diseases, our inferences may be more generally useful in systems apart from insect-baculovirus interactions and could warrant further applications (Breban et al. [2009], Brown et al. [2013b]). While pathogen densities tend to receive less attention than host densities in the estimation of epidemic size (Lloyd-Smith et al. [2005b], Keeling and Rohani [2008]), we demonstrate that low, infinitesimally-divisible pathogen

densities alter host survivorship over time, with profound ecological impacts that occur in nature. Moment closures, along with reaction diffusion equations, have a rich history in the field of disease ecology, but the two are rarely combined (Dwyer et al. [2000], Murray et al. [1986], Keeling and Rohani [2008]). Our novel reaction-diffusion approximation of heterogeneity in infection risk therefore provides a crucial step towards understanding the mechanisms driving transmission rate variation over space.

Rank	Model description	Agent types	Movement	$\widehat{\Delta\text{ELPD}} \pm \text{SE}$	Environmental stochasticity σ, posterior mean (95% credible interval)	Stacking weight
1	Deterministic PDE	None	Host diffusion	0.00 ± 0.00	–	0.45
2	Independent ODE systems with environmental stochasticity	None	None	-2.31 ± 3.26	0.15 (0.11, 0.19)	0.22
3	PDE with environmental stochasticity	None	Host diffusion	-2.53 ± 1.62	0.17 (0.13, 0.214)	0.00
4	Hybrid agent-based host with pathogen PDE	Hosts	Cadaver diffusion	-12.38 ± 6.78	–	0.21
5	Fully agent-based without movement	Hosts and cadavers	None	-13.20 ± 6.81	–	0.00
6	Hybrid agent-based host with independent pathogen ODEs	Hosts	None	-13.37 ± 6.94	–	0.12
7	Fully agent-based with host dispersal	Hosts and cadavers	Host nearest neighbor	-13.85 ± 6.71	–	0.00
8	Hybrid agent-based host with waning cadaver diffusion PDE	Hosts	Cadaver diffusion	-14.00 ± 6.98	–	0.00
9	Hybrid agent-based host with independent pathogen ODEs and host dispersal	Hosts	Host nearest neighbor	-14.61 ± 6.98	–	0.00
10	Fully agent-based with environmental stochasticity	Hosts and cadavers	None	-14.78 ± 6.86	0.14 (0.10, 0.18)	0.00
11	Fully agent-based with host dispersal and environmental stochasticity	Hosts and cadavers	Host nearest neighbor	-14.80 ± 6.83	0.12 (0.08, 0.16)	0.00
12	Non-spatial ODE with environmental stochasticity	None	Non-spatial	-24.21 ± 8.21	0.32 (0.27, 0.39)	0.00

Table 2.1: LOO-CV table from formal model selection. Estimates of $\widehat{\Delta\text{ELPD}}$ show absolute model ranking where a standard error overlapping zero indicates no difference from the best model. Model averaging was conducted to understand contribution of each model to the maximal LOO-CV predictive density using Bayesian stacking of predictive distributions. Stacking weight indicates the ideal proportional mixture of all models, summing to one. For models incorporating environmental stochasticity, posterior estimates of the standard deviation σ of the log-normal distribution of parameter fluctuations ϵ_τ are shown. Waning cadaver diffusion of Model 7 is to emulate the dispersal of first instar exposed individuals prior to mortality.

CHAPTER 3

HERITABLE INFECTION RISK GENERATES ACCELERATING WAVES AND RE-PRODUCES INSECT OUTBREAK DATA

3.1 Introduction

The theory of biological invasions provides a useful conceptual framework for describing the spread of populations over time and space (Williamson [1996], Shigesada and Kawasaki [1997], Okubo and Levin [2001]), notably by showing that limited dispersal can lead to travelling waves of population expansion (Murray et al. [1986], Dwyer [1992], Kot et al. [1996]). Although most often invoked in studies of invasive species (Burton et al. [2010], Rollins et al. [2015]), travelling waves can also describe non-invasive populations undergoing range expansions (Hill et al. [1999]), or variation in population cycles within an organism's native range (Bjørnstad et al. [2002]). For mathematical convenience, early analyses of travelling waves focused on constant wave speeds (Skellam [1951], Shigesada and Kawasaki [1997]), but later work showed that waves can also accelerate (Kot et al. [1996]). This is important because travelling waves in nature often accelerate (Williams et al. [2019], Miller et al. [2020]).

Early studies argued that accelerating waves are likely due to a small but non-trivial number of individuals travelling exceptionally long distances (Kot et al. [1996], in what follows we refer to this phenomenon as "exceptional dispersal"). Recent work, however, has shown that acceleration can also be driven by the evolution of traits relevant to reproduction or movement at the wave front (Edmonds et al. [2004], Perkins et al. [2013], Fetters and McGlothlin [2017], Deforet et al. [2019]), an effect that holds even for multi-species models (Burton et al. [2010], Perkins [2012], Bennett and Sherratt [2019]). Efforts to explain data on accelerating waves have generally only ever invoked exceptional dispersal or evolutionary change in isolation and thus have not considered the relative importance of the two mecha-

nisms. Partly as a result, the effects of evolution at the wave front for population dynamics behind the wave front are poorly understood (Erm and Phillips [2020]).

Here, we carry out a test of the importance of evolution and exceptional dispersal for both population dynamics and trait variation in a seasonally driven host-pathogen interaction undergoing a range expansion. We take advantage of a natural travelling wave in Douglas-fir tussock moth, *Orgyia pseudotsugata*, to test the relative usefulness of exceptional long-distance dispersal and evolutionary change for explaining data on accelerating waves in nature. Tussock moth populations regularly fluctuate from high to low densities in predator-prey type cycles that are driven by a host-specific, fatal baculovirus (Brookes et al. [1978], Mason [1996]). For Douglas-fir tussock moth, these cycles occur roughly every nine years and, during high-density outbreaks, cause defoliation that damages trees. In western Montana, however, outbreaks did not occur between 1976 and 2000, even though they had occurred in previous decades (Shepherd et al. [1988]). Then, from 2000 to 2007, outbreak-level tussock moth populations occurred nearly every year. Although the question of why the tussock moth disappeared and re-established in western Montana is biologically interesting, we lack sufficient information to answer it here. However, as we will demonstrate, these outbreaks show wave-like patterns and we can provide insights into the mechanisms that determine the speed of advance and spatial patterning of tussock moth spread.

Host-pathogen or predator-prey population dynamics in the wake of invasion could be a stable point equilibrium, stable cycles, or chaos, but which patterns occur in nature is rarely investigated (Bjørnstad et al. [2002], Sherratt and Smith [2008], Bennett and Sherratt [2019], Miller et al. [2020]). Instead, in studies of travelling waves in host-pathogen interactions, often only the wave speed is derived (Murray et al. [1986], Dwyer [1992], Mundt et al. [2009], Phillips et al. [2010], Leung and Kot [2015]). Although an important metric, the average wave speed generally provides little to no information about what the population dynamics of ecological systems will look like after range expansion has occurred (Sherratt et al. [1995],

Sherratt and Smith [2008]). For example, even in the absence of evolutionary processes, only limited areas of parameter space generate stable travelling waves (Grenfell et al. [2001], Bjørnstad et al. [2002]). To better understand accelerating waves, we therefore compared model predictions to data on both dynamics at the wave front and dynamics behind the wave front.

Previous studies that have invoked evolutionary change to understand accelerating waves have often focused on how the evolution of average trait values causes acceleration, particularly on the evolution of average dispersal distance (Perkins et al. [2013], Brown et al. [2013a], Bennett and Sherratt [2019], Erm and Phillips [2020]), or average fecundity at the wave front (Mason et al. [2008], Weiss-Lehman et al. [2017], Fetters and McGlothlin [2017]). This focus on average trait values, however, has led to a limited understanding of heritable variation. Meanwhile, there is strong evidence that Douglas-fir tussock moth larvae vary in their infection risk (Dwyer et al. [2000], Mihaljevic et al. [2020]) and that heritable infection risk can alter tussock moth outbreak cycles (Páez et al. [2017], Dwyer et al. [2022]). However, the mechanisms that maintain this variation are largely unknown, even in theory (Erm and Phillips [2020]). In this study, we attempt to understand how heterogeneity in the Douglas-fir tussock moth's infection risk is maintained by explicitly modeling variation in infection risk both at and behind the wave front. We do this by constructing spatial eco-evolutionary models that explain spatial patterns in defoliation data by invoking either evolving fecundity and infection risk at the wave front or exceptional dispersal. Our work shows that an eco-evolutionary model is a better explanation for accelerating waves than an exceptional dispersal model. Our work thus provides, to the best of our knowledge, the first example demonstrating that evolution has a larger effect on the spread of a species interaction than does long-distance dispersal.

3.2 Methods

Douglas-fir tussock moth populations are often so low as to be undetectable, while densities during periodic outbreaks are high enough to cause severe tree damage (Mason [1987, 1996]). To identify high-density Douglas-fir tussock moth populations in western Montana, we used tree defoliation data from annual aerial detection surveys provided by the US Forest Service. Although the data track the two-dimensional spread of tussock moth defoliation, visual inspection of the data suggested that the spread was approximately linear. We therefore simplified our analysis of the data by transforming the coordinates of all defoliation from 2000 to 2019 using principal component analysis (PCA). Because the first order principal component (PC1) explained $\sim$ 87% of the coordinate variance, we built a linear model that describes distance from the 2000 origin in PC1 units, resulting in a transformed, one-dimensional data set of the spread of the population over space and time. We then used the average position of defoliation, the putative high-density tussock moth populations, along PC1 as the wave front position.

Our model of spatial spread without evolution begins with a non-spatial model that can provide reasonable projections of forest insect population dynamics (Dwyer et al. [2000]). Like many outbreaking insects, Douglas-fir tussock moths have discrete, non-overlapping generations (Hunter [1995]). The model then assumes that the host population N_{n+1} and the pathogen population Z_{n+1} in generation $n+1$ are determined partly by the fraction of hosts $i_n(N_n, Z_n)$ that become infected during the epizootic of the previous generation n. A fraction infected i_n become infectious cadavers in the next generation at overwintering rate ϕ while the remaining fraction $(1 - i_n)$ reproduces at rate r (Dwyer et al. [2000]). To introduce space into this model, we used integrodifference equations, which assume that space is continuous and generations are discrete (Kot et al. [1996]).

$$N_{n+1}(x) = \int \overbrace{r N_n(y)\left[1 - i_n(y)\right]}^{\text{Reproduction}} \overbrace{k(x,y)}^{\text{Dispersal}}\, dy \tag{3.1}$$

$$Z_{n+1}(x) = \int \underbrace{\phi N_n(y) i_n(y)}_{\text{Overwintering}} \underbrace{k(x,y)}_{\text{Dispersal}}\, dy + \underbrace{\gamma Z_n(x)}_{\text{Pathogen survival}} \tag{3.2}$$

$$i_n(x) = 1 - \left(1 + \frac{\bar{\nu} V}{\mu}\left(N_n i_n + Z_n\right)\right)^{-\frac{1}{V}}, \tag{3.3}$$

Here, the dispersal function $k(x, y)$, usually referred to as a dispersal "kernel", is the probability that individuals dispersing from location y arrive at location x. Because the transformed data are effectively one-dimensional, we allow for only one-dimensional spread in the model. The dispersal kernel $k(x, y)$ can either be a "thin-tailed" kernel, meaning that its tails decay exponentially, or a "heavy-tailed" kernel, meaning that its tails allow for exceptional long-distance dispersal. We consider a special case of heavy-tailed kernels called "fat-tailed" kernels that decay according to a power law and that are known to generate accelerating waves (Kot et al. [1996], Mundt et al. [2009], Liu and Kot [2019]).

Adult female tussock moths are flightless, so the main form of long-distance dispersal occurs when larvae "balloon", during which they produce silken strands that allow the larvae to disperse on the wind (Mitchell [1979]). Because the baculovirus disperses in the form of infected first instar larvae, and because there is no evidence that viral infection affects ballooning (Brookes et al. [1978]), we assumed that overwintering baculovirus disperses according to the same dispersal kernel as uninfected hosts. We further assume that baculovirus that survives over the long-term at rate γ does not disperse.

Virus transmission is the result of direct contact between uninfected larvae and infectious cadavers (Cory and Myers [2003]). Thus the fraction of hosts $i_n(x)$ infected is described by a standard "$SEIR$" model from theoretical epidemiology modified to allow for host variation of infection risk, which is a basic feature of insect-baculovirus interactions (Appendix C,

Dwyer et al. [2000], Keeling and Rohani [2008], Myers and Cory [2015]). Therefore, the fraction of hosts $i_n(x)$ infected in generation n depends on the average infection risk at the start of the epizootic, $\bar{\nu}$, the squared coefficient of variation of infection risk, V (Appendix C, Dwyer et al. [2000, 2022]), and the decay rate of the pathogen, μ.

In our eco-evolutionary model, we allow for a fitness trade-off such that high fecundity is associated with high infection risk through a cost parameter ω (Appendix C, Elderd et al. [2008], Páez et al. [2017], Dwyer et al. [2022]). The eco-evolutionary model allows for evolutionary change in the average infection risk $\bar{\nu}_n(x)$ and in the host variation $V_n(x)$, the squared coefficient of variation of the distribution of infection risk. Because infection risk is likely due to a mixture of genetic and environmental factors, and to avoid the unrealistic evolution of complete baculovirus resistance, we assume that infection risk is only partly heritable. The heritability b is thus the fraction of the variance in the infection risk that is due to additive genetic variation (Páez et al. [2017]). The full eco-evolutionary integrodifference model is

$$N_{n+1}(x) = \int rk(x,y)N_n(y)\left[1-i_n(y)\right]\overbrace{\left(1+\omega\bar{\nu}_n(y)\left[1-i_n(y)\right]^{\frac{V_n(y)}{b}}\right)}^{\text{Trade-off effect on fecundity}}dy \tag{3.4}$$

$$Z_{n+1}(x) = \int k(x,y)\phi N_n(y)i_n(y)dy + \gamma Z_n(x) \tag{3.5}$$

$$\bar{\nu}_{n+1}(x) = \frac{\int k(x,y)N_n(y)(1-i_n(y))\bar{\nu}_{n+\frac{1}{2}}(y)\overbrace{\left[1+\omega(1+V_n(y))\bar{\nu}_{n+\frac{1}{2}}(y)\right]}^{\text{Trade-off effect on average risk}}dy}{\int k(x,y)N_n(y)(1-i_n(y))\left[1+\omega\bar{\nu}_{n+\frac{1}{2}}(y)\right]dy} \tag{3.6}$$

$$V_{n+1}(x) = \frac{\int k(x,y)N_n(y)(1-i_n(y))\bar{\nu}^2_{n+\frac{1}{2}}(y)\overbrace{\left[1+V_n(y)\right]\left[1+\omega(1+2V_n(y))\bar{\nu}_{n+\frac{1}{2}}(y)\right]}^{\text{Trade-off effect on variation in risk}}dy}{\bar{\nu}^2_{n+1}(x)\times\int k(x,y)N_n(y)(1-i_n(y))\left[1+\omega\bar{\nu}_{n+\frac{1}{2}}(y)\right]dy} - 1 \tag{3.7}$$

$$i_n(x) = 1-\left(1+\frac{\bar{\nu}_n(x)V_n(x)}{b\mu}\left(N_n(x)i_n(x)+Z_n(x)\right)\right)^{-\frac{b}{V_n(x)}} \tag{3.8}$$

$$\bar{\nu}_{n+\frac{1}{2}}(x) = \underbrace{\bar{\nu}_n(x)\left[1-i_n(x)\right]^{V_n(x)}}_{\text{Infection risk before reproduction}}, \tag{3.9}$$

Here, we simplify the notation by explicitly including an expression for the "half-generation" average infection risk $\bar{\nu}_{n+\frac{1}{2}}(x)$, which is determined after the epizootic in generation n but before reproduction or dispersal.

To understand the relative importance of exceptional long-distance dispersal and evolutionary change in driving accelerating waves, we fit four different versions of our models to the tussock moth spread data. The first model included a thin-tailed kernel and evolving infection risk, the second included a fat-tailed kernel and evolving infection risk, the third included a fat-tailed kernel but did not include evolving infection risk, while the fourth model included neither a fat-tailed kernel nor evolving infection risk.

Initially, we used the wave front data to fit only the parameters that affect the wave speed, which are the intrinsic reproduction rate r, the cost ω, and the dispersal parameter,

the meaning of which differed between thin-tailed and fat-tailed dispersal kernels. To explain why, we note that to ensure that models with different dispersal kernels could be comparable, we used a thin-tailed Laplace kernel and a fat-tailed Laplace kernel, which are approximately equivalent for some parameter values and very different for others (Liu and Kot [2019]). The dispersal parameter therefore consisted of either the power law decay order α for a fat-tailed Laplace kernel or the expected absolute distance travelled $\mathbb{E}[|\Delta x|]$ for a thin-tailed Laplace kernel.

Simulating the full integrodifference model equations is computationally intensive, so we instead fit only analytical expressions for the wave speed to the data (Appendix D.1, Kot et al. [1996], Neubert et al. [2000], Liu and Kot [2019]). Because pathogen spread rates are limited by their hosts, such that pathogen advance often lags behind the host wave front, we used analytical wave speeds that approximate the host invasion in the absence of the baculovirus (Sherratt et al. [1995], Bjørnstad et al. [2002], Phillips et al. [2010]). For each parameter set, we calculated the sum of squared errors (SSE) from the one-dimensional defoliation wave front data and then used `optim` in `R` to estimate the nuisance parameters, the initial variation $V_0(0)$ and initial average infection risk $\bar{\nu}_0(0)$, that minimized the SSE for each parameter set. The low number of parameters that determine wave speed meant that a simple grid search routine over 3,000 parameter sets was sufficient to find the maximum likelihood estimates of the parameters (Appendix D.2, McKinley et al. [2009]). Because the number of parameters and number of observations were the same across models, we were then able to select the best model using the SSE without correcting for differences in the number of parameters between models (Yates et al. [2023]).

To compare our models to data from behind the wave front, we used the best-fit parameters from our wave front fitting routine and conducted a second grid search routine across the remaining parameters, which do not affect the wave speed but do affect the population dynamics behind the wave front: pathogen overwintering ϕ, pathogen survival γ, pathogen

decay μ, and heritability b (Dwyer et al. [2000, 2022]). Because generating model predictions of dynamics behind the wave front necessarily required full integrodifference models, in this case we generated spatial simulations for each of the 100 parameter sets of our grid search routine. Because we did not have enough information to construct a separate model of defoliation, we assumed that areas with high host densities in the integrodifference models corresponded to areas of defoliation in the data (as shown in Chapter 2, Shepherd et al. [1988], Mason [1996]). We thus assumed that defoliation occurred with a probability equal to the percentile of the host density in the simulation. Because we had no information about the starting year of the invasion, we also varied the year of initial re-introduction, from 1995 to 2000. As in our comparisons of the model to the wave front data, the number of parameters was the same across models and so we were able to choose the best model using only the unadjusted likelihood.

3.3 Results

In our non-evolutionary model, point releases of hosts and pathogens in empty landscapes led to travelling waves with a constant speed of advance, but in our eco-evolutionary model the travelling waves accelerated (figure 3.1). Because host populations near the wave front in the evolutionary model were reproducing in the absence of the pathogen, those populations had higher fecundity and increased average infection risk $\bar{\nu}_n(\hat{x}_n)$. Host-pathogen interactions with heritable host infection risk can thus lead to accelerating waves because of increased fecundity at the wave front.

As the average infection risk increased near the wave front, the variation in the infection risk $V_n(\hat{x}_n)$ decreased over time (figure 3.5). Although a similar decline occurred in the corresponding non-spatial model, the decline occurred much more rapidly near the wave front in the spatial model (Appendix C). This rapid decline occurred because host populations near the wave front experienced very low selection pressure for increased resistance and thus

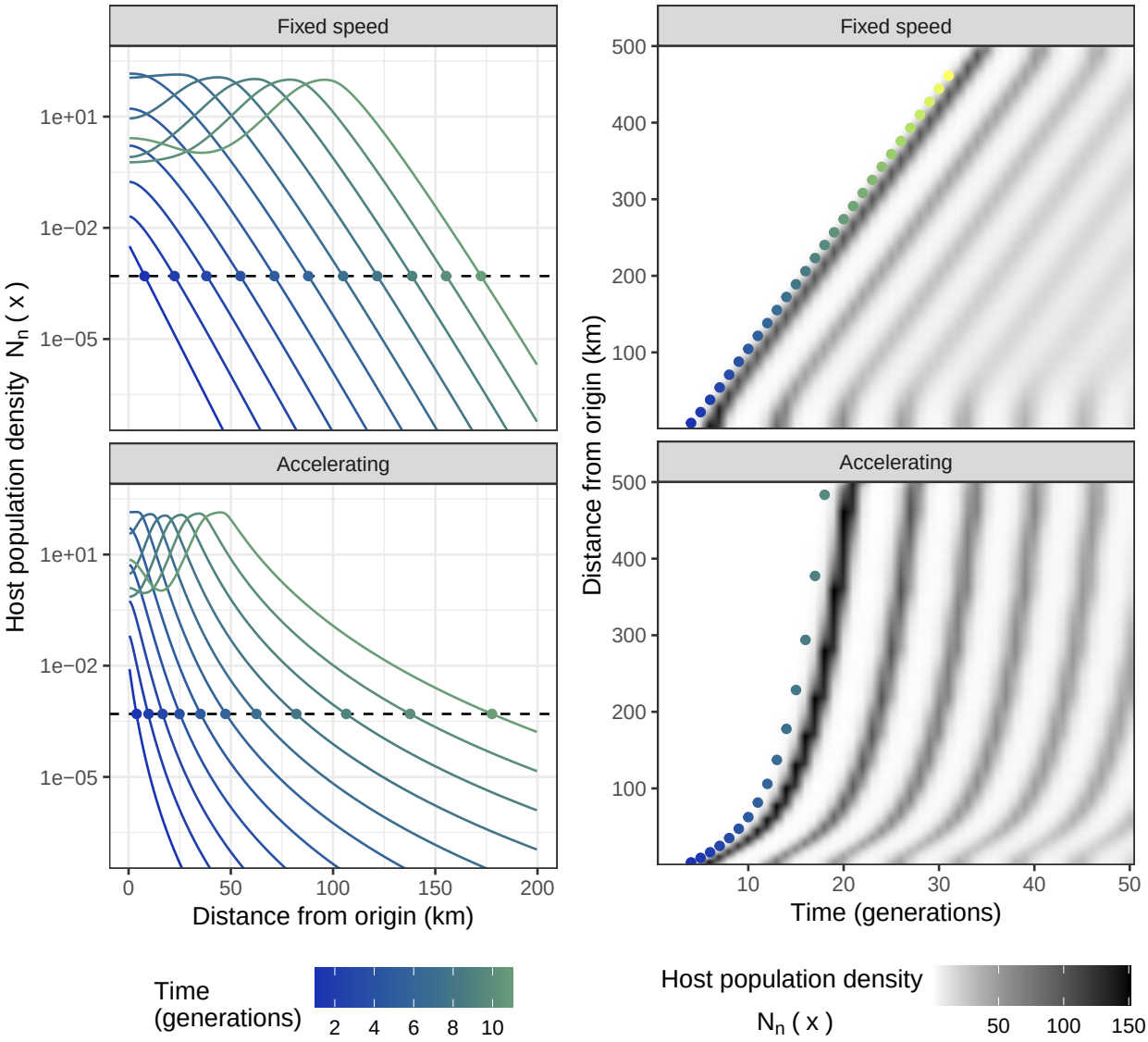

Figure 3.1: Summary of model projections. Upper panels show the non-evolutionary model while the lower panels show the evolutionary model for the case in which the dispersal kernel is a fat-tailed Laplace distribution. Left panels show host densities over space for generations 1 through 11. Distances between wave front locations $\hat{x}_n$ that reach the threshold density $\bar{N} = 1 \times 10^{-3}$ in successive generations are shown as points. Right panels show the host densities from the same simulations as a birds-eye view over generations $n = 1$ through 50. In the right hand panels, the colored points show how far the wave front has moved, with colors corresponding to the same generations as the left hand panels.

Rank	Evolution	Dispersal kernel	Cost ω	Intrinsic growth r	Dispersal value	SSE
1	Yes	Thin-tailed	7.44	1.01	$\mathbb{E}[\lvert\Delta x\rvert] = 1.73$	28.9
2	Yes	Fat-tailed	809.7	1.02	$\alpha = 1744.9$	30.5
3	No	Fat-tailed	-	48.7	α =18.60	181.0
4	No	Thin-tailed	-	9.51	$\mathbb{E}[\lvert\Delta x\rvert] = 2.79$	732.3

Table 3.1: Four models incorporating either eco-evolutionary dynamics (models 1 and 2), fat-tailed dispersal (models 2 and 3) or both (model 2) and associated sum of squared errors.

fecundity increased, reducing variation (figure 3.5).

The only model without an accelerating wave of advance, the model without evolution and with a thin-tailed kernel, provided by far the worst fit to the data (SSE = 732.3), with an average residual difference between the best-fit wave front and the data of 11.0 km. From this, we conclude that Douglas-fir tussock moth spread accelerated during re-establishment (figure 3.2). Although the model with a fat-tailed dispersal kernel and no evolution also generated accelerating waves, that model badly overestimated the early 2000-2003 wave front position and therefore also provided a poor fit to the data (SSE = 181.0, figure 3.2). The evolutionary models provided a better fit to defoliation data than either of the models without evolution, regardless of whether the dispersal kernel was fat- or thin-tailed (figure 3.2, table 3.1). Our evolutionary models were able to capture both the slow expansion during the early stages of the invasion and the more rapid expansion later in the invasion, and therefore had much lower error overall (SSE = 28.9, 30.5, table 3.1). We therefore conclude that evolution is necessary to explain tussock moth spread.

Notably, the two evolutionary models produced nearly identical wave fronts (figure 3.2). To explain this similarity, we note that the fat-tailed Laplace converges to a thin-tailed Laplace for high values of power law decay $\alpha \geq 100$ (figure 3.3A). This is important because the evolutionary model with fat-tailed dispersal explained the defoliation data better at higher levels of α, such that this best-fit dispersal kernel was effectively thin-tailed. In contrast, the non-evolutionary model with fat-tailed dispersal model explained the data better for lower values of α, and therefore required fat-tailed dispersal to explain the data

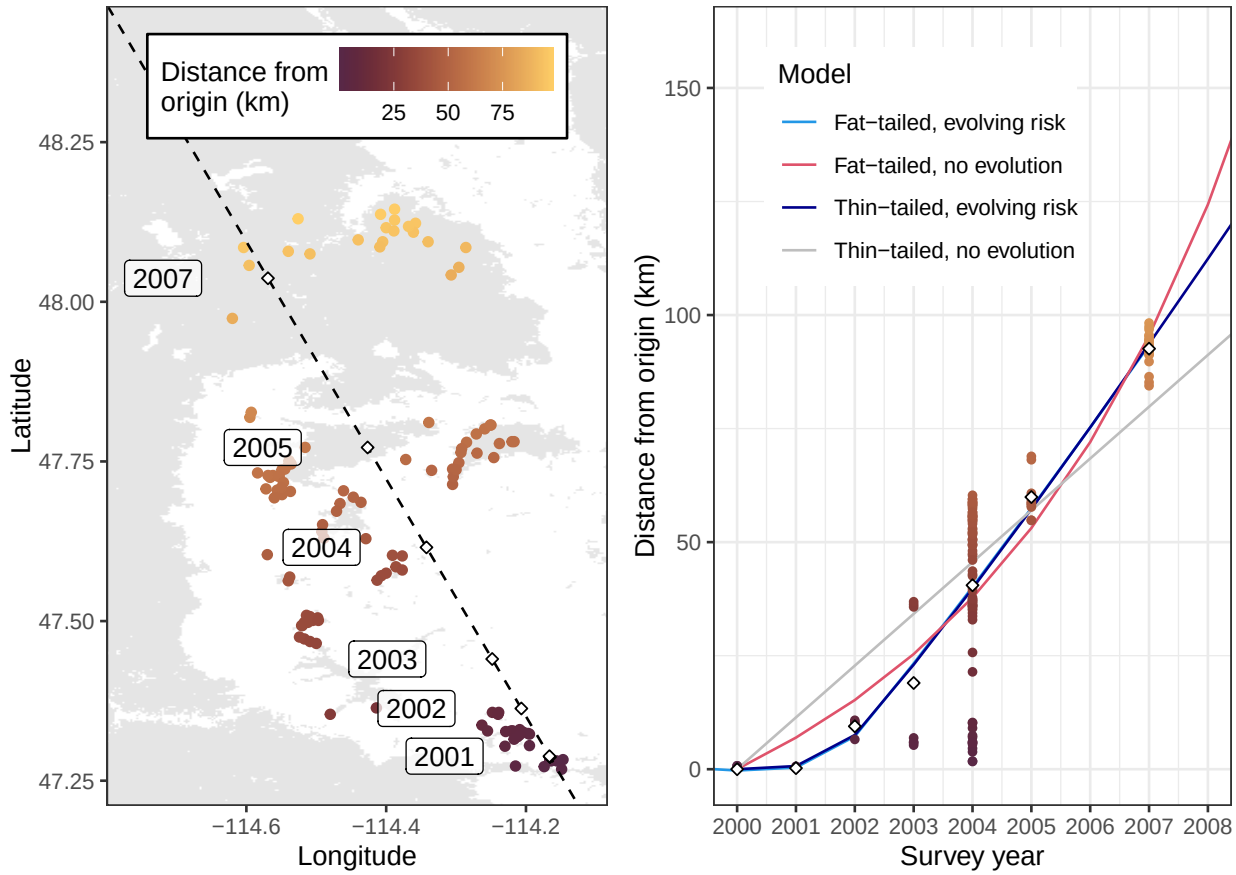

Figure 3.2: The defoliation data and fit of our four competing models to the data. Left panel shows a map of defoliation from 2000 to 2007. Habitable forest is shown in grey while uninhabitable non-forest is shown in white. Dashed black line shows the first order principal component which explains 87% of the variation over latitude and longitude. Labels show the average wave front as white diamonds along PC1 and in labels alongside. Right panel shows the best-fit invasion fronts for each of the four models as described in the methods. We used the average location of defoliation (white points) as an estimate of the furthest defoliation distance to reduce the bias introduced by environmental variation in our 1D projection. All other points show the defoliation from the left panel projected from 2D to 1D.

(figure 3.3B).

Indeed, the estimated value of $\alpha = 1745$ for the evolution model with a (potentially) thin-tailed kernel was sufficiently high that there was no difference between the tails of its dispersal kernel and those of the evolutionary model with an explicitly thin-tailed kernel (figure 3.3A). The SSE difference between the two evolutionary models (ΔSSE = 1.6) was therefore due to the average dispersal distance, which was 1.73 km in the thin-tailed eco-evolutionary model and 1 km in the fat-tailed eco-evolutionary model. The much lower SSE at higher values of α demonstrates that the accelerating re-establishment that we observe in the wave front data is not caused by fat-tailed dispersal kernels. Rather, the acceleration is solely caused by the evolving infection risk and increased fecundity at the wave front. We therefore conclude that accelerating waves in Douglas-fir tussock moth are better explained by evolutionary change than by fat-tailed dispersal.

In addition to explaining the wave front spread, our eco-evolutionary model was able to provide a good fit to defoliation data behind the wave front (figure 3.4). The eco-evolutionary model was able to explain the defoliation data behind the wave front regardless of fat-tailed ($\Delta\text{AIC} = 0$) or thin-tailed ($\Delta\text{AIC} = -1.35$) dispersal (figure D.3). Model ability to explain wave fronts was independent of overwintering ϕ and survival γ, but tended to be higher for low pathogen decay μ. We found that the initial year of re-introduction between 1995 and 1997 was important for explaining the defoliation data (figure D.5). There was considerable support for intermediate values of heritability $b = 0.02$ and $b = 0.002$ based on likelihood score comparison (figure D.4). Although the non-evolutionary model with a thin-tailed dispersal kernel was the worst model for describing the wave front, we observed that it was able to better describe defoliation data behind the wave front ($\Delta\text{AIC} = -10.8$) than the model incorporating fat-tailed dispersal and lacking evolution, which provided the worst explanation ($\Delta\text{AIC} = -23.4$). Our comparison of model simulations to defoliation data after the initial invasion front therefore further indicates that exceptional dispersal is unlikely to

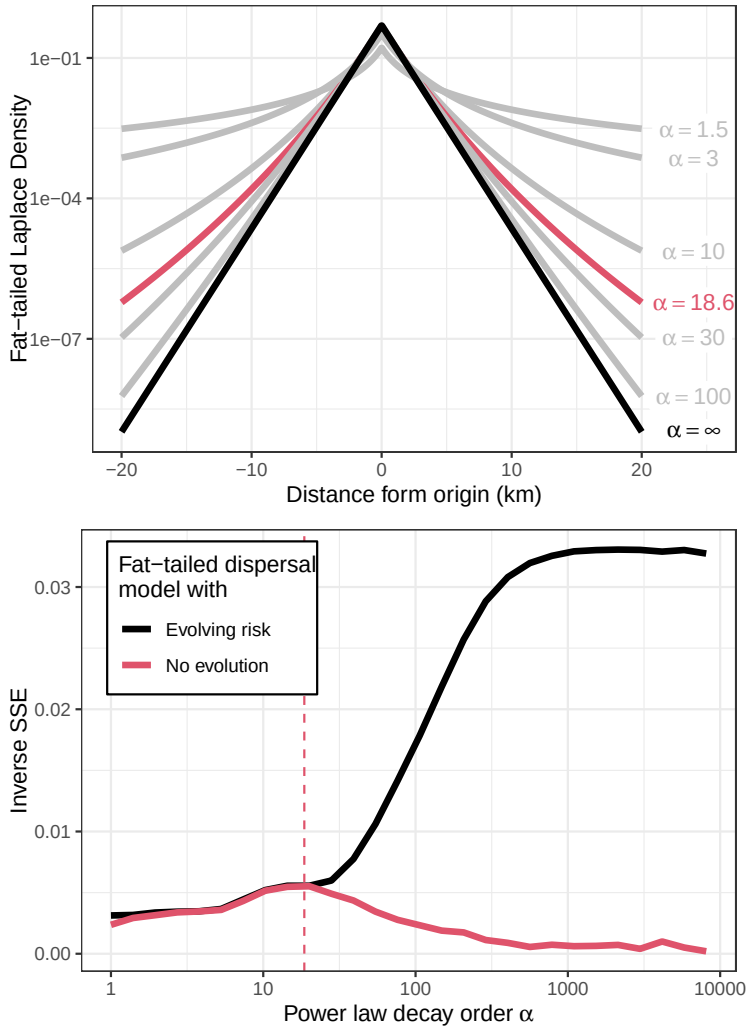

Figure 3.3: Effects of power-law decay α on fat-tailed dispersal kernels. The top panel shows the fat-tailed Laplace kernel with power law decay α, which is thin-tailed in the limit $\alpha = \infty$. The red line shows the best-fit value of α from the non-evolutionary model while the black line shows the limit of α, which is nearly identical from the best-fit value of α in the evolutionary model. At around $\alpha = 100$, the two distributions are essentially indistinguishable. The bottom panel shows the marginal inverse SSE, a measure of goodness-of-fit, with respect to α for the fat-tailed Laplace models when fit to the data. The model without evolution has a peak at the maximum likelihood estimate $\alpha = 18.6$ (table 3.1), and is thus moderately fat-tailed. For the model with evolution, however, the inverse SSE increases with α, showing that the model with evolution fits the data better with a thin-tailed dispersal kernel.

provide informative predictions for long-term population dynamics.

Crucially, the best-fit simulations of our eco-evolutionary models showed realistic cycles in both the host and pathogen populations (figure 3.6). Moderate heritability $b \geq 0.02$ was important to produce realistic sustained cycles, with periods that averaged 7 to 11 years and with amplitudes of several orders of magnitude, that mirror tussock moth populations in nature (Shepherd et al. [1988], Dwyer et al. [2022]). While lower values of heritability $b \leq 0.002$ were able to explain some of the defoliation data, but led to dampened oscillations that could not account for the recurrence of outbreaks in 2012. We therefore conclude that our eco-evolutionary models with heritability $b = 0.02$ are able to explain recurrent outbreaks caused by natural cycles through at least moderate heritability of infection risk.

Although variation in infection risk $V_n(\hat{x}_n)$ near the wave front decreased during spread, behind the wave front variation tended to increase sharply after the initial invasion and then roughly stabilized at longer time scales (figure 3.5, figure 3.6). In our best-fit models, the maintenance of heterogeneity is a direct result of cycle dynamics behind the wave front (3.6, figure C.4). This effect occurs because populations at different stages of the tussock moth outbreak and collapse behind the wave front interact through dispersal, leading to episodic increases in variation $V_n(x)$ behind the wave front (figure 3.6, figure 3.5). Because the host-pathogen cycles in our model do not exactly repeat, small perturbations due to dispersal between asynchronous populations can cause chaotic oscillations that are partly responsible for this effect (figure 3.6, figure C.4, Sherratt [2001], Bjørnstad et al. [2002], Bennett and Sherratt [2019]). In our spatial eco-evolutionary model, variation in infection risk is thus maintained through dispersal between out-of-sync populations. We therefore conclude that the realistic fluctuations predicted by our best-fit eco-evolutionary models contribute to the long-term maintenance of variation in host infection risk.

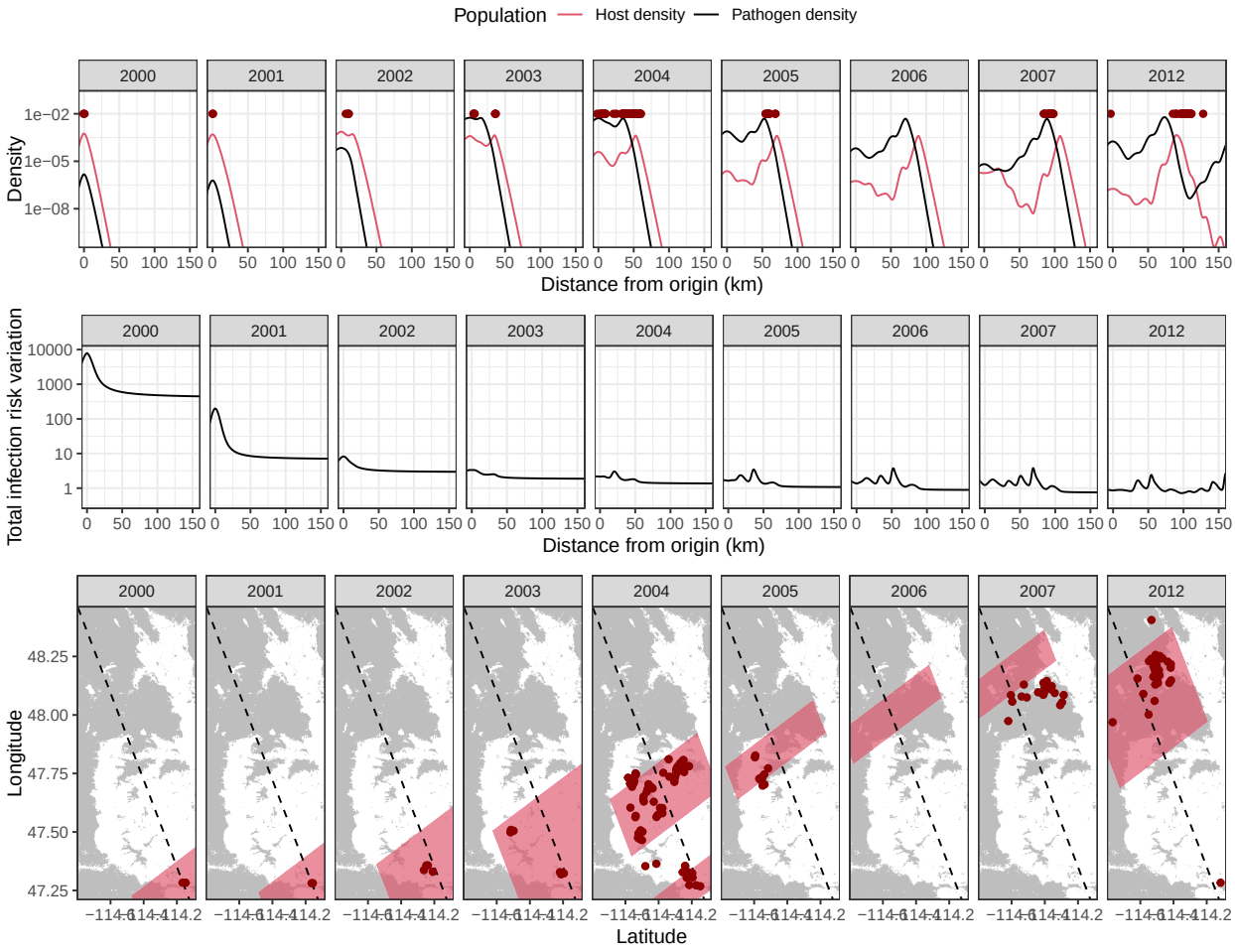

Figure 3.4: Comparison of model projections to data behind the wave front. Upper panels show the host population density and pathogen density over space for each survey year from the best-fit model $b = 0.2$, $\gamma = 0.05$, $\phi = 15$ and $\mu = 1 \times 10^{-4}$. Red points indicate the projected one dimensional location of defoliation data behind the wave front. Middle panels show the total variation of infection risk $\frac{V_n(x)}{b}$. Variation does not go to zero over time, instead fluctuating in a pattern similar to the fluctuations of host and pathogen densities. Lower panels show the areas predicted to have high host densities across a range of simulations. Red layers show host densities that were greater than or equal to the 95^{th} percentile within each of 10 simulations that varied pathogen overwintering $\phi = 5, 10, 12, 15$, or 25 and inter-generational pathogen survival probability $\gamma = 0.05$ or 0.1. The 1D simulations are projected into 2D space as bands that move in one dimension along PC1, shown as a dashed black line. Red points show observed defoliation from 2000 to 2012. Habitable forest cover is shown in grey while uninhabitable, non-forest cover is shown in white (source USFS). Additional parameters are the best values for the thin-tailed Laplace dispersal kernel (Table 3.1).

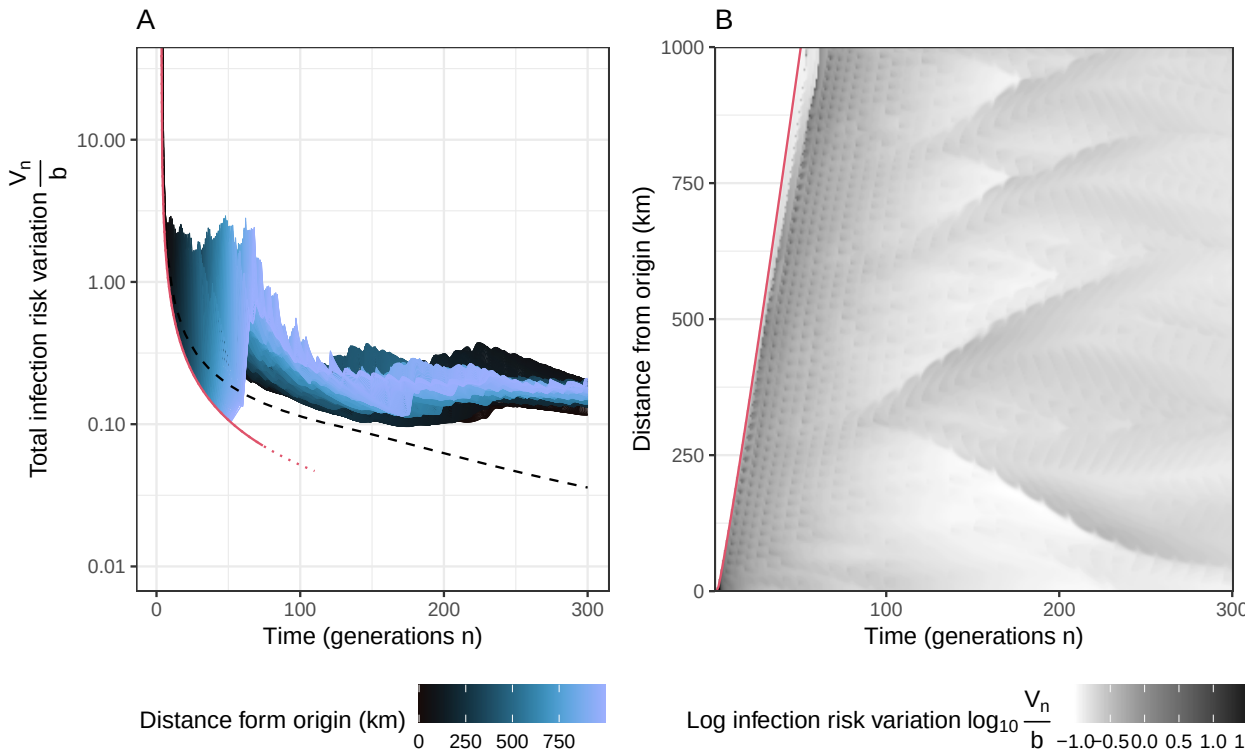

Figure 3.5: Maintenance of host variation in the eco-evolutionary model. A) In the non-spatial evolutionary model (black dashed line), variation in infection risk V_n decays to zero due to balancing selection. In contrast, in the spatial evolutionary model (colored lines) variation at first decreases but later stabilizes. During the initial wave of invasion (red line shows wave front recursion) variation decays more rapidly due to hosts escaping pathogen infection, allowing hosts with higher fecundity and higher infection risk to increase in frequency. As the pathogen wave catches up to the host invasion front, variation $V_n(x)$ increases. B) shows the birds-eye view of the same spatial simulation. Here, base reproduction $r = 1.014$, thin-tailed Laplace dispersal parameter 1.73, overwintering $\phi = 5$, pathogen survival $\gamma = 0.05$, and heritability $b = 0.2$. We use a spatial domain that is 2000 km in total width.

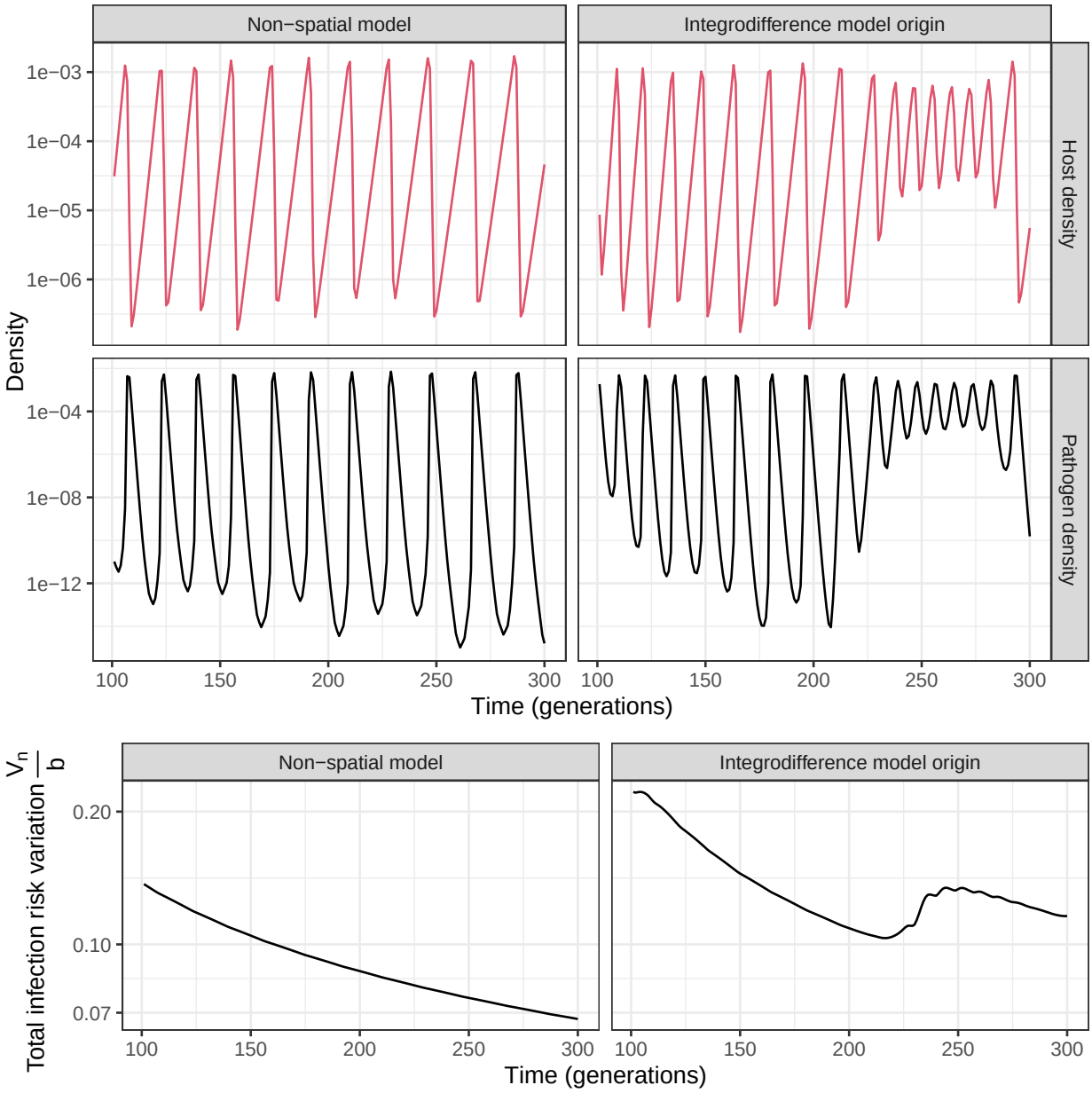

Figure 3.6: Eco-evolutionary population dynamics with and without space. Left panels show population cycles in the non-spatial eco-evolutionary model, which shows consistent cycles and decreasing variation in infection risk V_n. Right panels show the origin of $x = 0$ in a spatial integrodifference simulation. Cycle amplitudes are more variable in the spatial case and variation $V_n(0)$ fluctuates. Both simulations use base reproduction $r = 1.014$, overwintering $\phi = 5$, pathogen survival $\gamma = 0.05$, and heritability $b = 0.2$. The spatial simulation has a thin-tailed Laplace dispersal with average travel distance 1.73 km.

3.4 Discussion

Here, we show that a host-pathogen model with heritable host resistance provides a better explanation for the accelerating wave of defoliation observed during the re-establishment of Douglas-fir tussock moth outbreaks in western Montana than does a non-evolutionary model with fat-tailed dispersal. Moreover, the best evolutionary model realistically projects the maintenance of host variation behind the front and does an excellent job of predicting areas of defoliation behind the initial wave. A combination of models and data thus provides strong evidence that an eco-evolutionary host-pathogen interaction led to the rapid re-occurrence of Douglas-fir tussock moth outbreaks after a multi-decadal absence in western Montana.

Dispersal traits often receive more attention than other traits in the study of biological invasions (Olivieri et al. [1995], Shigesada and Kawasaki [1997], Kot et al. [1996], Liu and Kot [2019], Perkins et al. [2013], Brown et al. [2013a], Bennett and Sherratt [2019], Erm and Phillips [2020]). Although ballooning allows larval populations to disperse and thus escape the baculovirus, we observed that fat-tailed dispersal provided only a poor explanation of our data on tussock moth population spread. Our findings support previous conjectures that long-distance dispersal alone is unlikely to explain Douglas-fir tussock moth population spread (Mitchell [1979]). Because fat-tailed dispersal provided a meaningfully worse but not terrible fit to the wave speed data (figure 3.2), our study demonstrates the importance of comparing competing models to data in studies of accelerating invasions.

Our model also projected that variation in host infection risk will be low near the wave front (figure 3.5). Decreased variation during population expansion is often considered to be the product of dispersal bottlenecks and demographic stochasticity (Lande [1988], Miller et al. [2020]), but our model shows that reductions in variation at the wave front can alternatively be due to selection acting on traits at the wave front. Because we observed that infection risk variation decreased more sharply at the wave front than in the corresponding non-spatial model, and because host population sizes near the advancing wave front were

larger, it is unlikely that dispersal bottlenecks altered variation in infection risk in Douglas-fir tussock moth populations during expansion.

Notably, the model does a poor job of reproducing the absence of defoliation in 2006 (figure 3.4). This difference may be due to variables not included in our models that nonetheless complicate the prediction of insect population dynamics. For example, generalist parasitoids can affect tussock moth densities (Mason [1970], Mason et al. [1977], Dahlsten et al. [1977], Brookes et al. [1978], Dwyer et al. [2004], Liu et al. [2023]), while forest cover patchiness may alter host survivorship. These factors would not alter conclusions about the accelerating wave front, however, because neither parasitoids nor habitat patchiness affect wave speeds in our models (Appendix D.1). In contrast, weather fluctuations and climate shifts are well-known to have effects on advancing wave fronts (Parmesan and Yohe [2003], Diamond [2018]). This could be especially true for the Douglas-fir tussock moth, for which temperature, relative humidity, and precipitation across years have been shown to regulate outbreak severity and host reproduction (Dixon [2024]), which is closely tied to wave speed. These climatic variables may have led to a lack of defoliation observed in 2006.

Recent empirical studies have shown that, in expanding populations, genetic variation tends to be lower at the wave front than behind the wave front (Rollins et al. [2015], Williams et al. [2016], Dahirel et al. [2022]). Previous theory has largely explained this phenomenon through demogrpahic bottlenecks, whereas our work shows that it can also be explained by species interactions with evolving interaction terms. Our work may therefore be of broad applicability in large populations with increasing fecundity during invasion. Population dynamics and ecological interactions in the wake of invasions have also been poorly understood (Miller et al. [2020], Erm and Phillips [2020]), and so our result that species interactions behind the wave front can maintain variation may similarly be of general importance. Our work thus shows that models of eco-evolutionary species interactions over time and space can provide meaningful insights into the effects of evolutionary change on invasions and the

spatial pattern of population cycles.

CHAPTER 4

CONCLUSIONS AND FUTURE DIRECTIONS

In this study we provide evidence that spatial structure is important for understanding the disease ecology of Douglas-fir tussock moth. Our work at two different spatial scales uses model comparison informed by empirical data to draw conclusions about the spatial patterning of tussock moth populations.

In Chapter 2, we demonstrated that transmission hotspots drive overall pathogen dynamics and that these hotspots change over time. The initial transmission hotspots are due to patchy pathogen distribution. Later, host dispersal between low-intensity transmission coldpsots and high-intensity transmission hotspots mediates the rate at which transmission increases in coldspot sub-epizootics. We showed that this theoretically important result has consequences for the severity and extent of defoliation caused by Douglas-fir tussock moth larvae, which survive longer in coldspot refugia. This study extends previous work that could not explain defoliation extent using non-spatial baculovirus transmission models (Mihaljevic et al. [2020]) or insect density alone (Mason [1996]).

In Chapter 3, we extended spatial models to encompass multiple populations over long time periods. We determined that heritable infection risk variation generates the spatial patterning of defoliation over large landscape scales. A key feature of this spatial patterning is the accelerating wave front of high density host populations that occurred in our evolutionary models. Exceptionally long-distance dispersal was shown to not be as important for explaining the wave of Douglas-fir tussock moth re-establishment in western Montana. These findings demonstrate how spatial structure maintains heritable infection risk behind the accelerating wave front of invading host-pathogen interactions.

Both Chapters 2 and 3 make distinct assumptions about how average infection risk is distributed amongst populations. In Chapter 2, average infection risk during the epizootic varies across trees, becoming more variable over time due to differences between transmis-

sion hotspots and coldspots. Meanwhile, the initial average infection risk is assumed to be consistent across independent populations. In Chapter 3, the evolutionary integrodifference model assumes that initial average transmission risk $\bar{\nu}_n(x)$ does differ across populations and individuals at any point x are assumed to be perfectly mixing. Although these assumptions appear to be at odds with each other, the different scales of observation and heritability term b allows for consistency and leads to a general synthesis of spatial structure that describes tussock moth population dynamics.

We first note that host populations in our integrodifference model tended to have the same average infection risk $\bar{\nu}_n(x)$ when host densities were high. Additionally, the heritability term b of our integrodifference model allows for a proportion $(1-b)$ of variation that is driven by the environment, which includes local spatial structure. In contrast, all of the infection risk variation $V \equiv C^2$ in our continuous time spatial models (Chapter 2) is assumed to be intrinsic to host biology because local spatial structure is included explicitly. The consequences of this assumption can be seen when comparing the estimated infection risk variation in spatial models to that estimated in non-spatial models (figure B.4). The non-spatial had the highest estimated infection risk variation. The relative estimate of variation in our best spatial model indicates that spatial structure generates approximately 61.5% of infection risk variation. This difference shows the consistency of the model across both chapters, where the value of heritability $b \approx 0.39$ is close to the moderate level of heritability $b = 0.2$ that we found to be important for maintaining cycles behind the wave front (figure 3.4). However, because lower levels of heritability $b \geq 0.002$ provided some level of explanation for the defoliation data, there is likely some unaccounted for variables that contribute to non-heritable variation beyond spatial structure alone.

There are many mechanisms that our integrodifference models lack that could explain lower values of infection risk heritability b. First, Douglas-fir tussock moth larvae feed upon multiple tree species throughout their range (Brookes et al. [1978]). Although predominantly

feeding on Douglas-fir (*Pseudotsuga menziesii*) and true firs (*Abies* spp.), larvae have also been found feeding on other, sub-optimal foraging trees. Tree host is important as species can determine fecundity and health of larvae (Mason et al. [1977], Alfaro and Shepherd [1991], Mason [1996]). Further, it is well-known that plant diet influences interactions with baculovirus in the insect gut, with consequences for population-level transmission (Dwyer et al. [2005], Cory and Hoover [2006], Lee et al. [2006], Cory and Hoover [2006]). Douglas-fir constituted most of the forest stands from the infection rate monitoring data of Chapter 2, intermixed with grand fir in the forest stand of the Idaho and Oregon study sites and with some larvae feeding on Ponderosa pine (*Pinus ponderosa*) at the Oregon study population. The Montana study populations, near the accelerating wave populations assessed in Chapter 3, were entirely Douglas-fir, however, meaning that this variable may have little importance for explaining our estimate of heritability explaining patterns of defoliation in the area.

Second, the baculovirus transmitted in Douglas-fir tussock moth populations represents two distinct clades of nucleopolyhedroviruses (Hughes and Addison [1970]). So-called "morphotypes", for their distinguishing morphology, the two clades are highly genetically diverged (Thézé et al. [2018], Williams and Otvos [2005]). Multiple non-linear interactions could lead to increased non-heritable variation. To begin, the two morphotypes can have differing transmission rates depending on the larval diet and specialize on particular instars (Williams and Otvos [2005], Mihaljevic et al. [2020], Dixon [2024]). Further, there is also genetic variation within each morphotype, co-infection is not uncommon, and host and pathogen co-evolution are only recently coming to be understood (Williams and Otvos [2005], Fleming-Davies et al. [2015], Hudson et al. [2016], Dixon [2024]). Not only would pathogen heterogeneity contribute to the overall host infection risk variation across populations, pathogen heterogeneity would also have ramifications for transmission hotspots. Patchy pathogen distribution would be made more variable under pathogen heterogeneity. We observed a range of baculovirus morphotype compositions in our infection rate study data, but did not encode this information in

the models. Future research should therefore work to combine our small-scale dispersal and transmission hotspot model with models that have addressed morphotype by environment co-evolution models (Fleming-Davies et al. [2015], Hudson et al. [2016], Dixon [2024]).

Third, parasitoids, which kill hosts by growing inside of them, are prevalent in tussock moth populations Mason et al. [1977], Dahlsten et al. [1977], Brookes et al. [1978], Hughes et al. [2015]. Natural data on parasitoid prevalence reflects theory that show specialist parasitoids (Bjørnstad et al. [2002]) and generalist predators (Dwyer et al. [2004]) can affect Lepidopteran population dynamics. Parasitoids can grow in any stage of development (eggs, larvae, or pupae), which can alter relative mortality due to other factors such as baculovirus infection (Mason et al. [1977]). For example, if larval parasitoids were present, susceptible host larvae will be removed from the population during the epizootic. In reference to Chapter 2, this would mean that coldspot sub-epizootics may not show increased late-season transmission. In contrast, if egg parasitoids were present, reduced numbers of emerging larvae could decrease the number of exposed first-instar larvae and thereby increase the patchiness of pathogen distribution. It is then trivial to note that these local parasitoid impacts would increase the environmental variation of infection risk, decreasing the heritability $b = 0.39$ approximated from differences between posterior estimates of C^2. This is especially true since patchy spatial environments contribute to the variation of specialist parasitoids more than generalist predators (Hughes et al. [2015]). In general then, adding non-linear host-parasitoid interactions would exacerbate the complexity of the host-pathogen interactions (Dwyer et al. [2004]). Parasitoids may therefore be able to explain gaps between heritability estimates that our eco-evolutionary model cannot explain. We should likely consider these effects across scales and the consequences for heritable host variation.

Finally, although we have seen that environmental noise is not informative for single epizootics (Chapter 2), environmental differences over larger spatial scales and climate change over longer time periods will affect Douglas-fir tussock moth populations (Shepherd

et al. [1988], Dixon [2024]). Despite baculovirus transmission being generally unaffected by weather, climate change effects on Douglas-fir tussock moth populations will also likely have consequences for the baculovirus through either immunity and reproduction (D'Amico and Elkinton [1995], Cory and Myers [2003]. Further, plant diet and baculovirus infection interact; as forest composition and leaf chemical composition shift under a changing climate, we will also need models that account for the interactions of climate, plant diet, and pathogen variation in addition to spatial variability (Cory and Hoover [2006], Elderd and Dwyer [2019], Dixon [2024]). Although significant recent research has enhanced our understanding in these areas (Dixon [2024]), the implications of these interactions for initial pathogen densities and dispersal-mediated hotspot shifts are not clear. Climate change will lead to host range shifts (Diamond [2018], Dixon [2024]), but the speed at which these expansions will occur is uncertain. We've characterized the distance distribution in one such area that showed a novel range expansion where defoliation was not previously detected (Section D.2.2). Therefore, the projections of Chapter 3 have to be combined with range shift models that account for climatic variables in order to predict the future spatial patterning of Douglas-fir tussock moth populations.

A key piece of data missing from our analyses is genetic relatedness over space, which would more clearly identify the rate of spread. Genetic data can be used to estimate population mixing and dispersal rates (Osmond and Coop [2021]), which would allow for additional evidence supporting estimates of dispersal from accelerating wave defoliation data. Additionally, the degree of genotypic variation present in both host and baculovirus samples could provide insights into phenotypic variation of heritable infection risk. For example, genetic information would complement mating experiments that test the heritability and cost of infection risk or allow for the identification of loci involved in fecundity and infection risk traits (Section D.2, Páez et al. [2017]). Thus, the synthesis of genetic data, mating experiments, and climatic host range models would aid in our ability to understand the variability inherent

in tussock moth population cycles and better predict the spatial patterning of defoliation for better insect outbreak management.

Appendices

APPENDIX A

INFECTION RISK DISTRIBUTIONS OVER CONTINUOUS SPACE AND CONTINUOUS TIME

In our core SEP model, we assume that hosts vary in their susceptibility (Dwyer et al. [2000], Mihaljevic et al. [2020]). Host heterogeneity is denoted by the coefficient of variation in the distribution of infection risk C. The coefficient of variation is derived from a moment closure approximation over the continuous distribution of host infection risks $S(\nu, t)$ yielding mean transmission risk $\nu(t)$ and the fixed shape parameter C. In this model, more susceptible individuals are infected with the virus at a faster rate. From our moment closure approximation, only the mean transmission risk changes over time, while the ratio of the variance to the squared mean, C^2, remains constant. In a non-spatial model, we can integrate $\frac{d\nu}{dt}$ and we end up with the term

$$\nu(t) = \bar{\nu} \left(\frac{S(t)}{S(0)} \right)^{C^2} \tag{A.1}$$

where $\bar{\nu} \equiv \nu(0)$ and the effective transmission rate $\nu(t)$ is shown to decrease over time as $S(t)$ is strictly decreasing and C is strictly positive. The rate of decrease in transmission due to the incorporation of host heterogeneity is determined by C^2 such that a higher coefficient of variation of infection risk C leads to faster decline in transmission and shorter epizootics with higher host survivorship.

Spatial heterogeneity contributes to heterogeneity in individual infection risk (Keeling and Rohani [2008], Elderd et al. [2022]). Therefore, we have to close the moments of $S(\nu, x, t)$ bearing in mind this new assumption. It is worth reproducing the moment closure without space here first, despite its summary above and presence in other publications, to simplify the understanding of notation used in the spatial moment closure.

A.1 Non-spatial moment closure approximation

We can use a simple SIR model to demonstrate the non-spatial moment closure. The toy model for our demonstration is thus

$$\frac{\partial S}{\partial t} = -\beta SI, \tag{A.2}$$

$$\frac{dI}{dt} = I\int_0^\infty \beta S(\beta,t)d\beta - \gamma I. \tag{A.3}$$

where a partial derivative over S shows how all susceptible host populations distributed according to their transmission risk β change over time. The infectious class I is produced according to the expectation of this transmission risk in the susceptible population.

We define the j^{th} moments of the distribution of $S(\beta,t)$ as follows:

$$s_j = \int_0^\infty \beta^j S(\beta,t)d\beta, \tag{A.4}$$

$$m_j = \frac{\int_0^\infty \beta^j S(\beta,t)d\beta}{\int_0^\infty S(\beta,t)d\beta}. \tag{A.5}$$

$$\tag{A.6}$$

Most of what we care about in the distribution of susceptibles is in the lower moments, where $s_0(t)$ is the total susceptible population and $m_1(t)$ is the expected transmission risk of the susceptible class at time t. This simplifies what we define as the rate of change in infectious class I in equation (A.3), where we now have

$$\frac{dI}{dt} = I\frac{\int_0^\infty S(\beta,t)d\beta}{\int_0^\infty S(\beta,t)d\beta}\int_0^\infty \beta S(\beta,t)d\beta - \gamma I. \tag{A.7}$$

$$= Is_0(t)m_1(t) - \gamma I. \tag{A.8}$$

We would like to do simplify equation (A.2) as well, but we wind up with an infinite chain of lower moments that depend on higher moments.

$$
\begin{aligned}
s_j' &= \frac{\partial}{\partial t}\int_0^\infty \beta^j S(\beta,t)d\beta, && \text{(A.9)}\\
&= \int_0^\infty \beta^j \frac{\partial S}{\partial t}d\beta, && \text{(A.10)}\\
&= \int_0^\infty -\beta^{j+1} SI d\beta, && \text{(A.11)}\\
&= -I s_{j+1} && \text{(A.12)}\\
&= -I m_{j+1} s_0 && \text{(A.13)}
\end{aligned}
$$

We "close" these moments before s_∞ by assuming that the CV is constant

$$
\begin{aligned}
\text{CV} &= \frac{\sqrt{\text{Var}[x]}}{E[x]}, && \text{(A.14)}\\
&= \frac{\sqrt{E[x^2]-E[x]^2}}{E[x]}, && \text{(A.15)}\\
&= \frac{\sqrt{m_2-m_1^2}}{m_1} && \text{(A.16)}
\end{aligned}
$$

and we therefore can use algebra to remove m_2 from our final system of equations. We use the quotient rule to define m_1'

$$
\begin{aligned}
m_1' &= \frac{s_1' s_0 - s_0' s_1}{s_0^2} && \text{(A.17)}\\
&= \frac{(-I s_2)s_0 - (-I s_1)s_1}{s_0^2} && \text{(A.18)}\\
&= -I\frac{s_0 s_2 - s_1^2}{s_0^2} && \text{(A.19)}\\
&= -I\Big(\frac{s_2}{s_0} - \big(\frac{s_1}{s_0}\big)^2\Big). && \text{(A.20)}\\
&= -I\Big(m_2 - m_1^2\Big). && \text{(A.21)}
\end{aligned}
$$

Noting that

$$C^2 = \frac{m_2 - m_1^2}{m_1^2} \tag{A.22}$$

$$m_2 - m_1^2 = m_1^2 C^2 \tag{A.23}$$

and remembering our definition in equation A.13, we can write our model accounting for host heterogeneity in susceptibility as

$$\frac{ds_0}{dt} = -m_1 I s_0 \tag{A.24}$$

$$\frac{dm_1}{dt} = -m_1^2 C^2 I \tag{A.25}$$

Using notation from our SEP model, where

$$S \equiv s_0 \tag{A.26}$$

$$\nu \equiv m_1, \tag{A.27}$$

we have completed the moment closure with

$$\frac{dS}{dt} = -\nu S P \tag{A.28}$$

$$\frac{dP}{dt} = \nu S P - \mu P \tag{A.29}$$

$$\frac{d\nu}{dt} = -\nu^2 C^2 P \tag{A.30}$$

A.2 Moment closure in space

We are now looking to close moments of a PDE system that distributes populations over space. Again using our toy model SIR notation, we have $S(\beta, x, t)$ and $I(x, t)$, where x

is one-dimensional space. Two-dimensional calculations are more algebraically-intense, but produce the same system of equations.

Our initial model for which we need a moment closure is then

$$\frac{\partial S}{\partial t} = -\beta SI + D\frac{\partial^2 S}{\partial x^2} \tag{A.31}$$

$$\frac{\partial I}{\partial t} = I\int_0^\infty \beta S(\beta, x, t)d\beta - \gamma I \tag{A.32}$$

where we conveniently do not need to account for the diffusion of infectious cadavers, although calculations would be the same for an analogous communicable disease with live infectious individuals. Following our earlier moment closure approach, we have

$$\frac{\partial s_0}{\partial t} = \frac{\partial}{\partial t}\int_0^\infty S(\beta, x, t)d\beta \tag{A.33}$$

$$= \int_0^\infty \frac{\partial S}{\partial t}d\beta \tag{A.34}$$

$$= \int_0^\infty \left(-\beta SI + D\frac{\partial^2 S}{\partial x^2}\right)d\beta, \tag{A.35}$$

$$= -I\int_0^\infty \beta S d\beta + D\frac{\partial^2 \int_0^\infty S d\beta}{\partial x^2} \tag{A.36}$$

$$= -m_1 I s_0 + D\frac{\partial^2 s_0}{\partial x^2} \tag{A.37}$$

Now that we have added a diffusion term, the expression for the derivative of each successive moment is not identical to the last as in equation A.13. Even calculating the next moment s_1' is cumbersome

$$\frac{\partial s_1}{\partial t} = \frac{\partial}{\partial t}\int_0^\infty \beta S(\beta,x,t)d\beta \tag{A.38}$$

$$= \int_0^\infty \beta \frac{\partial S}{\partial t} d\beta \tag{A.39}$$

$$= \int_0^\infty \beta \left(-\beta SI + D\frac{\partial^2 S}{\partial x^2}\right) d\beta, \tag{A.40}$$

$$= -Is_2 + D\frac{\partial^2 s_1}{\partial x^2} \tag{A.41}$$

$$= -Is_2 + D\frac{\partial^2 \left(m_1 s_0\right)}{\partial x^2} \tag{A.42}$$

$$= -Is_2 + D\left(s_0 \frac{\partial^2 m_1}{\partial x^2} + 2\frac{\partial m_1}{\partial x}\frac{\partial s_0}{\partial x} + m_1 \frac{\partial^2 s_0}{\partial x^2}\right). \tag{A.43}$$

we are, however interestedf in $m_1(x,t)$, not only $s_1(x,t)$, thus we again take the quotient rule derivation

$$\frac{\partial m_1}{\partial t} = \frac{\partial}{\partial t}\left(\frac{s_1}{s_0}\right) \tag{A.44}$$

$$= \frac{\frac{\partial s_1}{\partial t}s_0 - \frac{\partial s_0}{\partial t}s_1}{s_0^2}, \tag{A.45}$$

$$= s_0\left(-Is_2 + D\left(s_0\frac{\partial^2 m_1}{\partial x^2} + 2\frac{\partial m_1}{\partial x}\frac{\partial s_0}{\partial x} + m_1\frac{\partial^2 s_0}{\partial x^2}\right)\right)/s_0^2$$
$$-s_1\left(-m_1 I s_0 + D\frac{\partial^2 s_0}{\partial x^2}\right)/s_0^2 \tag{A.46}$$

$$= -m_1^2 C^2 I + D\left((s_0^2/s_0^2)\frac{\partial^2 m_1}{\partial x^2} + 2(s_0/s_0^2)\frac{\partial m_1}{\partial x}\frac{\partial s_0}{\partial x} + ((m_1 s_0)/s_0^2 - s_1/s_0^2)\frac{\partial^2 s_0}{\partial x^2}\right) \tag{A.47}$$

$$= -m_1^2 C^2 I + D\left(\frac{\partial^2 m_1}{\partial x^2} + (2/s_0)\frac{\partial m_1}{\partial x}\frac{\partial s_0}{\partial x}\right) \tag{A.48}$$

$$= -m_1^2 C^2 I + \frac{D}{s_0}\left(s_0\frac{\partial^2 m_1}{\partial x^2} + 2\frac{\partial m_1}{\partial x}\frac{\partial s_0}{\partial x}\right) \tag{A.49}$$

The final system of equations is thus

$$\frac{\partial S(x,t)}{\partial t} = -m_1 IS + D\frac{\partial^2 S}{\partial x^2} \tag{A.50}$$

$$\frac{\partial m_1(x,t)}{\partial t} = -m_1^2 C^2 I + \frac{D}{s_0}\left(s_0\frac{\partial^2 m_1}{\partial x^2} + 2\frac{\partial m_1}{\partial x}\frac{\partial s_0}{\partial x}\right) \tag{A.51}$$

And altogether with our SEP model notation, we end up with the final PDE system presented in the main text

$$\frac{\partial S(x,t)}{\partial t} = -\nu PS + D\frac{\partial^2 S}{\partial x^2} \tag{A.52}$$

$$\frac{\partial \nu(x,t)}{\partial t} = -\nu^2 C^2 P + \frac{D}{S}\left[S\frac{\partial^2 \nu}{\partial x^2} + 2\frac{\partial \nu}{\partial x}\frac{\partial S}{\partial x}\right] \tag{A.53}$$

$$\frac{\partial E_1(x,t)}{\partial t} = \nu PS - m\delta E_1 + D\frac{\partial^2 E_1}{\partial x^2} \tag{A.54}$$

$$\frac{\partial E_i(x,t)}{\partial t} = m\delta E_{i-1} - m\delta E_i + D\frac{\partial^2 E_i}{\partial x^2} \quad (i \in [2,m]) \tag{A.55}$$

$$\frac{\partial P(x,t)}{\partial t} = m\delta E_m - \mu P \tag{A.56}$$

$$\tag{A.57}$$

APPENDIX B

FITTING SPATIAL MODELS TO INFECTION RATE DATA USING AN ADAPTED MCMC ALGORITHM

B.1 Likelihood incorporation of sample error with reflections on data

Binomial probability mass functions can be used to calculate the probability of observing a given number of hosts infected per number of hosts collected. Often in natural systems, we know that count data are overdispersed compared to a binomial distribution, meaning that the variance of observed counts is higher than would be expected under a binomial distribution. To account for overdispersion, beta-binomials are frequently invoked to describe the distribution of count data Young-Xu and Chan [2008]. The beta-binomial assumes that the number of insects infected k (out of n collected insects) depends on the true fraction of hosts infected p; however, it further assumes that p varies and is itself a random variable. For example, each sample i can have its own true fraction of infected insects, p_i, distributed according to a beta distribution with shape parameters α and β, denoted $B(\alpha, \beta)$, taking the form

$$f(k_i|n_i, \alpha, \beta) = \int_0^1 \text{Bin}(k_i|n_i, p_i)\text{Beta}(p_i|\alpha, \beta)dp_i \tag{B.1}$$

$$= \binom{n_i}{k_i} \frac{\mathcal{B}(k_i + \alpha, n_i - k_i + \beta)}{\mathcal{B}(\alpha, \beta)} \tag{B.2}$$

where $\mathcal{B}(\alpha, \beta)$ is the Beta function, $\mathcal{B}(\alpha, \beta) = \frac{\mathcal{G}(\alpha)\mathcal{G}(\beta)}{\mathcal{G}(\alpha+\beta)}$, and $\mathcal{G}$ is the Gamma Function, $\mathcal{G}(z) = \int_0^\infty t^{z-1}e^{-t}dt$.

For our non-spatial model, we thus have a beta-binomial distribution that has expectation $\mathbb{E}[p_i] = \frac{\alpha}{\alpha+\beta}$ and variance $V(p_i) = \mathbb{E}[p_i](1-\mathbb{E}[p_i])\gamma$. We can see that γ is the overdispersion.

Overdispersion γ is bounded between 0 and 1 because $\gamma = \frac{1}{\alpha+\beta+1}$. If $\gamma = 0$ there is no variance, meaning that we recover the binomial distribution because p is always exactly equal to $\mathbb{E}[p_i]$, whereas if $\gamma = 1$ then the overdispersion is at its maximum and the variance of the beta distribution with mean $\mathbb{E}[p_i]$ is greatly increased.

We observed that it is easier to fit a log-log inverse overdispersion because we can place a wider range on the parameter during model fitting and give equal weight to small, non-zero values and values approaching maximal overdispersion $\gamma = 1$. Therefore we define

$$\gamma = \frac{1}{\exp(\exp(\hat{\gamma}))}, \tag{B.3}$$

where the fitted parameter $\hat{\gamma}$ is unbounded, with values of $-\infty$ being maximally overdispersed and values of ∞ possessing zero overdispersion. We can therefore define the beta distribution of p_i according to the overdispersion γ and mean fraction infected p, which is taken from a given time point in the non-spatial model simulation as

$$p(t) = \frac{\sum_{j=1}^{m} E(t)_j}{S(t) + \sum_{j=1}^{m} E(t)_j}. \tag{B.4}$$

Defining $\alpha = p\gamma^{-1}$ and $\beta = (1-p)\gamma^{-1}$, we can capture a range of distribution behaviors.

B.1.1 Bounded kernel density estimators

In contrast to the non-spatial model, our spatial models assume the fraction infected p_i to be distributed according to the observed values over space and time. Instead of a beta distribution then, we construct a kernel density estimator (KDE) of the histogram of fractions infected. Kernel density estimators are smoothing approximations to the full distribution of a variable given some sample. Some number n of data points are given as inputs and the output is a density estimate that integrates to 1 over the whole interval of the distribution $(0, 1)$. The likelihood functions of our spatial models are then generally of the form

$$f(k_i|n_i, \vec{\theta}) = \int_0^1 \text{Bin}(k_i|n_i, p) K_x(p, t) dp, \tag{B.5}$$

where $K(p, t)$ is the kernel density estimator of the distribution of fraction infected over space at time t.

Fundamentally kernel density estimates are built by a summation of distributions centered at each data point. There are two hyperparameter components to a given kernel density estimate. These are the bandwidth h, which is a measure related to the variance of the distribution replicated and centered at each data point, and, in practical applications, the integration step g, the evenly spaced units over which the density is calculated so that integrating it using numerical methods yields 1. These two hyperparameters are optimized independently of each other, with h scaling as $n^{-\frac{1}{5}}$ and g typically being set to some sufficiently small value so that there are 10^2 to 10^3 steps over the data range plus or minus $m \times h$ (Chen [1999]).

Typically, we assumed that the data are unbounded and that Gaussian distributions with $\sigma = h$ are centered at each data point. This means that the kernel density estimate $K(X)$ is equal to

$$K(X) = \frac{1}{n} \sum_1^n \mathcal{N}(x_i, h) \tag{B.6}$$

However, these calculations do not work for bounded data. For example, if we consider a beta-distributed variable $Y \sim \text{Beta}(\alpha, \beta)$, normally-distributed approximations will give non-zero density for observations outside the range the data can take on. To account for this issue, we have to change the distribution centered at each point and adjust our calculation of the bandwidth h.

$$h = \min\left(\sigma_X + \epsilon, \frac{\mathrm{IQR}(X)}{1.34}\right)\left(\frac{4n}{3}\right)^{-\frac{2}{5}} \tag{B.7}$$

$$K(X) = \frac{1}{n}\sum_{i=1}^{n} g(x_i, h) \tag{B.8}$$

where

$$g(x,h) = \begin{cases} \mathrm{Beta}\left(x|\rho(x,h), \frac{1-x}{h}\right), & x \leq 2h \\ \mathrm{Beta}\left(x|\frac{x}{h}, \rho(1-x,h)\right), & x \geq 1-2h \\ \mathrm{Beta}\left(x|\frac{x}{h}, \frac{1-x}{h}\right), & \text{otherwise} \end{cases} \tag{B.9}$$

$$\rho(x,h) = 2h^2 + 2.5 - \sqrt{4h^4 + 6h^2 + 2.25 - x^2 - \frac{x}{h}} \tag{B.10}$$

The average of all Beta distributions $g(x,h)$ is an unbiased estimator of the bounded density $K(X)$. If only one point in our spatial simulation had non-zero host density, we instead set $K(X)$ to be a Dirac delta function with point density at the fraction infected observed in the surviving population.

During our spatial simulations, we take the estimate of the fraction infected at each point in space, from the fraction summation formula in equation B.4, and used these values to generate the bounded density $K(X)$ from 0 to 1. We then integrate using the binomial likelihood function $f(k_i|n_i, \vec{\theta})$. We used the trapezoidal rule with 401 integration steps to integrate the binomial likelihood over density estimator $K(X)$.

Once we calculated the value of the pointwise likelihood $f(k_i|n_i, \vec{\theta})$ from a given simulation for all of our data, we take the sum of the log likelihood scores as the final likelihood for a given parameter set. During model fitting, we used one model realization per likelihood score calculation and during log pointwise predictive density calculation we used 64

realizations per likelihood calculation.

B.1.2 Temporal overdispersion is better captured by spatial models due to improved sample error estimation

It is important to note that the construction of $K(X)$ allows for overdispersion to vary temporally while the use of hyperparameter γ in the beta-binomial non-spatial likelihood does not allow for changes in overdispersion over time.

If $\gamma > p$, then the beta distribution is bimodal, otherwise the distribution is unimodal. This means that during times with low infection rates in a fixed overdispersion model, the distribution of fraction infected $p(t)$ will be bimodal for low values of fraction infected. This is the opposite case in our spatial model, where the bimodality, and thus overdispersion, is most pronounced during the middle to late season of the epizootic. Therefore, the fitted overdispersion values in our spatial models provided much better fits to those overdispersion values bootstrapped from our infection data (figure B.1).

B.2 PCA-adjusted MCMC provides computationally-efficient convergence

B.2.1 Dimensionally-reduced Gibbs sampler

Sampling from high-dimensional posterior distributions $\pi(\mathbf{w}|\mathbf{x})$ can be challenging with standard MCMC algorithms due to potential correlations between the parameters $\mathbf{w}$ Kennedy and Dwyer [2018]. These correlations can lead to poor mixing and slow convergence. To mitigate this issue with our Gibbs sampler, we first generated a reasonable proposal distribution $\mathbf{w}$ using linesearch and then used principal component analysis (PCA) transform $h(\mathbf{w})$ to account for correlations between parameters (algorithm 2, Kennedy and Dwyer [2018]). This gave us proposed values in terms of the principal components, which are orthogonal

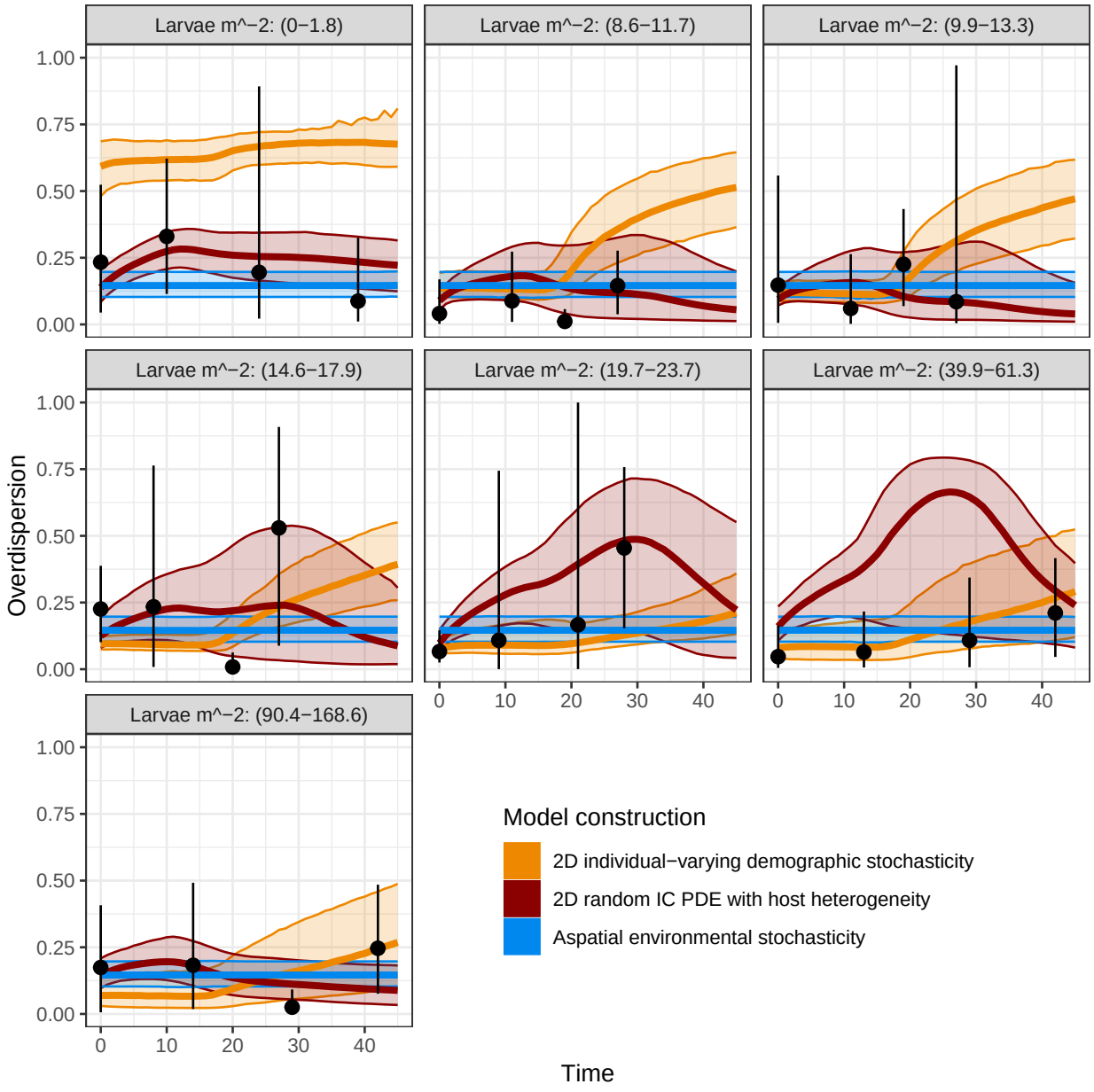

Figure B.1: Posterior estimates of overdispersion over time (ribbons) versus bootstrapped smaple data (points). Temporal variance in oversdispersion seems to be important and PDE matches data. Beta-binomial with fixed overdispersion cannot replicate data appropriately.

and therefore uncorrelated by construction and allows for better mixing. We then repeated this process iteratively to increasingly improve un-correlated proposal distributions.

We generated our first proposal distributions by using 500 line search algorithms and taking the parameter sets in the top 40% of posterior probabilities, which forms a rough

posterior surface. We then transform these line search outputs using PCA and use this as a proposal distribution following algorithm 2. We then take the posterior from our first round of MCMC, using 5000 iterations and a burn-in period of two integrated autocorrelation times (IATs). This prevents inclusion of overdispersed initial parameter suggestions. We then do another round of MCMC, transforming the posterior using a second PCA and run 10000 iterations, which we show to be approximately the IAT squared in all of our model construction MCMCs. In figure B.2 we show the proposal distribution and posterior for our two rounds of MCMC, which allowed us to in a sense parallelize MCMC in time.

We initialized our state $\mathbf{r}^{(0)}$ by independently drawing the principal component coefficients from $\mathcal{N}(0, \sigma_i)$, with variances being multiplied by 1.2 to overdisperse our initial sample. Applying h^{-1} to $\mathbf{r}^{(0)}$ yielded the corresponding parameter vector $\boldsymbol{\theta}^{(0)}$ in the original space, while still being expressed in an uncorrelated basis. This helped eliminate potential issues with correlated initial conditions. We then performed dimensionally-reduced Gibbs sampling in the principal component space as follows. At each iteration t, we cycled through each principal component j, proposing updates by drawing r'_j from $\mathcal{N}(0, \sigma_j)$. Crucially, we only sample each principal component in proportion to the total variance that it can explain in the proposal distribution. This means that lower order principal components are re-sampled less frequently for a more efficient exploration of the high-dimensional distribution space, thus saving simulation time of more similar parameter sets. Over MCMC posterior-proposal iterations, the distribution of variance explained by lower order components becomes more even and acceptance ratios approach ideal mixing (figure B.5), resulting in more frequent draws from these components relative to first and second order principal components.

After computing the proposed full parameter vector $\boldsymbol{\theta'} = h^{-1}(\mathbf{r'})$, we evaluated the corresponding posterior $\pi(\boldsymbol{\theta'}|\mathbf{x})$. We then used the standard Metropolis-Hastings acceptance ratio of posteriors and proposal densities. We only used one realization of each model per likelihood score calculation. To avoid the winner's curse fallacy common to stochastic mod-

els, where exceedingly good likelihood scores are accepted too quickly, we initially rejected acceptance ratios greater than one. For these parameter sets, which would otherwise be accepted under a standard Gibbs sampler, we re-calculated the likelihood and then followed the standard protocol for the second acceptance ratio, making this sampler cautious. We still followed the standard approach to accept ratios less than one with the probability of acceptance being the ratio in order to avoid rejecting slightly worse parameter sets. If a proposed component update was accepted, we updated $r_j^{(t)}$, $\boldsymbol{\theta}^{(t)}$, and our estimated posterior $\hat{\pi}$ (algorithm 2).

By performing most of the algorithm's operations in the orthogonal principal component space, we were able to effectively decouple the correlated parameters and sample from the full posterior distribution much more efficiently than could be achieved with standard MCMC approaches on the original correlated space.

Algorithm 1: Initialize Gibbs Sampler

Define $h(w)$ as the PCA transform of $n-$dimensional posterior $\pi(w|x)$;
Define $\vec{\sigma}$ as the vector of length n where σ_i denotes the standard deviation of principle component i from $h(w)$;
Define $\vec{v}$ as vector of length n where v_i denotes the variance explained by principal component i;
Initialize $r^{(0)}$ from $h(w)$ where $r_i \sim \mathcal{N}(0, \sigma_i)$;
Initialize $\theta^{(0)} \leftarrow h^{-1}(r^{(0)})$;
Initialize $\hat{\pi} \leftarrow \pi(\theta^{(0)}|x)$;

B.2.2 Convergence diagnostics

In table B.1, we show the priors used and list of parameters across all models.

The MCMC chains showed improved mixing over MCMC proposal-posterior iterations. From our best spatial model, we show some examples for the parameters $\bar{\nu}$, μ, δ, and C, which were the only parameters in all of our models that were not host or pathogen densities (figure B.3). We also show the respective Gelman-Rubin $\hat{R}$ statistics for each chain (figure

Algorithm 2: Iterative PCA Gibbs Sampler

for *MCMC iteration* $t \in (1, n)$ **do**
- Store $r' \leftarrow r^{(t-1)}$;
- **for** *Principal component* $j \in (1, n)$ **do**
  - **if** $(t \bmod \lfloor v_0 v_j^{-1} \rfloor) == 0$ **then**
    - Propose $r'_j \sim \mathcal{N}(0, \sigma_j)$;
    - Set $\theta' = h^{-1}(r')$;
    - Calculate $\pi(\theta'|x, s_1)$ with random seed s_1;
    - Calculate criterion $\rho \equiv \frac{\pi(\theta'|x)}{\hat{\pi}} \times \frac{p\left(r_j^{(t-1)}|\sigma_j\right)}{p\left(r'_j|\sigma_j\right)}$;
    - Draw random number $u_1 \in (0, 1]$;
    - **if** $\rho < u_1$ **then**
      - Reject proposal and store $r_j^{(t)} \leftarrow r_j^{(t-1)}$;
      - Re-store $r'_j \leftarrow r_j^{(t-1)}$;
    - **else if** $\rho < 1$ **then**
      - Accept $r_j^{(t)} \leftarrow r'_j$;
      - Store $\theta^{(t)} \leftarrow \theta'$;
      - Re-calculate and store $\hat{\pi} \leftarrow \pi(\theta', s_2|x)$ with random seed $s_2 \neq s_1$;
    - **else**
      - Re-calculate $\pi(\theta'|x, s_2)$ with random seed $s_2 \neq s_1$;
      - Re-calculate criterion $\rho = \frac{\pi(\theta'|x)}{\hat{\pi}} \times \frac{p\left(r_j^{(t-1)}|\sigma_j\right)}{p\left(r'_j|\sigma_j\right)}$;
      - Draw random number $u_2 \in (0, 1]$;
      - **if** $\rho < u_2$ **then**
        - Reject proposal and store $r_j^{(t)} = r_j^{(t-1)}$;
        - Re-store $r'_j \leftarrow r_j^{(t-1)}$;
      - **else**
        - Accept $r_j^{(t)} \leftarrow r'_j$;
        - Store $\theta^{(t)} \leftarrow \theta'$;
        - Store $\hat{\pi} \leftarrow \pi(\theta'|x, s_2)$
      - **end**
    - **else**
      - $r_j^{(t)} \leftarrow r_j^{(t-1)}$;
    - **end**
  - **end**

end

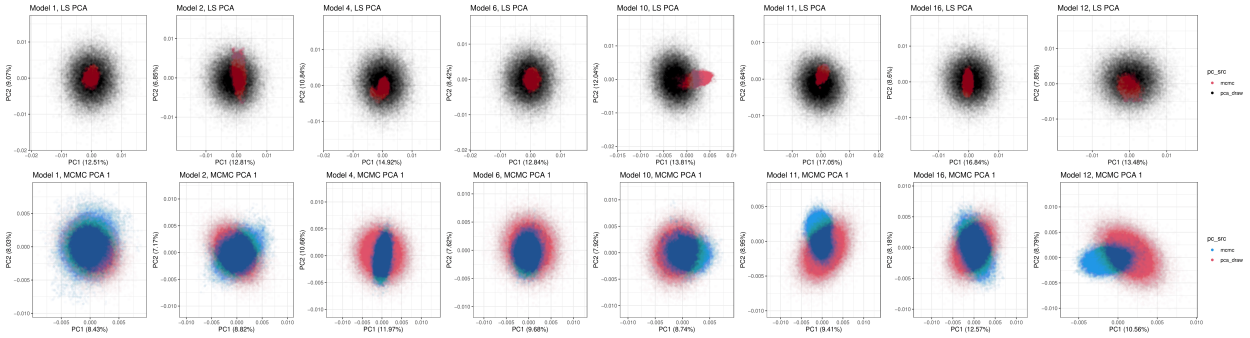

Figure B.2: Each column represents our fitting routine proposals and posteriors for different model constructions. Black points show the proposal distribution in PCA space generated by our linesearch routine and red overlaid points in the top panels show the MCMC posterior from these proposals. In the bottom panels, Red again is the MCMC posterior, this time as a proposal distribution, and our second posterior distribution from MCMC in PCA space is overlaid in blue. In most cases, the second round of MCMC aided in convergence but did not qualitatively alter the proposal distribution, except in the right-most panel of Model 12, the PDE with environmental stochasticity.

Parameter	Description	Prior distribution shape	Prior parameters	Units	Source or rationale
c_1	Diffusion constant	Uniform	lower = 0, upper = 0.37	individuals per day per tree^2	-
c_2	Michaelis-Menten growth constant	Normal	mean = 7.8, sd = 1.77	days	Development data during study
$\bar{\nu}$	Average initial infection risk	Log-normal	logmean = -4.82, sd = 0.59	individuals per tree per day	Mihaljevic et al. [2020]
C	Coefficient of variation over infection risk	Log-normal	logmean = 0.047, sd = 0.375	unitless	Mihaljevic et al. [2020]
δ	Mortality rate	Gamma	shape = 200, rate = 0.06	individuals per day	Mihaljevic et al. [2020]
μ	Pathogen decay rate	Uniform	lower = 0, upper = 0.6	individuals per day	-
σ	Standard deviation of environmental noise	Gamma	shape = 2, scale = 3	unitless	Reasonable levels for variability
γ	Beta distribution overdispersion	Uniform	lower = 0, upper = 148.4	unitless	-
$\bar{S}_0$	Initial average host population	Normal	Population-specific	hosts per tree	Population-level branch densities at first sample
$\bar{P}_0$	Initial average pathogen population	Uniform	lower = 0.0037, upper = 148.4	cadavers per tree	-
t_0	Time of first sample	Log-normal	logmean = 0, sd = 0.5	days	Second instar proportion at first sample

Table B.1: Priors and parameter description for all models

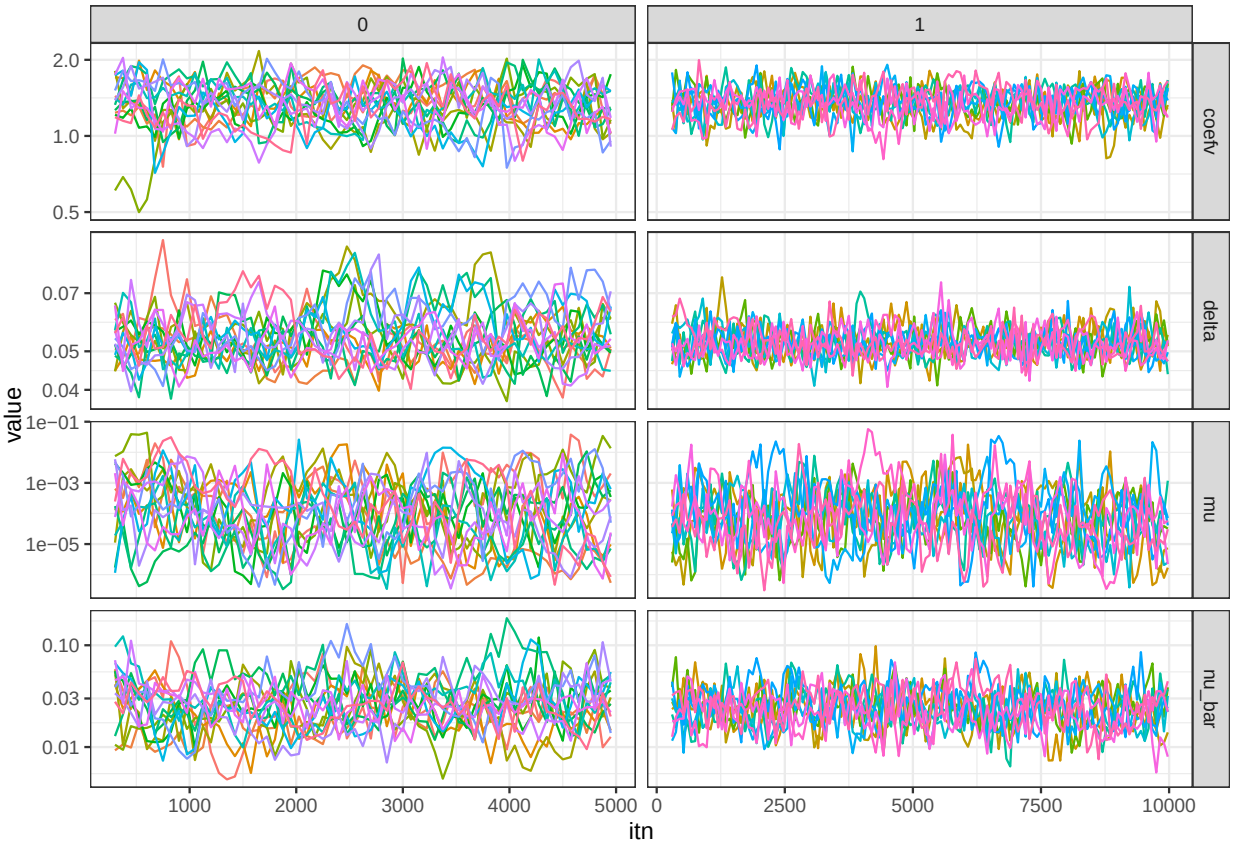

Figure B.3: Example of four parameters from our best spatial model during iterative MCMC thinned by the IAT. The second MCMC iteration shows better mixing and a tighter posterior distribution due to the improved proposal distribution generated from the previous MCMC iteration posterior. Scales are consistent across MCMC iterations but are different across parameters to improve visualization.

B.5). In the first round of MCMC, $\hat{R}$ values indicate poorer mixing as compared to the acceptable values shown in round 2. Acceptance ratios were also improved towards ideal mixing, approaching the acceptance of $\sim$ 25% of proposed values in our second round. These acceptance ratios indicate that the proposal distribution of our Gibbs sampler closely resembled the true posterior distribution. Additionally, our chains were longer than the squared estimated sample size, based on integrated auto-correlation time, adding to our confidence in the posterior estimates from each MCMC output.

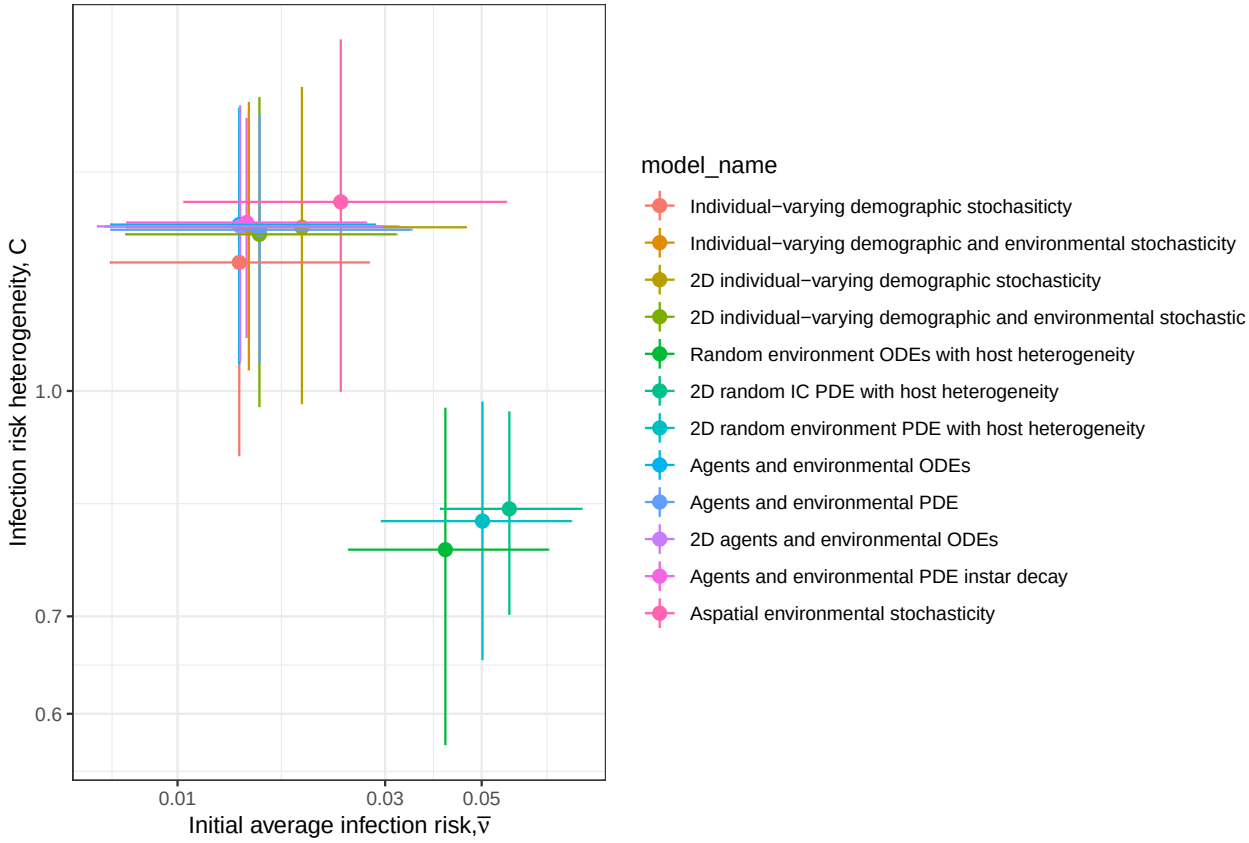

Figure B.4: Differential equations models yielded posterior distributions for transmission parameters that were highly divergent from agent-based posteriors. Notably, C was estimated to be less than 1 for differential equations, which qualitatively changes the long-term dynamics of the system to produce cycles. The non-spatial model, however, estimated a much higher coefficient of variation in infection risk C.

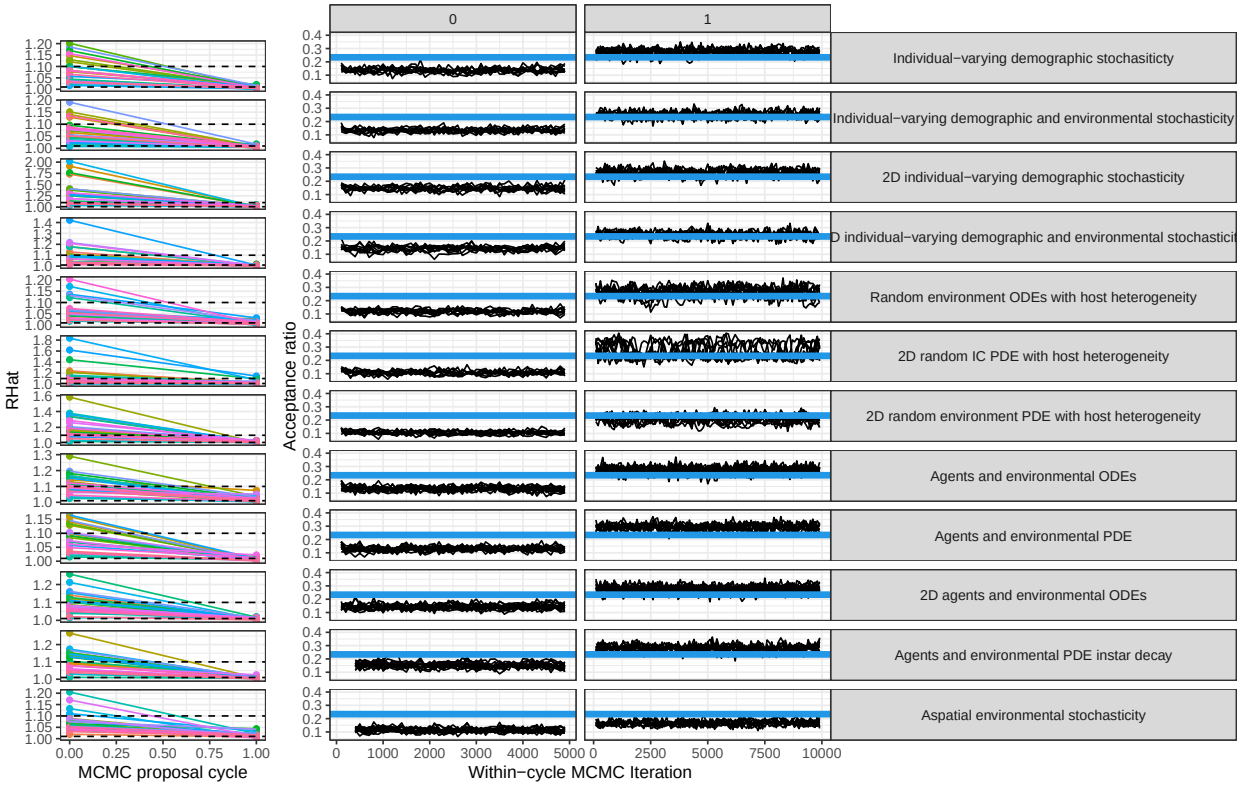

Figure B.5: In the left panels, all $\hat{R}$ values over MCMC proposal cycle iterations, which decline to acceptable range below 1.1. Right panels show acceptance ratios of proposals across MCMC iterations. Each row shows one model construction

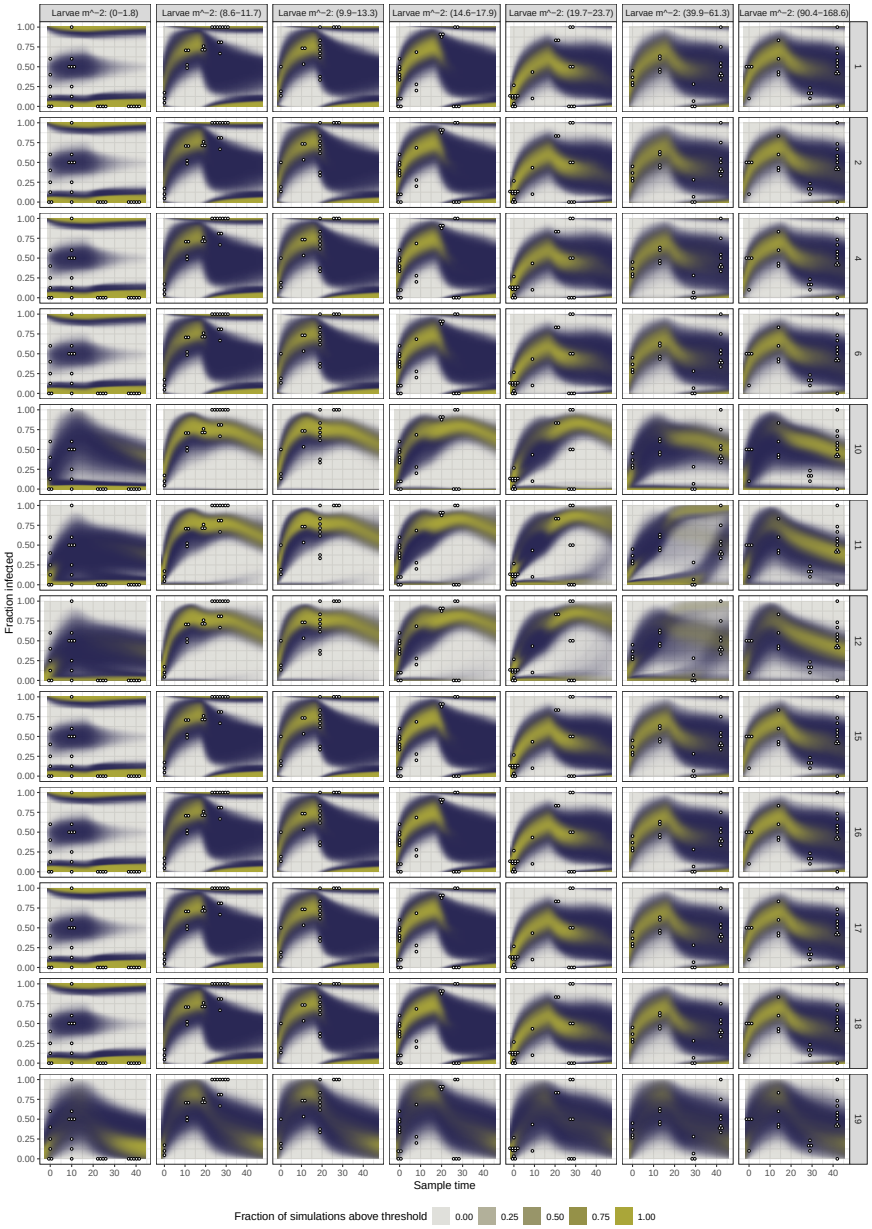

Figure B.6: Comparison of the posterior estimate of incidence load over space and time from all model structures. Over all independent MCMC draws used to calculate ELPD, we observed the proportion of those simulations where the kernel density estimates of fraction infected at time t were above a threshold value of 0.4 or 2. Opaque areas towards purple indicate increased probability of density estimates above 0.4 for a particular fraction infected value at a particular time. Yellow does this for the 2 threshold. We show observed data as dotplots centered at time of collection. Each column is a particular study site and, as columns increase from left to right, estimated host density measured as larvae per square meter increases. Rows show individual model constructions.

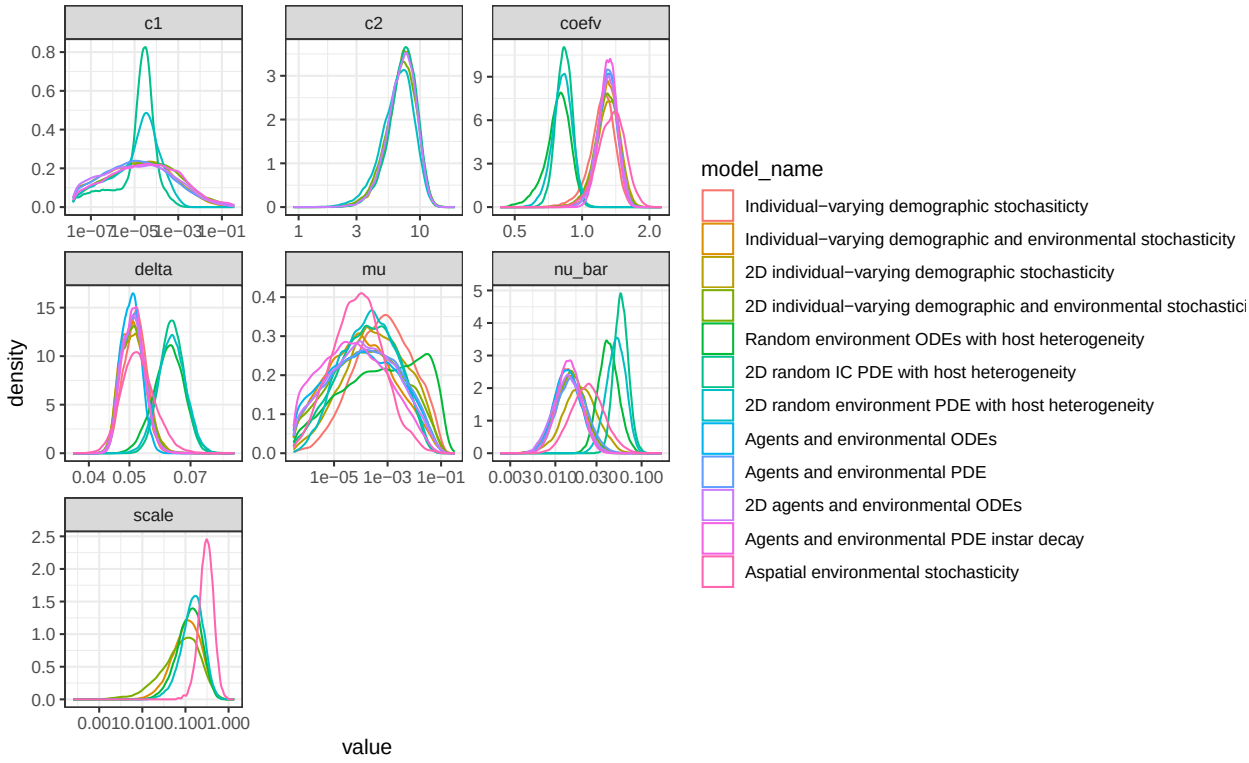

Figure B.7: Posterior distributions for final MCMC iteration across transmission parameters. The differential equations models, in greens and blues, show marked differences from the agent-based models. The non-spatial model, in pink, is most differentiated from the other models.

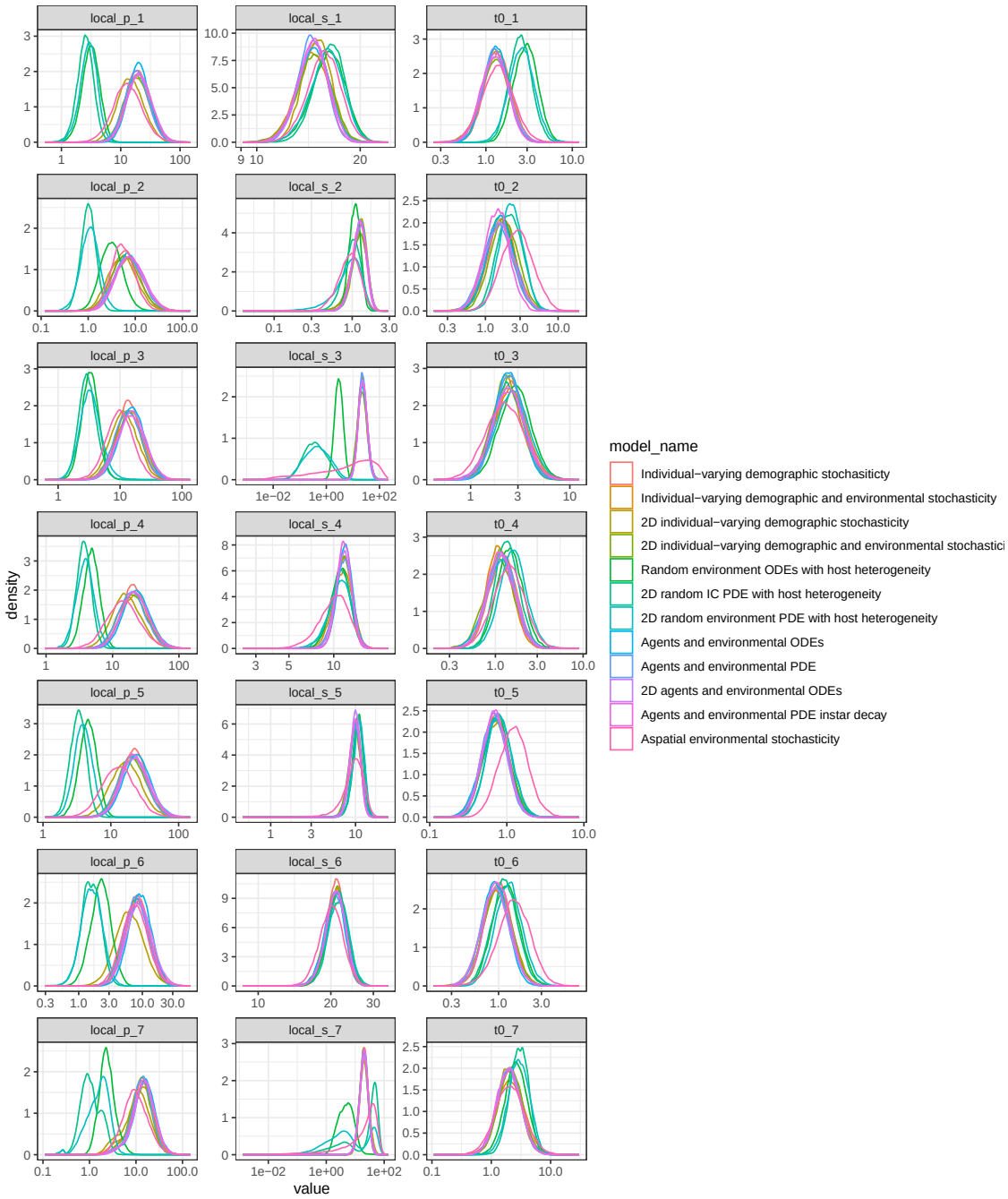

Figure B.8: Posterior distributions for final MCMC iteration across population specific parameters. Host densities, pathogen densities, and the time of first sample collection t_0 were estimated independently for each site. We assumed uninformative priors for pathogen densities. We assumed log normal priors for time of first samples with an expectation of one. We assumed normal priors based on our observed larval branch densities for each site.

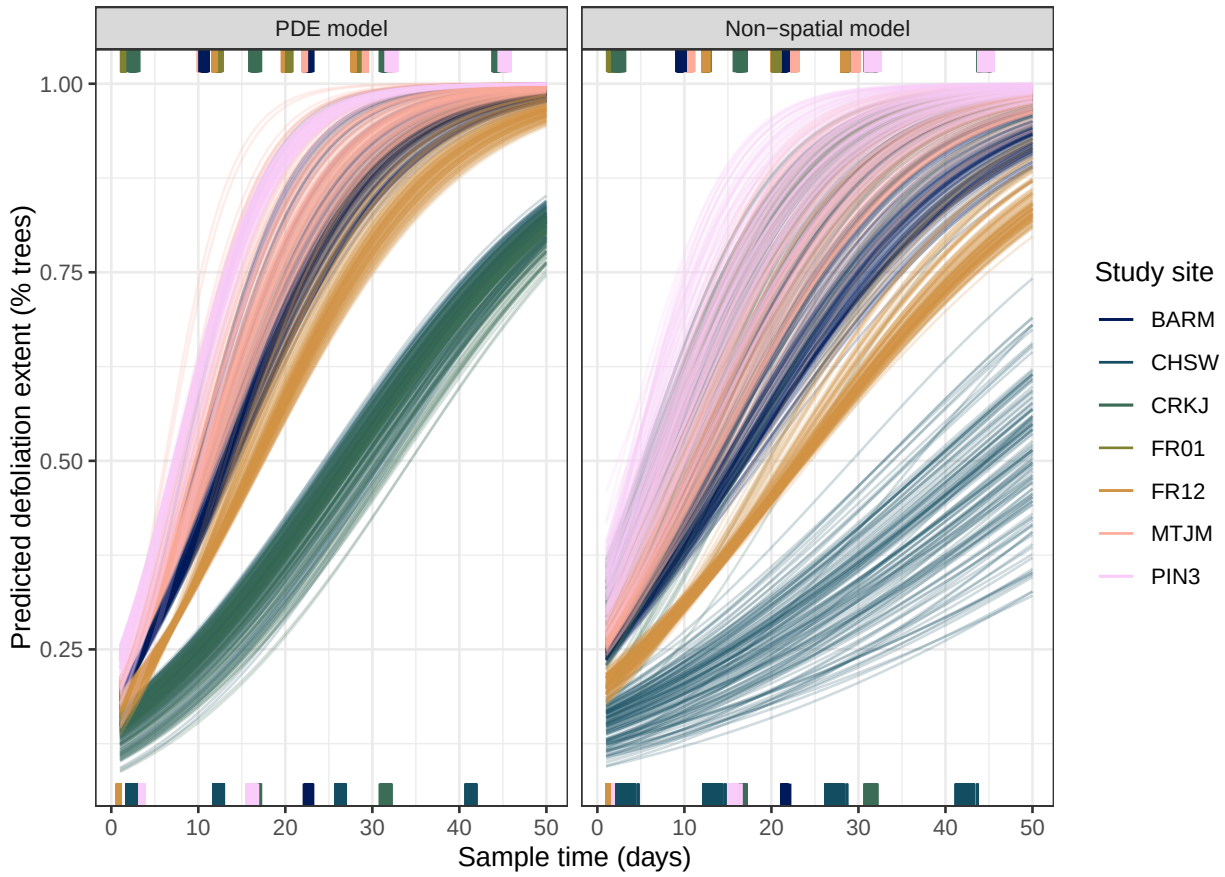

Figure B.9: Regression models of defoliation extent where each line shows one of 124 draws from the posterior $H(\hat{\tau})$. Rugplots show the distribution of data for each of the predictor draws, with either no defoliation present or some defoliation present for each of the study populations (shown as colors). The non-spatial model projections (right) show decreased estimated defoliation extent overall and a wider variation for each study population, but in general are comparable models of defoliation under BIC comparison.

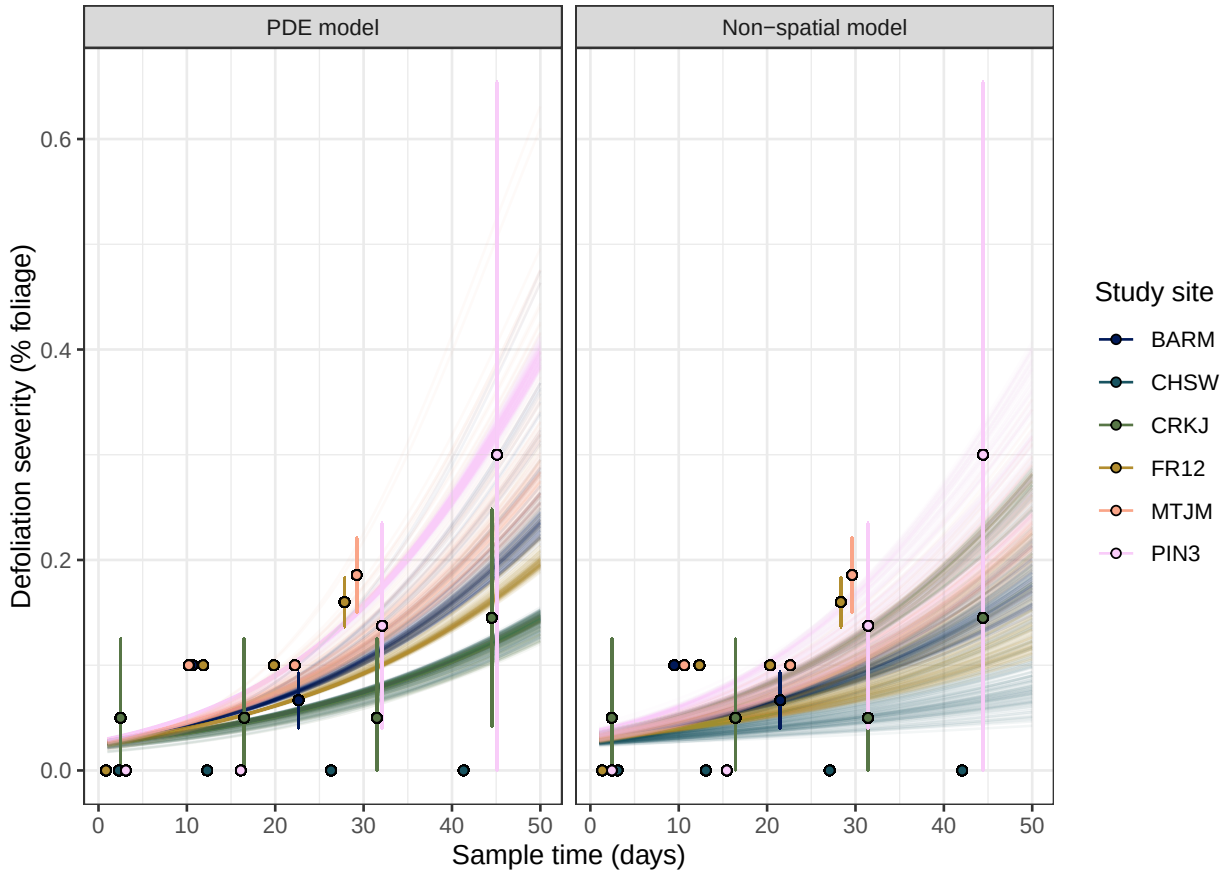

Figure B.10: Regression models of defoliation severity where each line shows one of 124 draws from the posterior $H(\hat{\tau})$. Observed defoliation data aggregated for each study population and time point with error bars showing two standard errors from the mean defoliation severity level

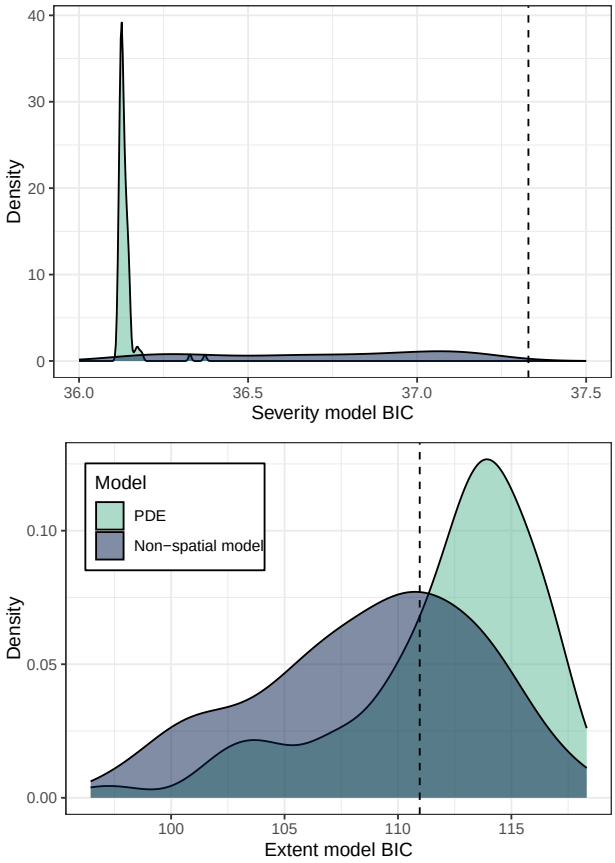

Figure B.11: Distributions for BIC scores across 124 samples for defoliation severity (top) and extent (bottom), with different models shown in either teal (PDE) or dark blue (non-spatial ODE model). The vertical lines in each of the panels show the BIC score for the cumulative insect sample count model. Severity BIC scores show that the PDE offers definitively improved predictive power over the non-spatial and insect density alone models alike. Extent BIC scores show little difference amongst models, with the non-spatial model suggesting an uncertain predictive gain over the PDE model projections.

B.3 Model selection

For our model selection analysis we used the Pareto-smoothed importance sampling leave-one-out cross validation (PSIS-LOO) method. Briefly, we calculated pointwise likelihood scores across all of our models, taking 1,220 independent samples from each posterior distributions of MCMC output and simulating 64 realizations for each sample. We then used the `loo` package in `R` to estimate the contribution of each data point to the expected log pointwise predictive density (ELPD) using Pareto-smoothed importance sampling.

We arrived at the number of samples to take from our MCMC outputs as follows. First, we calculated the integrated auto-correlation time for each MCMC chain using the `LaplacesDemon` package in `R`, which estimates the average number of MCMC iterations before an independent sample is reached. We thinned our MCMC posterior by taking the maximum IAT across all models' MCMC chains as a burn-in value b, throwing out the first b MCMC iterations to exclude samples correlated with the initial MCMC starting positon. We then selected a random $\lfloor \frac{nc}{b} \rfloor$ samples from the posterior of each model, where n is the total number of samples per chain and c is the number of chains. Because we had 10 chains of 10,000 samples each and an IAT of $b \approx 82$, this amounted to $10^5 \times \max(\text{IAT})^{-1} = 1,220$ samples from each model construction to form our log likelihood arrays.

B.3.1 PSIS-LOO, stacking weights, and WAIC comparisons

Pareto smoothed importance sampling leave-one-out cross-validation (PSIS-LOO) is a method used for model selection and evaluation in Bayesian statistics. The PSIS-LOO routine is described in detail by the vignettes written by the `RStan` team and was originally introduced in Vehtari et al. [2017, 2024b]. The routine follows the philosophical approach of WAIC to reward high likelihood scores and penalize likelihood variance, but also offers diagnostics on confidence in the pointwise selection criterion and thus on confidence in the extrapolation of present data to future data.

LOO-CV systematically and singly leaves out each data point, which in our case represents an infection rate of a single tree at a particular time point, and evaluates the model ability to predict the left-out data point based on the remaining data. This process is repeated for all data points, and the resulting predictions are compared to the actual observed values to assess the model's predictive accuracy for future data. The key aspect of PSIS-LOO cross-validation is the use of Pareto smoothed importance sampling (PSIS) to estimate the leave-one-out predictive densities $p(y_i|y_{-i})$, where y_i is the left-out data point and y_{-i} represents all other data points. PSIS-LOO CV is useful when the posterior distribution is highly complex or high-dimensional, as is the case in our MCMC posteriors, because it does not require the exact calculation of leave-one-out predictive density $p(y_i|y_{-i})$. Instead PSIS-LOO estimates this density by drawing importance samples from the full posterior distribution and weighing the importance ratios as the ratio of the leave-one-out posterior density to the full posterior density for each sample. Pareto smoothing stabilizes the estimates of pointwise contributions to the expected log predictive density.

PSIS-LOO therefore provides an efficient estimation of pointwise contribution to the ELPD and evaluation of the performance of each model without having to fit the model repeatedly to the leave-one-out datasets. Instead we were able to leverage the randomly selected, independent 1,220 posterior samples from each of our fitted posteriors.

A key diagnostic of Pareto-smoothed importance sampling is pointwise estimation of our confidence in the selection analysis. Pareto k parameters determine the shape of the likelihood distribution from the posterior parameter sample for a given data point. The distribution of PSIS-LOO Pareto k values are shown in figure B.12. Poor values of $k > 0.5$ indicated that the variance of the smoothed pointwise likelihood score distribution is undefined. Bad values of $k > 0.7$ would have indicated that the mean likelihood score was undefined, and thus that we would not have confidence in the overall model selection scores, but we observed no bad k values. We therefore have confidence in our LOO-CV

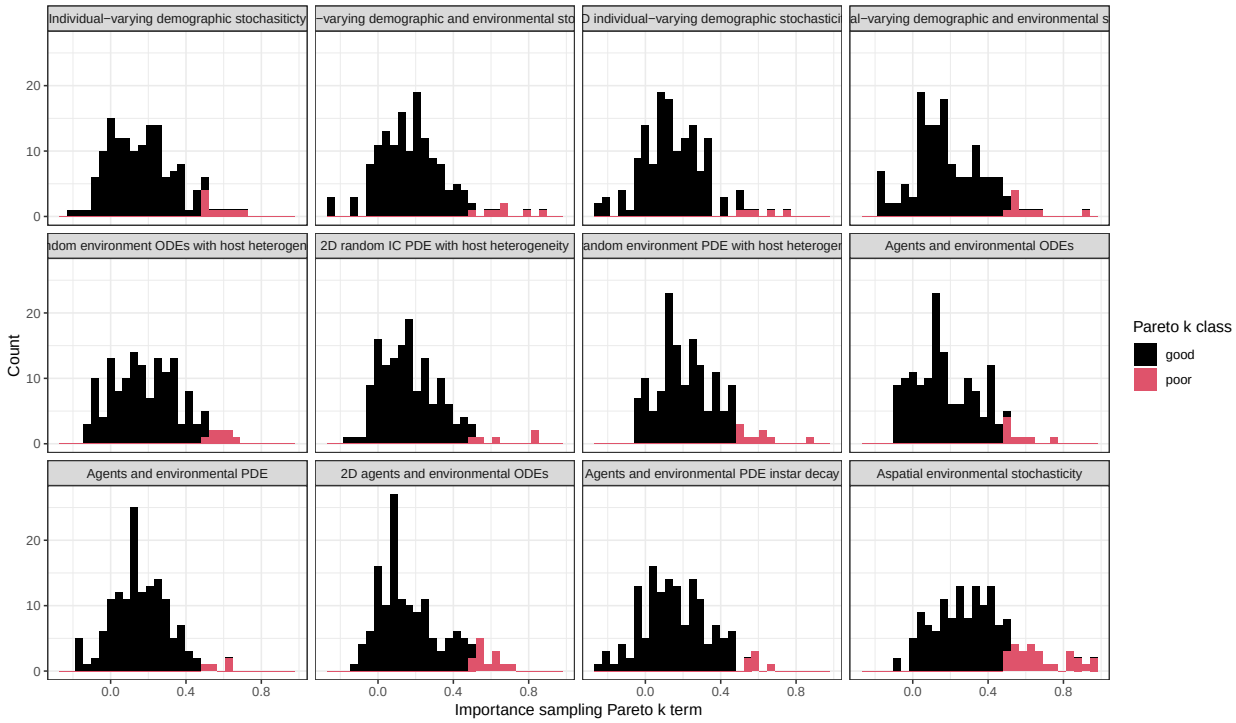

Figure B.12: Distribution of Pareto k values for PSIS-LOO. No values were bad (> 0.7, undefined mean) but some were poor (> 0.5, undefined variance), marked in red. Each panel shows our 144 data points under each model construction.

results. For models that were not able to capture the data well, these poor values were more common. Poor k values indicate that the marginal posterior and LOO posterior are distinct and that some influential observations affect the likelihood score variability. In linear regression models, one way to overcome the difference between the posterior and LOO distributions is to account for overdispersion, for example recommending the replacement of Poisson distributed sample error functions with Negative binomial distributions. However, in our mechanistic model, we instead take these poor k values that show robust likelihood point estimates to further demonstrate poor model fit. The variance in likelihood score distribution for our worst models is reflected in the inflated estimates of effective number of parameters p_{LOO}, which fall out from the calculation of Pareto-k statistics (table B.2).

Our model selection order was robust to using WAIC as a selection criterion (table B.2). To provide more information on the utility of model constructions determined to have a

worse predictive performance than our best spatial model, we calculated Bayesian stacking weights and Pseudo-Bayesian model averaging weights with bootstrapping (Pseudo-BMA+) for each model, again using the `loo` package Yao et al. [2018]. These two approaches are used to determine the best proportions to combine model constructions in a composite model, quantitatively describing the proportion of the predictive density that is best-explained by a particular model. Bayesian stacking of predictive distributions is the best model average and Pseudo-BMA+ provides an approximate alternative (Yates et al. [2023]). Here we compare both as the number of data points do not create computational challenges that would exclude the option of Bayesian stacking. We can see that Pseudo-BMA+ provides an over-estimation of the proportion of the predictive density better explained by our best model ($\sim 67\%$ rather than $\sim 45\%$ under Bayesian stacking). We also note that Pseudo-BMA+ estimates very little of the predictive density to be better explained by any models other than our best and second best spatial models, meaning that the results of table 1 in the main text are conservative.

Bayesian stacking performs well regardless of model similarity. We had several similar models because of our paired model designs, which can be seen in the qualitatively similar dynamics projected by sets of models (figure B.6). This means that we are better able to confirm the utility of some spatial models using Bayesian stacking, such as our hybrid models that use agents for hosts and differential equations for pathogens. Extrapolating from this point, we note that if our best spatial model was more uniquely able to describe the predictive density of our data, we would not have seen such a large drop in the proportion explained between these two composite model approaches. It would then not be unreasonable to claim that our second-best model, which we already acknowledge to not be distinguishable from our best-model, is a reasonable alternative. However, we emphasize that several study sites had low numbers of low-intensity sub-epizootics, meaning that models without diffusion between grid points could offer more reasonable projections because nearly the whole population acted as a transmission “hotspot". If, instead, we had observed more sites with low pathogen

densities, such as our second-highest and third-highest host density sites, we would have likely been able to more clearly distinguish between these two models and the model weight would have been more stable across Bayesian stacking and Pseudo-BMA+ approaches. We can therefore be confident in our main text assessment of the ineffective nature of the second-best model to explain future data reliably.

B.3.2 ELPD performance across subset data

The advantage of PSIS-LOO is not only in the diagnostic capabilities, but in the ability to quickly subset the predictive density by particular attributes such that any time point, site, or, in the extreme, every data point can be used to select a best model. We subset at the site level to determine if there were correlations between larval densities or geographic properties and model performance.

Across all points, higher insect densities lowered overall pointwise predictive densities due to the higher discerning power of larger sample sizes (figure B.13). We note that these sites with more discerning densities were able to be explained by some agent-based models in a comparable fashion to our best spatial model, such that there was an increase in agent-base model performance with site-level average initial insect density (figure B.14).

Agent-based models tended to not provide high predictive performance at the beginning of epizootics and mostly performed well for elevated infection rate data points during the middle of epizootics. We address this in the main text, where we illustrate the difficulty of estimating the highly variable initial epizootic data points when pathogen and exposed host populations are lower. Some data points at the end of the epizootic were able to match the exact distribution of infection rates due to similar denominators (e.g. all samples were of ≤ 2 insects, so fractions infected could only be 0, 0.5, or 1). This occurred despite the high variability of these time points due to low host population sizes after epizootic population collapse and pupation escape, but tended to occur only in our higher density study sites,

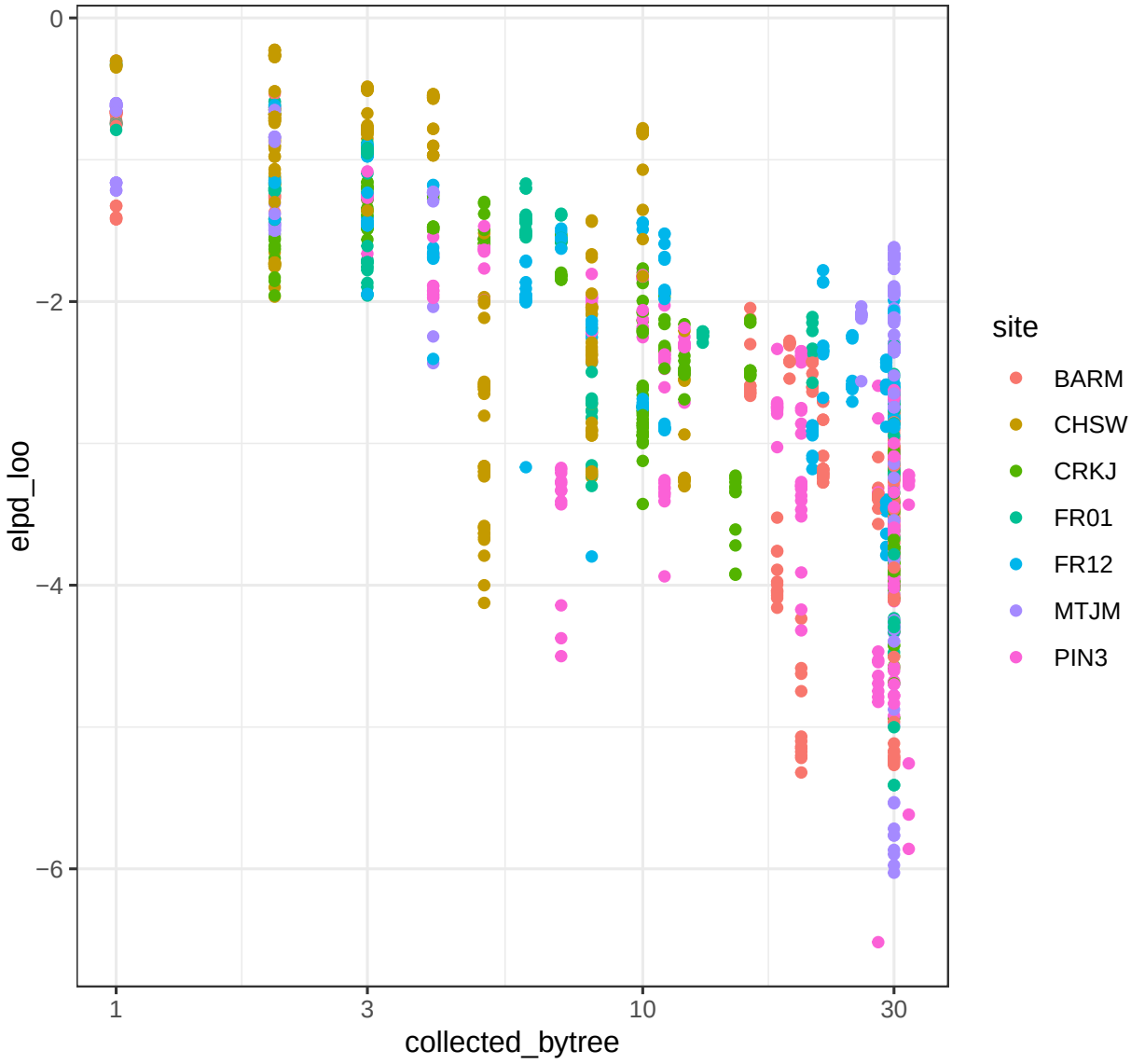

Figure B.13: We see a general decrease in ELPD with increasing insect branch density, generated by more information available from larger sample sizes.

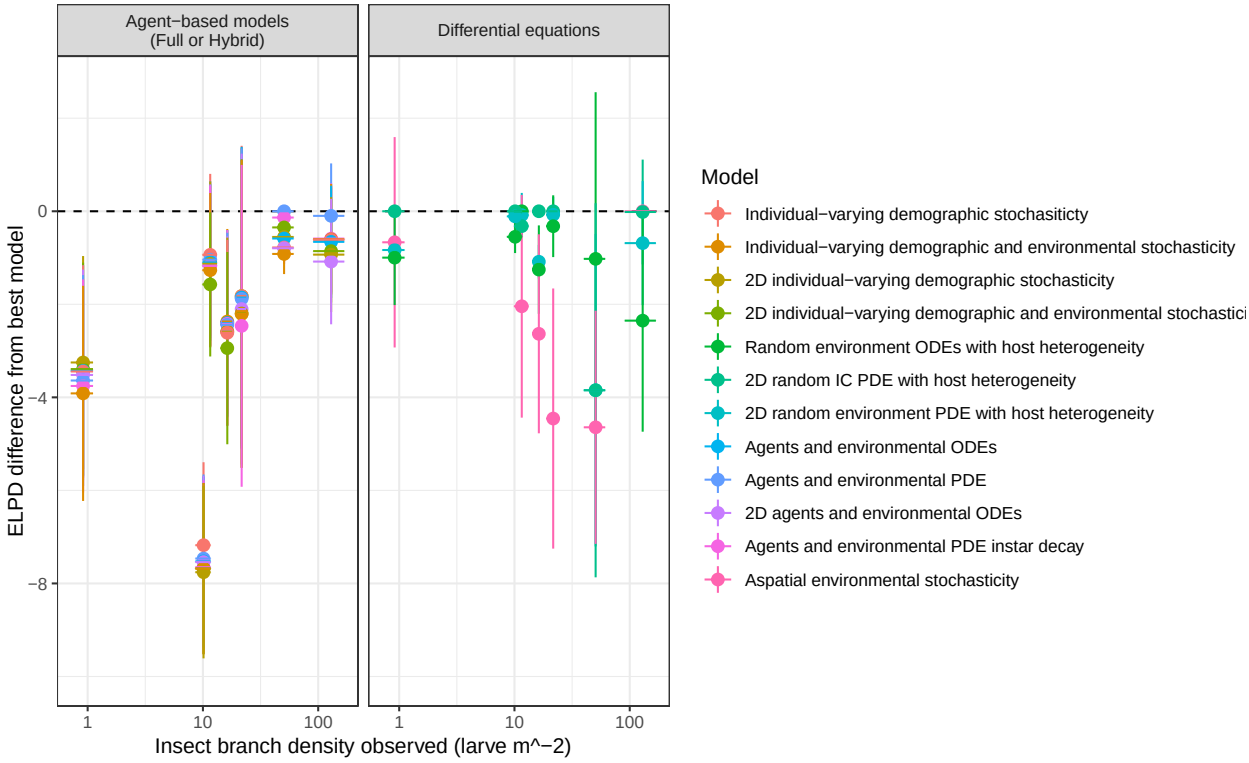

Figure B.14: Plots showing differences from the best model for each study population after subsetting ELPD at the study population level. Horizontal line at zero indicate the best model with worse models and their standard errors shown as point ranges overlapping performance. Although each panel shows agent-based models (left) or differential equations models (right), all model comparisons are done across all 12 models for each study population. Insect density observed at the first time of collection increases from left to right. Improved performance of agent-based models over insect density indicates that agent-based models have better explanatory power at higher host densities. No such consistent relationship exists for differential equations models.

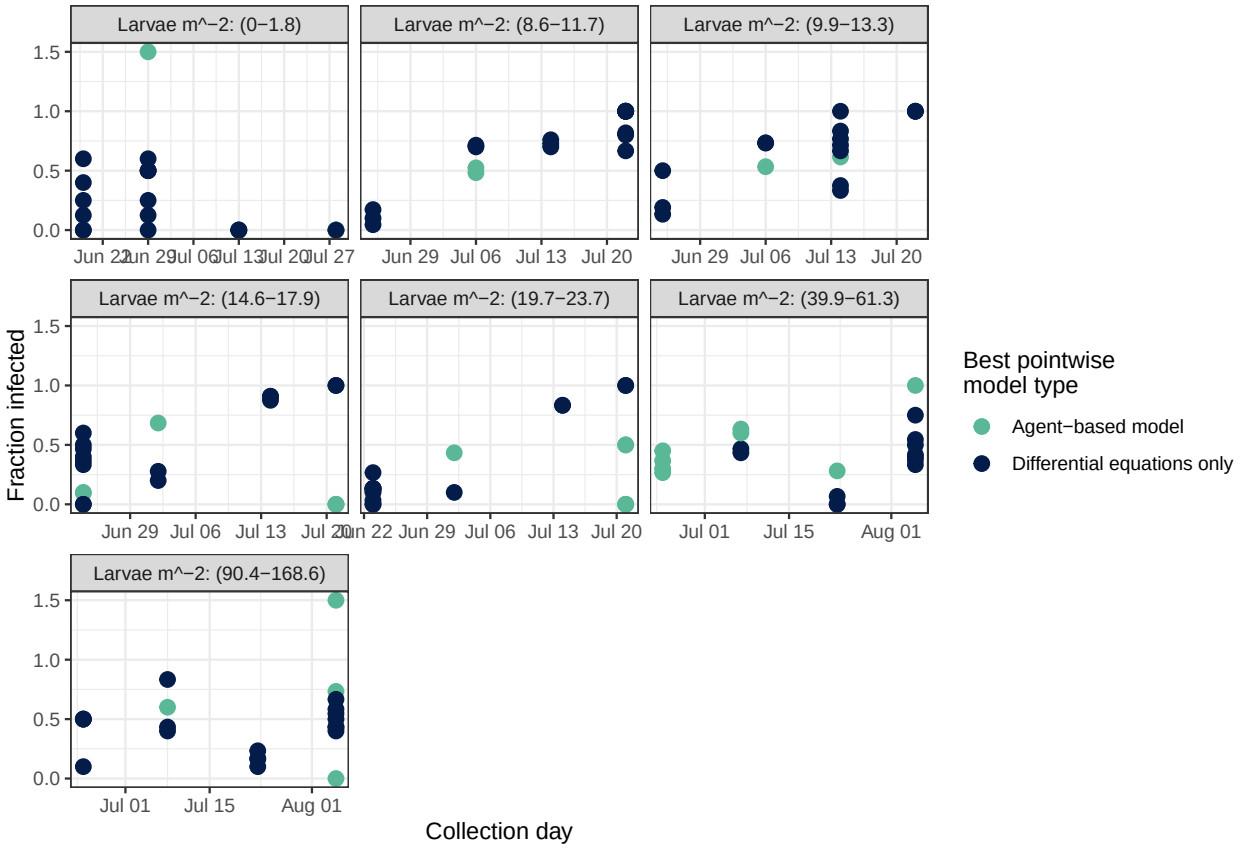

Figure B.15: For each data point we show whether it is better explained by an agent-based (teal) or differential equations model (dark blue).

again supporting our claims in the main text.

Rank	Model description	$\Delta\widehat{\text{ELPD}}_{\text{LOO}} \pm \text{SE}$	$\Delta\widehat{\text{ELPD}}_{\text{WAIC}} \pm \text{SE}$	$\text{p}_{\text{LOO}} \pm \text{SE}$	Stacking weight	Pseudo-BMA+
1	Deterministic PDE	0.00 ± 0.00	0.00 ± 0.00	20.40 ± 3.00	0.454	0.639
2	Independent ODE systems with environmental stochasticity	-2.31 ± 3.26	-1.73 ± 3.20	19.67 ± 2.35	0.223	0.249
3	PDE with environmental stochasticity	-2.53 ± 1.62	-2.31 ± 1.67	24.66 ± 3.24	0.000	0.07
4	Hybrid agent-based host with pathogen PDE	-12.38 ± 6.78	-12.10 ± 6.74	19.22 ± 2.38	0.206	0.013
5	Fully agent-based without movement	-13.20 ± 6.81	-12.82 ± 6.77	20.16 ± 2.55	0.000	0.006
6	Hybrid agent-based host with independent pathogen ODEs	-13.37 ± 6.94	-13.00 ± 6.89	20.52 ± 2.61	0.117	0.006
7	Fully agent-based with host dispersal	-13.85 ± 6.71	-13.43 ± 6.70	20.79 ± 2.51	0.000	0.002
8	Hybrid agent-based host with waning cadaver diffusion PDE	-14.00 ± 6.98	-13.69 ± 6.93	20.26 ± 2.64	0.000	0.004
9	Hybrid agent-based host with independent pathogen ODEs and host dispersal	-14.61 ± 6.98	-14.10 ± 6.91	21.48 ± 2.80	0.000	0.002
10	Fully agent-based with environmental stochasticity	-14.78 ± 6.86	-14.22 ± 6.81	21.83 ± 2.70	0.000	0.001
11	Fully agent-based with host dispersal and environmental stochasticity	-14.80 ± 6.83	-14.27 ± 6.78	21.75 ± 2.72	0.000	0.001
12	Non-spatial ODE with environmental stochasticity	-24.21 ± 8.21	-23.28 ± 8.16	25.76 ± 2.98	0.000	0.000

Table B.2: LOO-CV table from the main text with WAIC, effective parameter count p_{LOO}, and Pseudo-BMA+ weights included. WAIC model order and scores recapture results from LOO-CV.

APPENDIX C

EVOLVING INFECTION RISK DISTRIBUTIONS OVER CONTINUOUS SPACE AND DISCRETE GENERATIONS

C.1 Non-spatial evolving infection risk

Following the continuous time moment closure approximation of Appendix A, we assessed the changes that occur in the density of susceptible hosts $S_n(\nu)$ in generation n that have individual transmission risks between ν and $\nu + d\nu$. The distribution in generation n is determined before the epizootic progresses. For discrete generations, we define the integral of density $S_n(\nu)$ as the total population size N_n, calculating the average infection risk at the beginning of the epizootic in generation n, where

$$s_{n,j} \equiv \int \nu^j S_n(\nu) d\nu \tag{C.1}$$

$$m_{n,j} \equiv \frac{s_{n,j}}{s_{n,0}} \tag{C.2}$$

$$N_n \equiv s_{n,0} = \int S_n(\nu) d\nu \tag{C.3}$$

$$\bar{\nu}_n \equiv m_{n,1} \tag{C.4}$$

$$= \frac{1}{N_n} \int \nu S_n(\nu) d\nu \tag{C.5}$$

$$\tag{C.6}$$

Following Section A.1 and Dwyer et al. [2000], we therefore have the half-generation population size

$$N_{n+\frac{1}{2}} = N_n \left[1 - i_n(N_n, Z_n, \bar{\nu}_n)\right] \tag{C.7}$$

$$\bar{\nu}_{n+\frac{1}{2}} = \bar{\nu}_n \left[1 - i_n(N_n, Z_n, \bar{\nu}_n)\right]^V , \tag{C.8}$$

in which the squared coefficient of variation $V \equiv C^2$ is a constant shape parameter for the density distribution $S_n(\nu)$.

The total population density N_{n+1} in the subsequent generation after reproduction is determined by a intrinsic reproduction parameter r that is modified through a balancing selection trade off modulated through cost parameter ω. Under a fitness trade off, individuals with higher infection risk would have higher net fecundity $\lambda = r(1+\omega\nu)$ (Elderd et al. [2008], Páez et al. [2017], Dwyer et al. [2022]). This is reasonable given some empirical evidence that fecundity is reduced after epizootics in tussock moths (Mason et al. [1977], Dahlsten et al. [1977]) and in other Lepidoptera (Elderd et al. [2008], Páez et al. [2017]). The total population size would thus be

$$N_{n+1} = r \int (1 + \omega\nu) S_{n+\frac{1}{2}}(\nu) d\nu \tag{C.9}$$

$$= r N_n [1 - i_n] \left(1 + \omega \bar{\nu}_n \left[1 - i_n\right]^V\right) \tag{C.10}$$

$$\tag{C.11}$$

To consider the case where infection risk heterogeneity is not strictly due to genetic factors, Páez et al. [2017] introduced the heritability term b. Heritability, the proportion of the total phenotypic variation that is attributable to heritable, genetic factors, then determines how the genetic distribution relates to the overall infection risk distribution Páez et al. [2017]. Combining the approach in equation C.9 with equation C.8 for the average infection over

generations $\bar{\nu}_n$, we arrive at the full non-spatial eco-evolutionary model

$$N_{n+1} = rN_n\left[1-i_n\right]\left(1+\omega\bar{\nu}_n\left[1-i_n\right]^V\right) \tag{C.12}$$

$$Z_{n+1} = \phi N_n i_n + \gamma Z_n \tag{C.13}$$

$$\bar{\nu}_{n+1} = \frac{\bar{\nu}_n\left[1-i_n\right]^{bV}\left[1+\omega(1+bV)\bar{\nu}_n\left[1-i_n\right]^{bV}\right]}{1+\omega\bar{\nu}_n\left[1-i_n\right]^{bV}} \tag{C.14}$$

$$1-i_n = \left[1+\frac{\bar{\nu}V}{\mu}\left(N_n i_n + Z_n\right)\right]^{-\frac{1}{V}}, \tag{C.15}$$

where Z_n is the pathogen population as in Páez et al. [2017]. The pathogen population is determined by the overwintering rate ϕ that translates the infected fourth instar hosts $N_n i_n$ into second instar cadavers Z_{n+1} in the next generation, in addition to the inter-generational pathogen persistence rate γ. The fraction infected i_n must be solved numerically as it is an implicit expression, using any root solver, but it is guaranteed to have at least one positive root between zero and one or be equal to zero (**?**).

C.2 Inter-generational infection risk moment closure over space

In a spatial model with evolving infection risk, the assumption that the squared coefficient of variation V of equations C.12-C.15 is constant is invalid, but the degree to which this invalid assumption causes statistical results to differ from the moment closure approximation is unclear. While the invariant heterogeneity shape assumption is known to be valid during the epizootic at a single spatial location (Dwyer et al. [2000]), the shape of the infection risk distribution could be subject to change during dispersal between points with asynchronous disease dynamics, host densities, and pathogen densities (Shigesada and Kawasaki [1997]). We therefore derived a new moment closure that accounts for higher-order moments than the mean and coefficient of variation.

To arrive at a spatial moment closure that accounts for higher order moments, we closed the moments for each of the two infection risk distributions at location x during the annual Douglas-fir tussock moth life cycle: the infection risk distribution for larvae at the start of the season $S_n(\nu, x)$ and the distribution for adult moths at the end of the season, before reproduction and dispersal $S_{n+\frac{1}{2}}(\nu, x)$ (Leung and Kot [2015]). We strictly consider the heritable infection risk distribution for ease of later notation, but the procedure would be identical apart from placement of heritability parameter b.

The half-generation infection risk distribution $S_{n+\frac{1}{2}}(\nu, x)$ is the adult infection risk distribution that results from the epizootic selection event and is therefore analogous to the non-spatial equation C.8, where

$$\bar{\nu}_{n+\frac{1}{2}}(x) = \frac{1}{N_{n+\frac{1}{2}}(x)} \int \nu S_{n+\frac{1}{2}}(\nu, x) d\nu \tag{C.16}$$

$$= \bar{\nu}_n(x) \left[1 - i_n(x)\right]^{V_n(x)} . \tag{C.17}$$

Crucially, the shape $V_n(x)$ of the infection risk distribution is no longer a constant and must instead be a function of space x and generation n. However, because the squared coefficient of variation $C^2 \equiv V$ still does not change during the epizootic (Appendix A), $V_n(x)$ does not vary at the half generation time and the two values $V_{n+\frac{1}{2}} = V_n$ are equivalent.

In contrast with the adult half generation distribution, the subsequent larval infection risk distribution $S_{n+1}(\nu, x)$ is a mixture distribution comprised of the dispersed progeny from the previous generation n. After calculating the half-generation distribution and population, reproduction and dispersal occur and the mixture distributions over space $S_{n+1}(x)$ get calculated by integrating the product of $S_{n+\frac{1}{2}}(y)$ and the dispersal kernel $k(y, x)$ across all y. We assume that the mixture distributions are only the result of larval dispersal after reproduction in $n + \frac{1}{2}$, and that male flight doesn't change the mean or shape of the infection

risk distribution through gametic mixing with sessile adult females in different populations. This is reasonable considering that male flight is driven by pheromones released by adult female moths (Brookes et al. [1978]), meaning that males will not leave high density populations with available mates and males that enter high density populations from low density populations will likely not significantly change the distributions of their arrival locations.

To arrive at the central moments of the larval infection risk distribution $S_{n+1}(x,\nu)$, we began with the mean infection risk of the larval populations in generation $n+1$.

$$\bar{\nu}_{n+1}(x) = \frac{s_{(n+1),1}(x)}{s_{(n+1),0}(x)} \tag{C.18}$$

$$= \frac{\int k(x,y)N_n(y)(1-i_n(y))\int \nu(1+\omega\nu)S_{n+\frac{1}{2}}(\nu,y)d\nu dy}{\int k(x,y)N_n(y)(1-i_n(y))\int (1+\omega\nu)S_{n+\frac{1}{2}}(\nu,y)d\nu dy}, \tag{C.19}$$

where once again the initial host population densities are determined by overall host reproduction $r(1+\omega\nu)$ and the individuals that survived to reproduce $N_n(x)(1-i_n(x))$. The intrinsic growth rate r cancels from the numerator and denominator, as it is not a function of infection risk ν. We further make substitutions based on the assumption that our non-spatial moment closure holds over the epizootic to place the larval infection risk $S_{n+1}(x,\nu)$ to only depend on $S_n(\nu,x)$ and eliminate the need to explicitly calculate the half-generation time point. We start by noting that

$$\int \nu(1+\omega\nu)S_{n+\frac{1}{2}}(\nu,y)d\nu = \int \nu S_{n+\frac{1}{2}}(\nu,y)d\nu + \omega\int \nu^2 S_{n+\frac{1}{2}}(\nu,y)d\nu \tag{C.20}$$

$$= \mathbb{E}_{n+\frac{1}{2},y}[\nu] + \omega\left[\mathbb{E}_{n+\frac{1}{2},y}[\nu]^2 + \mathrm{Var}_{n+\frac{1}{2},y}(\nu)\right] \tag{C.21}$$

$$= \bar{\nu}_n(y)\left[1-i_n(y)\right]^{V_n(y)} + \omega\left(\bar{\nu}_n(y)\left[1-i_n(y)\right]^{V_n(y)}\right)^2\left[1+V_n(y)\right] \tag{C.22}$$

$$= \bar{\nu}_n(y)\left[1-i_n(y)\right]^{V_n(y)}\left[1+\omega\bar{\nu}_n(y)\left[1-i_n(y)\right]^{V_n(y)}\left(1+V_n(y)\right)\right], \tag{C.23}$$

such that

$$\bar{\nu}_{n+1}(x) = \frac{\int k(x,y)N_n(y)(1-i_n(y)\bar{\nu}_n(y)\left[1-i_n(y)\right]^{V_n(y)}\left[1+\omega\bar{\nu}_n(y)\left[1-i_n(y)\right]^{V_n(y)}\left(1+V_n(y)\right)\right]dy}{\int k(x,y)N_n(y)(1-i_n(y))\left[1+\omega\bar{\nu}_n(y)\left[1-i_n(y)\right]^{V_n(y)}\right]dy} \tag{C.24}$$

is in terms of the first two central moments of larval infection risk distribution, $\bar{\nu}_n(x)$ and $V_n(x)$. This mean infection risk equation differs from simply averaging the mean infection risk over space because the fitness trade off yields higher offspring contribution by populations with higher average infection risk.

Next, we calculated the change in the squared coefficient of variation $V_{n+1}(x)$, which is a function of the already-derived mean infection risk $\bar{\nu}_{n+1}(x)$, as

$$V_{n+1}(x) = \frac{m_2 - m_1^2}{m_1^2} = \frac{m_2}{m_1^2} - 1 \tag{C.25}$$

$$= \frac{\int k(x,y)N_n(y)(1-i_n(y))\int \nu^2(1+\omega\nu)S_{n+\frac{1}{2}}(\nu,y)d\nu dy}{\bar{\nu}_{n+1}^2(x)\int k(x,y)N_n(y)(1-i_n(y))\left[1+\omega\bar{\nu}_n(y)\left[1-i_n(y)\right]^{V_n(y)}\right]dy} - 1 \tag{C.26}$$

If we assume that infection risk heterogeneity can be represented as a gamma distribution, the third central moment, skewness, can be expressed either as a function of only squared coefficient of variation V or as a function of only the mean, variance, and $s_3 \equiv \mathbb{E}[\nu^3]$. Therefore we have a closed, analytical expression for the numerator in $V_{n+1}(x)$, in which the skewness $\tilde{\mu_3}$ can be placed in terms of the lower order moments as

$$\tilde{\mu_3} = 2\sqrt{V} \tag{C.27}$$

$$\tilde{\mu_3} = \frac{s_3 - 3s_1\mathrm{Var}(\nu) - s_1^3}{\mathrm{Var}(\nu)^{3/2}} \tag{C.28}$$

$$2\sqrt{V} = \frac{s_3 - 3\bar{\nu}^3 V - \bar{\nu}^3}{V^{3/2}\bar{\nu}^3} \tag{C.29}$$

$$s_3 = \bar{\nu}^3(2V^2 + 1 + 3V) \tag{C.30}$$

$$\int \nu^3 S_n(\nu)d\nu = \bar{\nu}^3(2V+1)(V+1), \tag{C.31}$$

where equation C.27 arises from assuming a gamma distribution. The third moment expectation of equation C.31 is thus expressed solely in terms of the mean and variation, meaning that

$$\int \nu^2(1+\omega\nu)f_{n+\frac{1}{2}}(\nu, y)d\nu = Var_{n+\frac{1}{2}}(\nu, y) + \bar{\nu}^2_{n+\frac{1}{2}}(y) + \omega\mathbb{E}[\nu^3] \tag{C.32}$$

$$= \bar{\nu}^2_{n+\frac{1}{2}}(y)\left[V_n(y) + 1 + \omega\bar{\nu}_{n+\frac{1}{2}}(y)(2V_n(y)+1)(V_n(y)+1)\right] \tag{C.33}$$

$$= \bar{\nu}^2_{n+\frac{1}{2}}(y)\left[V_n(y)+1\right]\left[1 + \omega\bar{\nu}_{n+\frac{1}{2}}(y)(2V_n(y)+1)\right] \tag{C.34}$$

and that we can reduce this equation to be explictly in terms of the larval distribution like in the mean infection risk calculation of equation C.23. We show the expression for $\bar{\nu}_{n+\frac{1}{2}}$

from equation C.17 again for convenience, so that we have

$$V_{n+1}(x) = \frac{\int k(x,y) N_n(y)(1-i_n(y))\bar{\nu}^2_{n+\frac{1}{2}}(y)\left[1+V_n(y)\right]\left[1+\omega(2V_n(y)+1)\bar{\nu}_{n+\frac{1}{2}}(y)\right]dy}{\bar{\nu}^2_{n+1}(x)\int k(x,y)N_n(y)(1-i_n(y))\left[1+\omega\bar{\nu}_{n+\frac{1}{2}}(y)\right]dy} - 1 \tag{C.35}$$

$$\bar{\nu}_{n+\frac{1}{2}}(x) = \bar{\nu}_n(x)\left[1-i_n(x)\right]^{V_n(x)}. \tag{C.36}$$

It should be noted that although we are here making an assumption that the post-epizootic heterogeneity in infection risk follows a gamma distribution, we are not specifically assuming the same for the pre-epizootic mixture distribution. The mixture will likely be easily approximated by a gamma, but it would be a rare occurrence that the mixture distribution would exactly follow a gamma distribution because all neighboring sites would have to have the same estimated scale parameter. The only assumptions we make then are that the coefficient of variation doesn't change over the course of the epizootic, the average infection risk $\bar{\nu}_{n+\frac{1}{2}}$ at the end of the epizootic season is of the form shown in the half generation equation C.17, and that ultimately the surviving adult population infection risk distribution does follow a gamma distribution. Our analytical equations take a different in form if we assume another strictly positive distribution for infection risk but would be analogous so long as higher order moments close. For example, using a log-normal distribution did not affect the approach or consistency of numerical and analytical results, but we use a gamma distribution based on prior studies and the reduced tailedness of the distribution that allows the within-season epizootic moment closure for $\bar{\nu}_{n+\frac{1}{2}}$ to better approximate the exact distribution.

Finally, because the moments of $S_n(x)$ are over heritable infection risk variation passed on to progeny by the half-generation adult populations, heritability b now appears in the expression for changing host densities instead of the average infection risk as in equations

C.12-C.15. Again, for notational convenience, we keep $\bar{\nu}_{n+\frac{1}{2}}$ even though it is not necessary to calculate explicitly prior to calculating $\bar{\nu}_{n+1}$. Our final system of equations is thus

$$N_{n+1}(x) = \int rk(x,y)N_n(y)\left[1-i_n(y)\right]\left(1+\omega\bar{\nu}_n(y)\left[1-i_n(y)\right]^{\frac{V_n(y)}{b}}\right)dy \tag{C.37}$$

$$Z_{n+1}(x) = \int \phi k(x,y)N_n(y)i_n(y)dy + \gamma Z_n(x) \tag{C.38}$$

$$\bar{\nu}_{n+1}(x) = \frac{\int k(x,y)N_n(y)(1-i_n(y))\bar{\nu}_{n+\frac{1}{2}}(y)\left[1+\omega(1+V_n(y))\bar{\nu}_{n+\frac{1}{2}}(y)\right]dy}{\int k(x,y)N_n(y)(1-i_n(y))\left[1+\omega\bar{\nu}_{n+\frac{1}{2}}(y)\right]dy} \tag{C.39}$$

$$V_{n+1}(x) = \frac{\int k(x,y)N_n(y)(1-i_n(y))\bar{\nu}^2_{n+\frac{1}{2}}(y)\left[1+V_n(y)\right]\left[1+\omega(1+2V_n(y))\bar{\nu}_{n+\frac{1}{2}}(y)\right]dy}{\bar{\nu}^2_{n+1}(x)\times\int k(x,y)N_n(y)(1-i_n(y))\left[1+\omega\bar{\nu}_{n+\frac{1}{2}}(y)\right]dy} - 1 \tag{C.40}$$

$$i_n(x) = 1-\left(1+\frac{\bar{\nu}_n(x)V_n(x)}{b\mu}\left(N_n(x)i_n(x)+Z_n(x)\right)\right)^{-\frac{b}{V_n(x)}} \tag{C.41}$$

$$\bar{\nu}_{n+\frac{1}{2}}(x) = \bar{\nu}_n(x)\left[1-i_n(x)\right]^{V_n(x)}, \tag{C.42}$$

C.3 Loss of heterogeneity under Dirac delta dispersal kernel

To compare this spatial eco-evolutionary model to the previous, non-spatial model, we removed dispersal by setting the dispersal kernel $k(x,y)$ to be the Dirac delta function centered at x (Leung and Kot [2015]). Simplifying notation by reducing the state variables to be only a function of time, we arrived at

$$V_{n+1} = \frac{N_n(1-i_n)\bar{\nu}^2_{n+\frac{1}{2}}\left[1+V_n\right]\left[1+\omega(1+2V_n)\bar{\nu}_{n+\frac{1}{2}}\right]}{\bar{\nu}^2_{n+1}\times N_n(1-i_n)\left[1+\omega\bar{\nu}_{n+\frac{1}{2}}\right]} - 1 \tag{C.43}$$

$$= \frac{(N_n(1-i_n))^2\bar{\nu}^2_{n+\frac{1}{2}}\left[1+V_n\right]\left[1+\omega\bar{\nu}_{n+\frac{1}{2}}\right]\left[1+\omega(1+2V_n)\bar{\nu}_{n+\frac{1}{2}}\right]}{\left(N_n(1-i_n)\bar{\nu}_{n+\frac{1}{2}}\left[1+\omega(1+V_n)\bar{\nu}_{n+\frac{1}{2}}\right]\right)^2} - 1 \tag{C.44}$$

$$= \frac{\left[1+V_n\right]\left[1+\omega\bar{\nu}_{n+\frac{1}{2}}\right]\left[1+\omega(1+2V_n)\bar{\nu}_{n+\frac{1}{2}}\right]}{\left(1+\omega(1+V_n)\bar{\nu}_{n+\frac{1}{2}}\right)^2} - 1 \tag{C.45}$$

$$= \left[1+V_n\right]\frac{1+2\omega\bar{\nu}_{n+\frac{1}{2}}(1+V_n)+\omega^2\nu^2_{n+\frac{1}{2}}(1+V_n)^2-\omega^2\nu^2_{n+\frac{1}{2}}V_n^2}{\left(1+\omega(1+V_n)\bar{\nu}_{n+\frac{1}{2}}\right)^2} - 1 \tag{C.46}$$

$$= \left[1+V_n\right]\left[1-\frac{\omega^2\nu^2_{n+\frac{1}{2}}V_n^2}{\left(1+\omega(1+V_n)\bar{\nu}_{n+\frac{1}{2}}\right)^2}\right] - 1 \tag{C.47}$$

$$= V_n - \left[1+V_n\right]\left[\frac{\omega\nu_{n+\frac{1}{2}}V_n}{1+\omega(1+V_n)\bar{\nu}_{n+\frac{1}{2}}}\right]^2 \tag{C.48}$$

$$V_{n+1} = V_n - \left[1+V_n\right]\left[\frac{\omega V_n\bar{\nu}_n\left[1-i_n\right]^{V_n}}{1+\omega(1+V_n)\bar{\nu}_n\left[1-i_n\right]^{V_n}}\right]^2, \tag{C.49}$$

demonstrating that without space, accounting for skewness through changing coefficient of variation in infection risk makes the variation decrease to zero, recapturing a classic result in population genetics.

To assess the circumstances that cause inconsistencies between our novel moment closure with the approximate model with invariant shape V, we conducted a statistical test and then a sensitivity analysis of dynamics in two populations.

To verify that decreasing variation would occur and assess the sensitivity of differences between the two models to cost ω, we conducted a statistical experiment where we drew offspring infection risk values from parental infection risk values. We began with a parental

infection risk distribution using random gamma variables with shape $\frac{1}{V}$ and scale $V\bar{\nu}$. We drew offspring count f_i for each individual i according to a Poisson distribution with mean $1 + \omega\nu_i$. Since these calculations are only for the heritable infection risk heterogeneity, the f_i progeny of individual i in the next generation inherit exactly ν_i. We then calculated the variance and mean of the offspring infection risk distribution.

The statistical experiment results match our analytical results well (Figure C.1), meaning that our new system tracking evolving infection risk is reliable. Because infection risk is more strongly correlated with fecundity as cost parameter ω increases, the offspring distribution becomes more shifted towards higher infection risk and variation V decreases more sharply as cost increases. These results likely have little impact on simulations over few years or for low values of $\omega < 10$ in non-spatial models because the offspring infection risk distributions do not strongly differ from the parental distributions under these circumstances.

Following our statistical simulations, we assessed the cyclical dynamics of non-spatial simulations with evolving infection risk and declining infection risk heterogeneity. In these deterministic simulations over discrete generations, heterogeneity decreased until passing below one, at which point cycling dynamics occurred because values of V less than one generate cycles. The phase diagrams show that many areas of parameter space cause "chaotic extinctions" where populations reach exceedingly low densities and, due to numerical limitations of floating point numbers, go to zero.

C.4 Maintenance of heterogeneity in multiple populations

Non-spatial dynamics therefore suggest that infection risk variation over generations should disappear due to balancing selection. To determine the effects of spatial environments on infection risk heterogeneity, we first assessed the conditions for which discrete populations with some level of imperfect mixing could maintain non-decreasing variation over time V_n in our eco-evolutionary model. We forced environmental heterogeneity by including differences

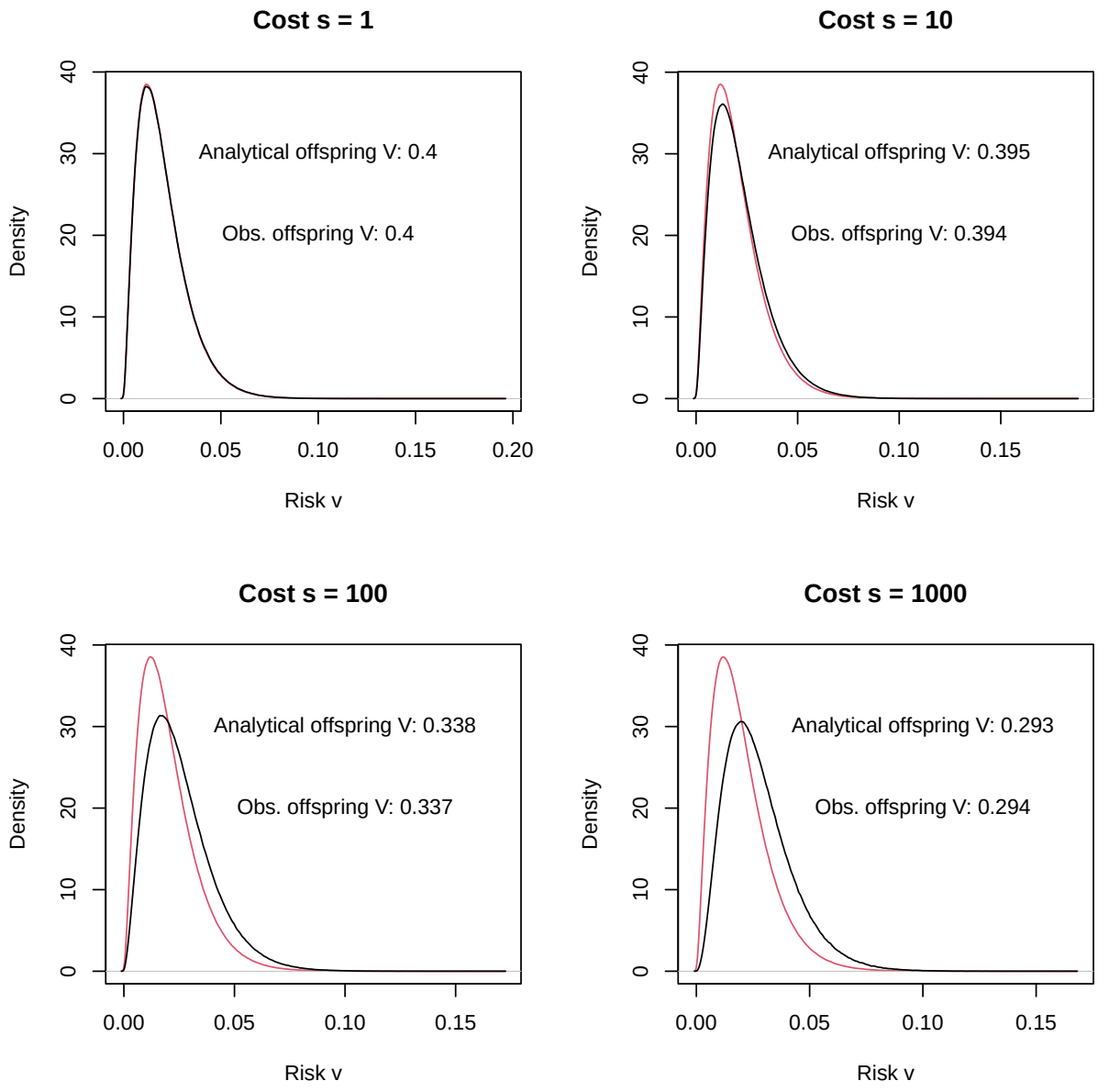

Figure C.1: Offspring distribution of infection risk (black) as a result of the parental distribution (red). Base reproduction is assumed to be 1. Parental mean infection risk $\bar{\nu}_{n+\frac{1}{2}} = 0.02$ and parental squared coefficient of variation V_n is 0.4. The shifting distribution of offspring infection risk is a result of balancing selection from the cost of resistance parameter ω. The distributions change mean during reproduction, but notably also change shape according to analytical equation C.49

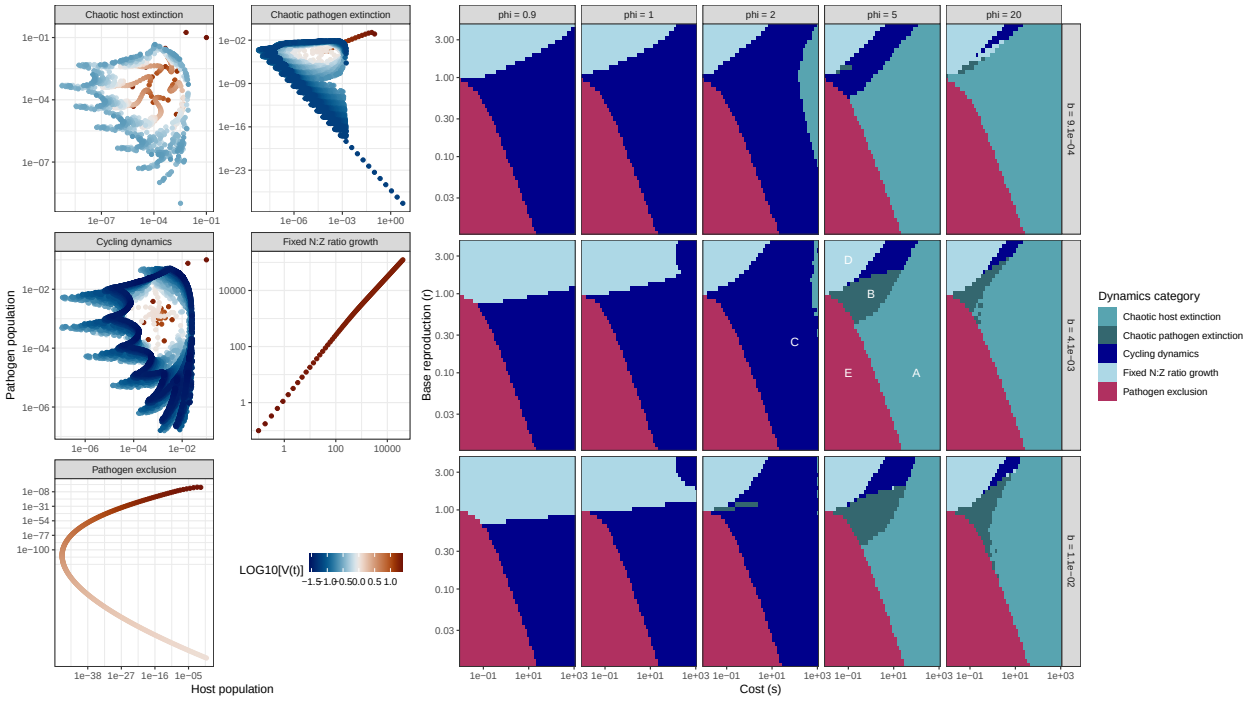

Figure C.2: The dynamics of parameter space for non-spatial eco-evolutionary model with changing heterogeneity shape V_n. Left panels show example phase portraits of pathogen density Z_n and host density N_n, where color represents the log of the squared coefficient of variation. Cycles occur for values of V_n below 1. Right panels map trajectory portraits to areas of parameter space, varying pathogen overwintering ϕ, heritability b, intrinsic reproduction r and cost ω.

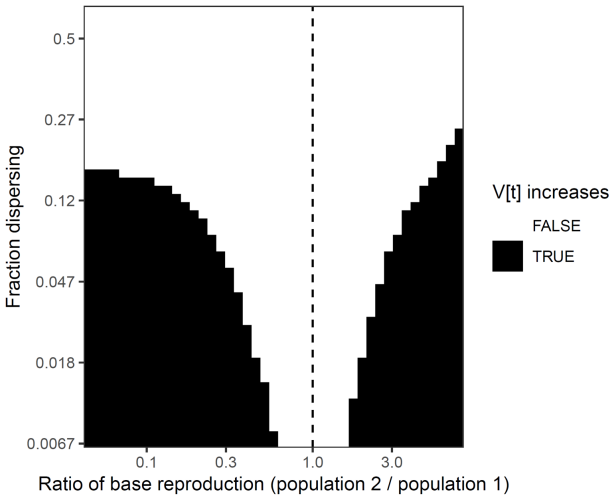

Figure C.3: Black areas show the regions of parameter space where heterogeneity in infection risk is not strictly decreasing for a two population model. Low levels of dispersal and differences in growth rates led to asynchronous population cycles exchanging individuals to drive increases in overall heterogeneity. Upper limit of 50% fraction dispersing show the perfect mixing case for two populations, arriving again at a single population.

in the intrinsic growth rate r of two host populations. We found that allowing for as few as two populations led to scenarios in which infection risk heterogeneity over time was not strictly decreasing. For low rates of dispersal between the two populations and growth rate differences of approximately two orders of magnitude, change in infection risk variation $\Delta V_{n,i}$ over time in population i was positive, indicating that asynchronous populations with different equilibria can easily maintain overall population heterogeneity of infection risk.

In the case of continuous space, we found that growth rate differences do not need to be explicitly invoked in order to maintain infection risk heterogeneity. In continuous spatial models, differences in the time between outbreaks, or cycle period, created variation over space in the wake of invasion that reflected the same level of changes that environmental forcing created in the two population scenario. In figure C.4, we show several simulations that have variable rotation number over space centuries after a point release of host and pathogen densities. In contrast with the environmental forcing scenario, all of the populations distributed over space had the same equilibria, but were at different points in the cycle due

to invasion timing. Different populations over space had different cycle periods due to the interaction of dispersal and asynchronous populations disrupting each other. The non-linear interaction of host, pathogens, average infection risk, and infection risk variation as functions of generational time led to chaos in the wake of invasion that persisted for multiple centuries, similar to some cases of non-evolutionary predator-prey dynamics (Sherratt et al. [1995], Bjørnstad et al. [2002]). Decreasing heritability b led to higher levels of synchronization of rotation numbers over space, but heterogeneity was still maintained after invasion for centuries in the simulation with lower heritability.

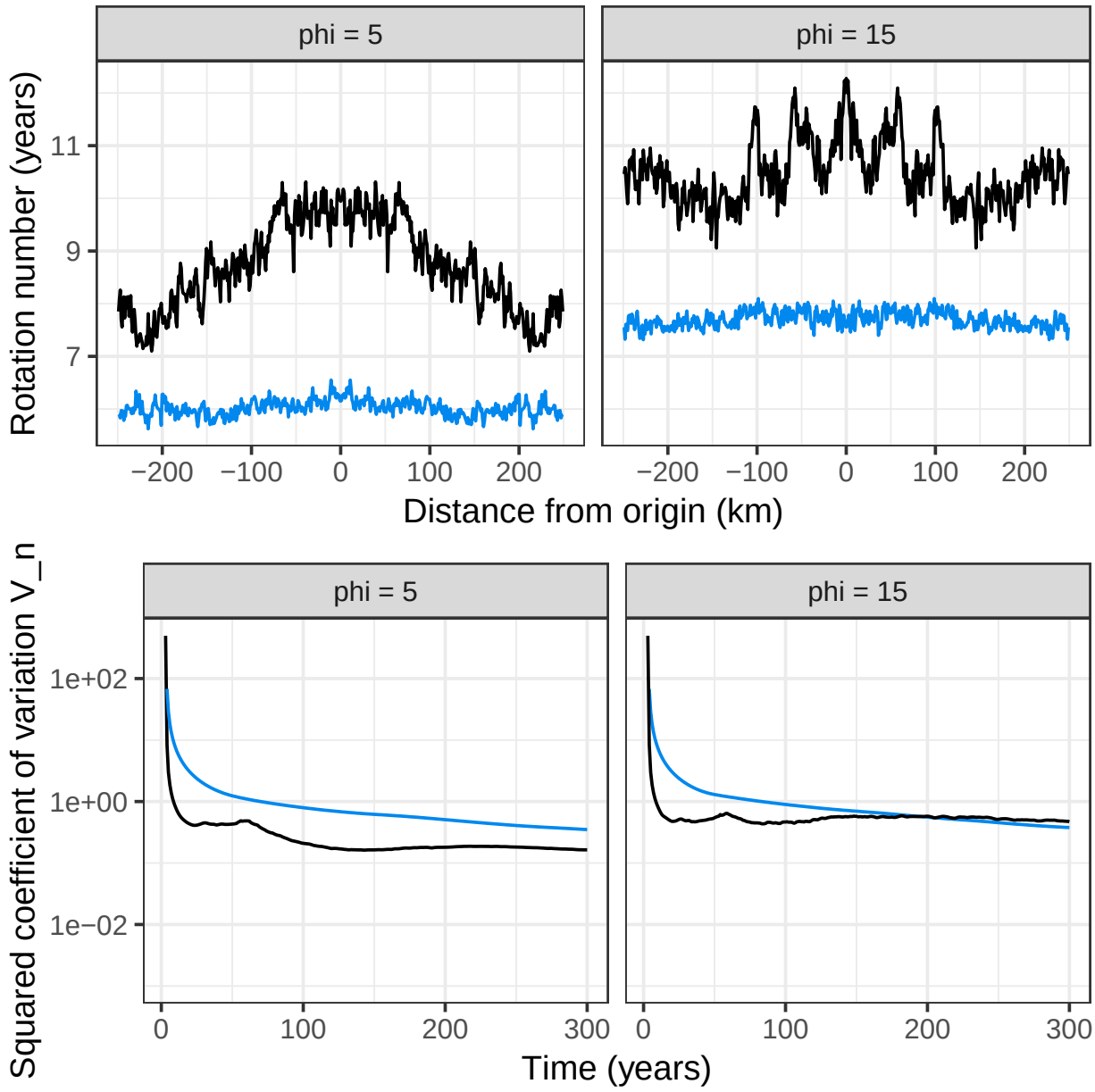

Figure C.4: Four example simulations of the average squared coefficient of variation over space for each generation n in evolutionary model with thin-tailed dispersal. Top panels show the cycle period, or "rotation number", and lower panels show the variation of infection risk at the origin $V_n(0)$. Two values of overwintering $\phi = 5$ (left panels) or 15 (right panels) and two values of heritability $b = 0.02$ (black lines) and 0.002 (blue lines) were used, with pathogen survival $\gamma = 0.1$, pathogen decay $\mu = 1 \times 10^{-4}$, and the best parameters from wave front parameterization (table 3.1).

APPENDIX D

FITTING INTEGRODIFFERENCE MODELS TO INSECT OUTBREAK DATA

D.1 Wave speed approximations for integrodifference models

Integrodifference equations, which model continuous space and discrete time, are key tools for understanding the dynamics of wave fronts Kot et al. [1996], Shigesada and Kawasaki [1997], Sherratt and Smith [2008]. The discrete time steps, often representing generations, accurately reflect the biology of many annually reproducing animals and plants, such as Douglas-fir tussock moth. Over discrete generations n and a continuous spatial domain $(-\infty, +\infty)$, integrodifference equations take the general form

$$N_{n+1}(x) = \int_{-\infty}^{+\infty} f(N_n(y))k(y,x)dy, \tag{D.1}$$

where the population density at point x in generation $n+1$ is determined by some growth function $f(N_n(y))$ of all the population densities across space in the previous generation n multiplied by the probability that individuals from site y arrive at site x according to the dispersal kernel $k(y,x)$. It is common practice to use symmetrical or unidirectional dispersal kernels Sherratt et al. [1995], Kot et al. [1996], Leung and Kot [2015], where dispersal probability is determined by the absolute distance between two spatial locations Δx. Such dispersal kernels represent the long distance dispersal potential of individuals, assuming that populations at particular points in space are perfectly mixing during growth and reproduction.

We required many simulations of our integrodifference model with evolving infection risk over space to determine its ability to explain the speed of re-establishment observed in tussock moth defoliation patterns. As simulating the integrodifference models is computationally

intensive (Appendix E), we instead calculated analytical expressions of the rate of advance (Kot et al. [1996], Neubert et al. [2000], Liu and Kot [2019]). We focused exclusively on host populations invading empty habitat, with the assumption that the pathogen is absent when the host is absent and that the rate of expansion by the pathogen is therefore strictly less than or equal to the host invasion speed alone (Sherratt et al. [1995], Phillips et al. [2010]).

D.1.1 Recursion methods for thin-tailed kernels

The two patterns of invasion that are commonly observed are pushed waves, the constant wave speed invasions that propagate from the pressure of individuals dispersing from the bulk of the established population behind the wavefront, and pulled waves, the accelerating invasions that propagate from the expanding reach of individuals dispersing at the wave front. In pushed wave fronts that have fixed rates of advance, there is some threshold population size that satisfies the equation

$$\bar{N}_{n+1}(\hat{x}_{n+1}) = \bar{N}_n(\hat{x}_n) \tag{D.2}$$

$$\hat{x}_{n+1} = c + \hat{x}_n, \tag{D.3}$$

where c is the constant wave speed and $\hat{x}_n$ is the position of the wave front in generation n (Kot et al. [1996]). Wave speed c can be calculated analytically through a single minimization equation if there exists some moment generating function $g(m)$ of the dispersal kernel

$$c = \min_m \left[\frac{1}{m} \ln(\lambda g(m)) \right] \tag{D.4}$$

where λ is the instantaneous reproduction rate of the population (Kot et al. [1996]). Such dispersal kernels that possess moment generating functions are called “thin-tailed" kernels and are exponentially-bounded (Liu and Kot [2019]).

In pulled waves that accelerate during invasion, however, rather than the wave position difference c approaching a constant speed, the ratio of the wave front positions over time asymptotically approaches a constant in the form

$$\lim_{n\to\infty} \frac{\hat{x}_{n+1}}{\hat{x}_n} = \rho. \tag{D.5}$$

and such accelerating waves of advance can be caused by either “heavy-tailed" kernels, for which a moment generating function does not necessarily exist, or for evolving traits at the wave front (Liu and Kot [2019]). We are interested both in cases with evolving growth rate λ_n and in cases with heavy-tailed dispersal kernels with excess outliers. We therefore required approximations that included either or both of these mechanisms.

In the evolving infection risk model where hosts populations expand over space and the pathogen wave front has not yet caught up to the host front, the reproduction rate at the host front $\lambda_n(\hat{x}_n)$ is strictly increasing as individuals come to have higher infection risk and higher fecundity (Páez et al. [2017], Dwyer et al. [2022]), leading to the acceleration. In such cases where growth rate λ varies over generations, the average speed $\bar{c}$ across generations 0 to τ is determined by the geometric mean of the reproduction rates (Neubert et al. [2000]). We therefore use the minimization

$$\bar{c}_\tau = \min_m \left[\frac{1}{m} \ln \left(\prod_{n=0}^{\tau} \lambda_n g_n(m) \right)^{\frac{1}{\tau}} \right]. \tag{D.6}$$

We calculated the instantaneous speed c_n in generation n by using the value $\bar{m}$ that satisfies minimization equation D.6 as

$$c_n = \frac{1}{\bar{m}} \ln \left[\lambda_n g_n(\bar{m}) \right], \tag{D.7}$$

We then calculated the increasing fecundity and increasing infection risk of the host population at the wave front position $\hat{x}$ following the IDE system from equations 3.4-3.9

with $i_n(\hat{x}_n) = 0$ for $n \in (0, \tau)$. The resulting speed c_{n+1} and growth rates λ at the evolving wave front are

$$\nu_{n+1}(\hat{x}_{n+1}) = \nu_n(\hat{x}_n)\left(\frac{1+\omega\nu_n(\hat{x}_n)\left[V_n(\hat{x}_n)+1\right]}{1+\omega\nu_n(\hat{x}_n)}\right) \tag{D.8}$$

$$V_{n+1}(\hat{x}_{n+1}) = \nu_n(\hat{x}_n)^2\left[V_n(\hat{x}_n)+1\right]\frac{1+\omega\nu_n(\hat{x}_n)\left[1+2V_n(\hat{x}_n)\right]}{\nu_n(\hat{x}_n)^2\left[1+\omega\nu_n(\hat{x}_n)\right]} - 1 \tag{D.9}$$

$$\lambda_{n+1}(\hat{x}_{n+1}) = r\left[1+\omega\nu_n(\hat{x}_n)\right] \tag{D.10}$$

$$\bar{c}_{n+1}(\hat{x}_{n+1}) = \min_m\left[\frac{1}{m}\ln\left(\prod_{i=0}^{n+1}\lambda_i(\hat{x}_i)\times g_i(m)\right)^{\frac{1}{n+1}}\right] \tag{D.11}$$

$$c_{n+1}(\hat{x}_{n+1}) = \frac{1}{\bar{m}}\ln\left[\lambda_{n+1}(\hat{x}_{n+1})\times g_{n+1}, (\bar{m})\right] \tag{D.12}$$

which are unaffected by generalist parasitoids due to the normalizing constants of the full eco-evolutionary model in equations 3.4-3.9. Further, the arbitrary selection of host density threshold means that the exact location $\hat{x}_n$ is unaffected by habitat patchiness. We observed that our wave front analytical expressions were equally suitable for determining the rate of advance in simulations that included habitat patchiness, where the larger reproduction rate $r(x)$ across space determined the overall rate of spread, and in simulations that included generalist parasitoids. In contrast, see Neubert et al. [2000], in which the reproduction rate fluctuates over time in unison across the entire spatial domain, thereby altering invasion speeds.

D.1.2 Tail-additivity approximation for fat-tailed kernels

Fat-tailed kernels comprise a set of heavy-tailed dispersal kernels that exhibit power law decay with order α such that $k(x, y) = k(|x-y|) \equiv k(x) \propto x^{-\alpha}$ (Kot et al. [1996], Shigesada and Kawasaki [1997]). In contrast with thin-tailed kernels, fat-tailed kernels lack moment

generating functions for some or all of parameter space α and the recursion from analytical equations above does not hold. Instead, we used the tail-additivity approximation for fat-tailed kernels, which works well at distances that are far enough from the origin to have low arrival probabilities, which is a convenient property of the wave front position $\hat{x}_n$ (Liu and Kot [2019]). The tail additivity approximation for fat-tailed kernels demonstrates that the convolution of kernels is approximately equivalent to their sum

$$N_0 \lambda^n k^{n*}(x) \approx N_0 \lambda^n n k(x) \tag{D.13}$$

$$\lambda \left(\frac{n+1}{n} \right) k(x_{n+1}) \approx k(x_n), \tag{D.14}$$

which follows from the approach used for thin-tailed kernels (Liu and Kot [2019]). As with thin-tailed kernels, the expression in equation D.14 can be altered to include the evolving growth rate $\lambda_n(\hat{x})$ instead of fixed growth rate λ.

For projecting the approximate wave front, we then initialize the wave front at position $\hat{x}_1$ using the inverse kernel

$$\hat{x}_{n+1} = k^{-1} \left(k(\hat{x}_n) \frac{n}{\lambda_{n+1}(n+1)} \right) \tag{D.15}$$

$$\hat{x}_1 \equiv k^{-1} \left(\frac{\bar{N}}{N_0 \lambda_0} \right) \tag{D.16}$$

As reproduction increases, the denominator of equation D.15 decreases and therefore the rate of advance through the inverse kernel k^{-1} accelerates. As the power law decay order α increases, converging to a thin-tailed distribution as $\alpha \to \infty$, the difference between approximation equation D.15 and analytical equation D.12 shows the bias of the tail-additivity approximation when applied to thin-tailed kernels (Liu and Kot [2019]).

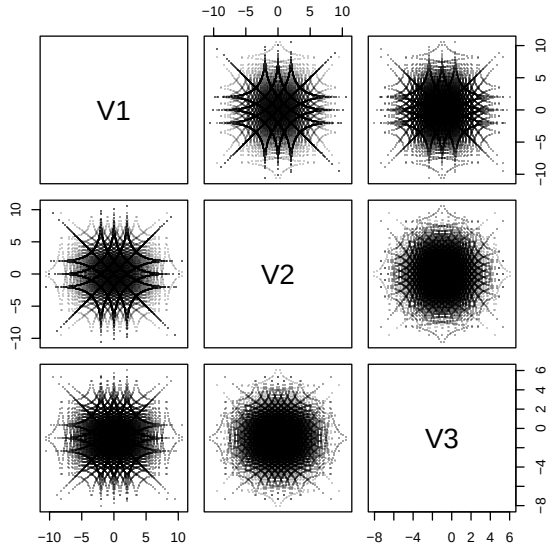

Figure D.1: Example of the Fourier-transformed grid search routine for three parameters. Values are selected to capture total variance of the parameter space without excess duplication. The parameter selections present as periodic functions of one another.

D.2 Inference and future data

D.2.1 Marginal SSE surfaces for wave speed parameters

In our grid search routine over parameters that affect the wave front, we selected 3,000 parameters sets using the Fourier-transformed periodic grid search technique developed for sensitivity analyses (Cukier et al. [1973]). The routine searches the parameter space more efficiently than linear grid searches, such that it captures the variance of without repeating parameter sets in similar areas of the parameter space (figure D.1).

We interpolated SSE surfaces for growth and dispersal from our grid search routine using the marginal SSE profiles in two dimensions. In our evolutionary models, the marginal SSE profiles for dispersal and reproduction showed single optima (figure D.2). Pathogen waves lagged behind the advancing host front, allowing host populations at the wave front to escape selection pressure from pathogen-induced mortality, validating our wave speed

approximation.

However, the marginal profile for cost ω was fairly uniform across the range of parameters that we assessed in both eco-evolutionary models. We could identify that extremely low and extremely high cost values were unrealistic based on the marginal SSE, but a wide range of similar SSE scores across values of cost ω made obtaining a maximum likelihood estimate difficult. We could not easily identify a narrow range for cost parameter estimates because the performance of cost ω depends on initial conditions through the initial average infection risk $\bar{\nu}_0(0)$. Therefore, we would require either estimates of $\bar{\nu}_0(0)$ or cost ω determined independently outside of wave front parameterization.

In order to disentangle cost from initial average infection risk, we therefore need to estimate the average infection risk through experiments. Previous experiments in spongy moth (*Lymantria dispar*) were able to successfully measure both fecundity and infection risk variation as well as estimate heritability (Elderd et al. [2008], Páez et al. [2017]). Previous work shows that fecundity also drops in Douglas-fir tussock moth populations that have undergone high-infection epizootics, even though defoliation from the previous year, a measure of diet quality, was uncorrelated with egg mass size (Mason et al. [1977]). Experiments quantifying fecundity of individuals that survive transmission branch experiments (such as those in Mihaljevic et al. [2020], Dixon [2024]) would allow us to estimate what percentage of this fecundity reduction is due to heritable infection risk changes and what percentage is due to diet quality in high density populations (figure D.6, Dahlsten et al. [1977], Mason et al. [1977]).

Next, we compared our models to defoliation behind the wave front. Because we had already estimated the parameters that were relevant for the wave speed, only heritability b and pathogen overwintering ϕ, survival γ, and decay μ remained uncertain for determining dynamics behind the wave front. We found that simulations with pathogen decay rate $\mu = 1 \times 10^{-4}$ was necessary, confirming the low decay rate of baculovirus in natural popualtions

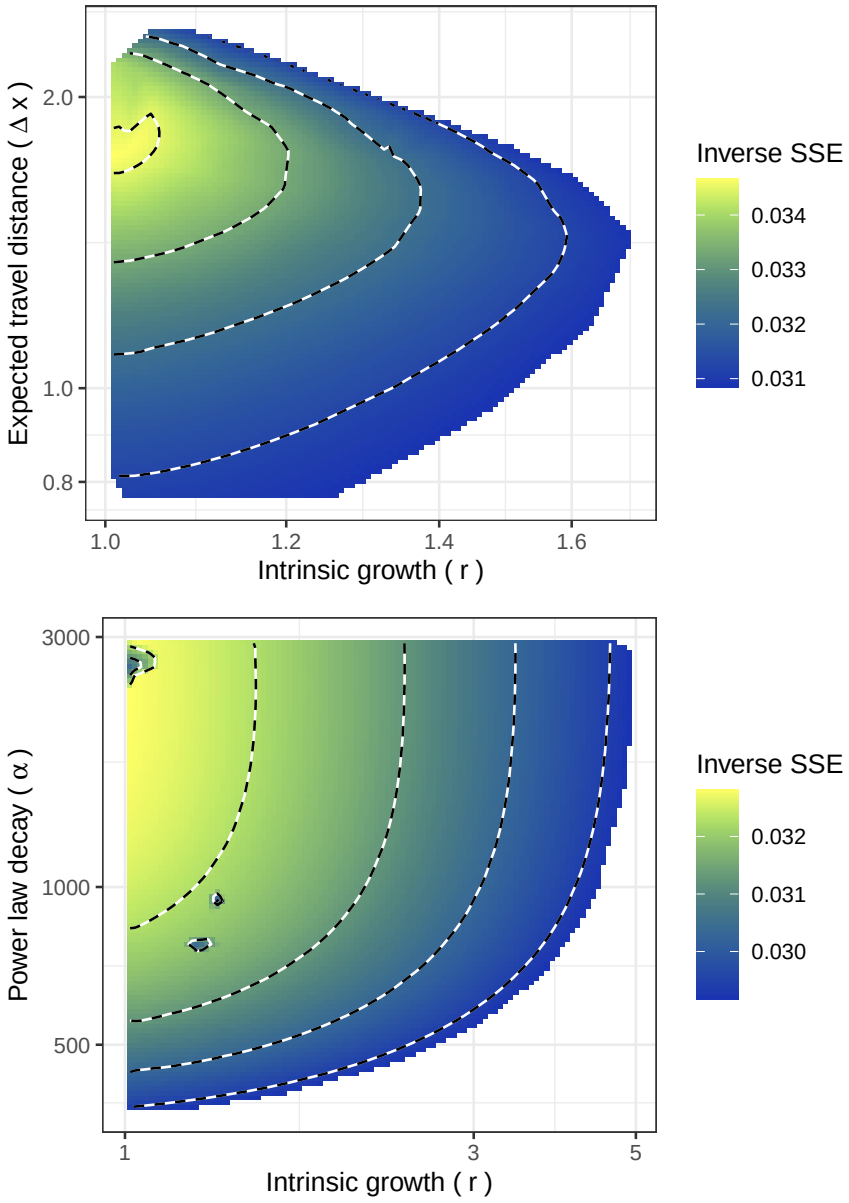

Figure D.2: Marginal SSE surfaces for the evolutionary models. We interpolated over all SSE values less than 40. The top panel shows the surface for the thin-tailed Laplace dispersal kernel, with maximum likelihood estimate from the grid search shown in yellow. The bottom panel shows the surface for the fat-tailed Laplace dispersal kernel, which was less smooth than the surface for the thin-tailed dispersal model. Intrinsic growth r was estimated to be near 1.01 in both models.

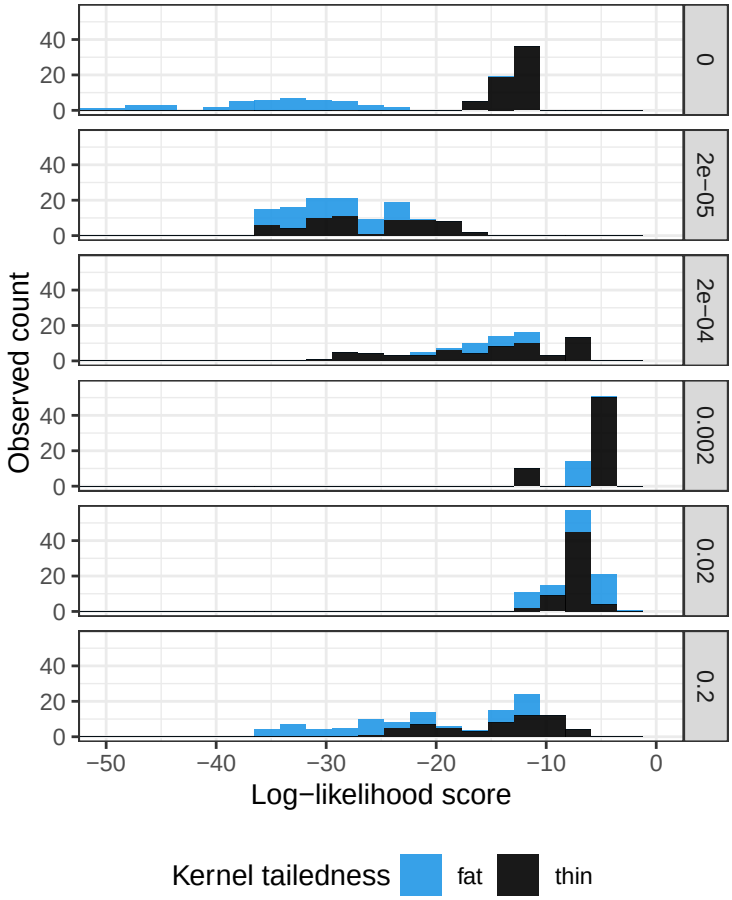

Figure D.3: Model explanations of defoliation in the wake of invasion. Histograms show the distribution of likelihood scores for particular values of heritability b, or $b = 0$ in the models lacking evolution. Models incorporating fat-tailed kernels are shown in blue while those incorporating thin-tailed kernels are shown in black. Histogram is over other parameters with ϕ, γ, and μ varying along with initial year of introduction being either 1995, 1996, or 1997.

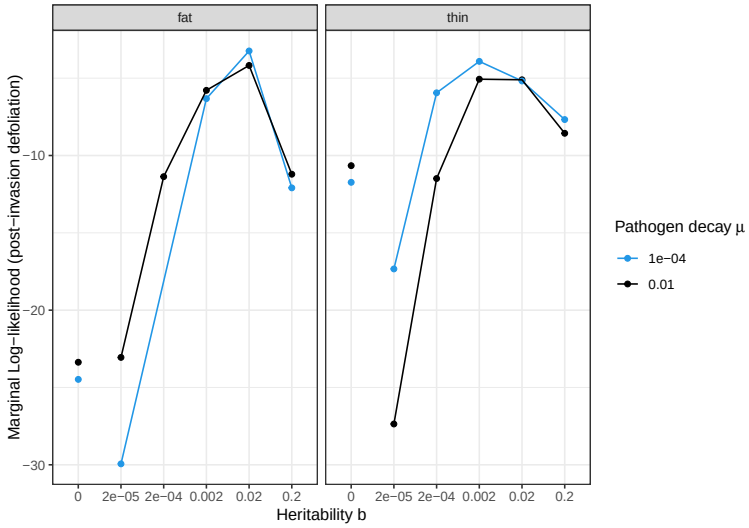

Figure D.4: Marginal likelihood profiles across heritability b. Each panel shows the dispersal function with either a fat- (left) or thin-tailed (right) kernel. Heritability $b = 0$ indicates the non-evolutionary models, which are separated from the evolutionary model marginal values of b. The maximum likelihood suggest $b = 0.02$ (fat) or $b = 0.002$ (thin) for evolutionary models. Color indicates pathogen decay μ, where blue shows low rates of decay $\mu = 1 \times 10^{-4}$ and black shows higher rates of decay $\mu = 1 \times 10^{-2}$.

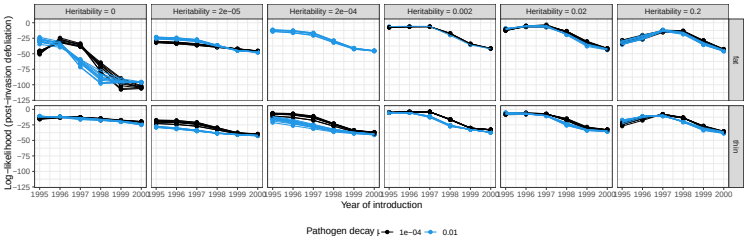

Figure D.5: Marginal likelihood profiles across year of first re-introduction. Each panel shows the dispersal function with either a fat- (top) or thin-tailed (bottom) kernel. Heritability $b = 0$ indicates the non-evolutionary models. The curves show that later re-introduction times, between 1998 and 2000, are unable to reproduce the data. Slight peaks indicate that 1997 is the maximum likelihood estimate of re-introduction time, although it performs comparably to 1995 and 1996. Color indicates pathogen decay μ, where blue shows low rates of decay $\mu = 1 \times 10^{-4}$ and black shows higher rates of decay $\mu = 1 \times 10^{-2}$.

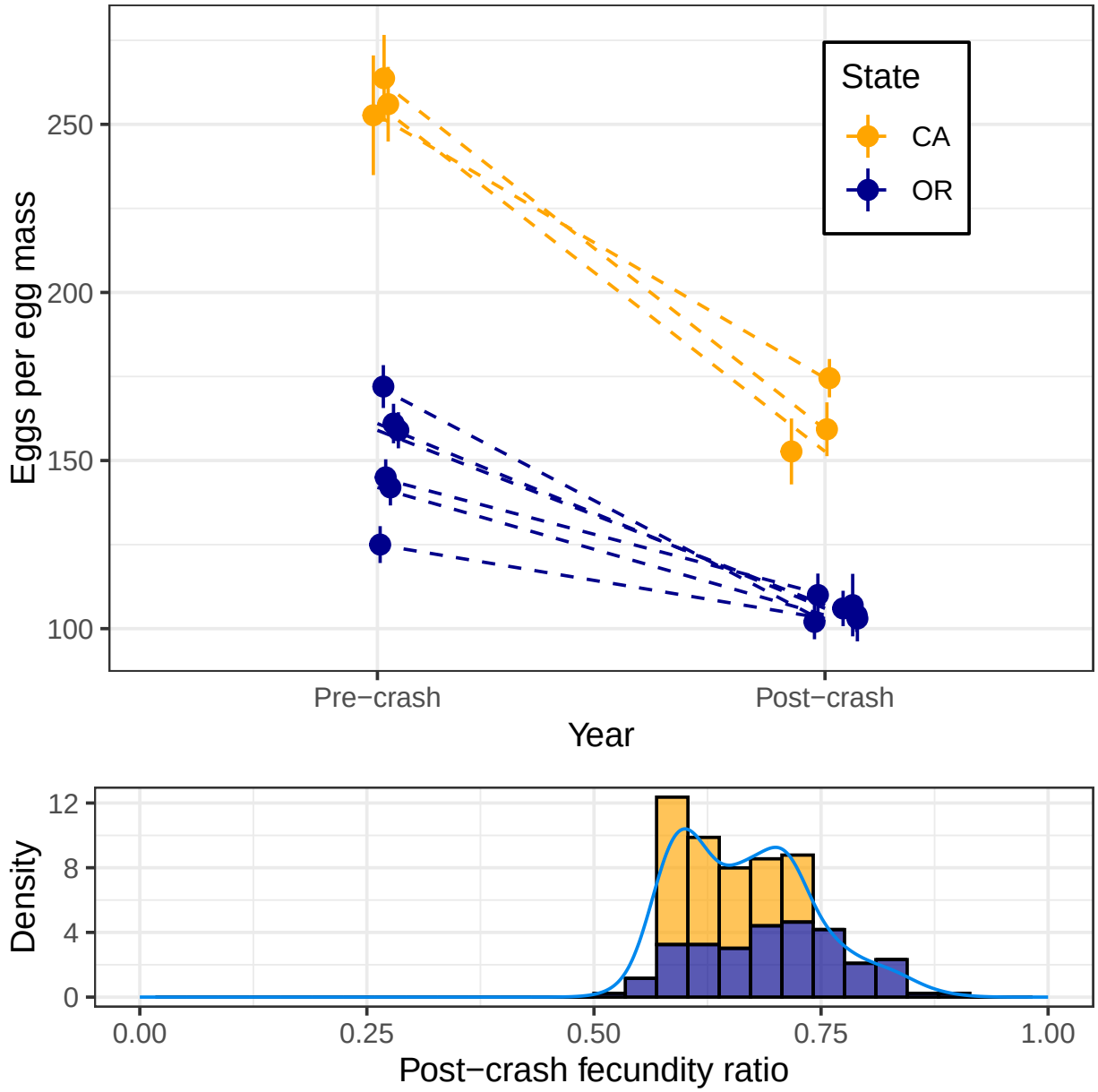

Figure D.6: Top panel shows absolute changes in eggs per egg mass during two epizootics, taken from Dahlsten et al. [1977] (California outbreak 1971-72, Orange) and Mason et al. [1977] (Oregon outbreak 1972-73, navy). Bottom panel shows the distribution of fecundity ratios after population crash due to viral mortality and other factors. Decreases in fecundity were not correlated with generalist parasitoids Dahlsten et al. [1977] or defoliation level Mason et al. [1977]

(Mihaljevic et al. [2020]). We found that while heritability $b = 2 \times 10^{-3}$ covered most of the defoliation data set it led to dampening oscillations (figure **??**). Higher pathogen decay rate $\mu = 1 \times 10^{-2}$ consistently lowered model ability to explain the data in the wake of invasion, independent of other grid search parameters or year of re-introduction (figure **??**). These findings were robust to values of overwintering $\phi = 5, 10, 12, 15$, and 25, as well as values of pathogen survival $\gamma = 0.05$ and 0.1, which cover the range of parameter estimates from previous eco-evolutionary studies of forest insects (Elderd et al. [2008], Páez et al. [2017], Dwyer et al. [2022], Dixon [2024]). The best-fit year of re-introduction was 1997, but most years of re-introduction also demonstrated that heritability $b \geq 2 \times 10^{-3}$ were the better estimates to cover the defolaition data (figure **??**).

D.2.2 A novel range expansion following re-establishment

In addition to defoliation from re-establishing Douglas-fir tussock moth populations, insect damage also appeared in areas that have never been previously defoliated. These new populations are not unexpected, as the Douglas-fir tussock moth range is shifting under climate change (Dixon [2024]). However, the novel westward expansion meant we could not use the same one-dimensional simulations from the 2000-2007 outbreaks (figure D.7). We can still use our approach by isolating the 2020-2022 expansion, as the extent of this synchronized defoliation does still resembles our integrodifference simulations qualitatively.

Although the range expansion appeared suddenly in 2020, instead of presenting as a travelling wave, defoliation appeared at clustered distances that were similar to the distribution of high host densities from our integrodifference models (figure D.7). As forest cover is uniform over the extent of this novel range expansion, the clustering cannot be explained by habitat patchiness. According to the best parameters from the eco-evolutionary model with a thin-tailed Laplace dispersal kernel, the extent of the 2020 defoliation presence could be from a range expansion that began 14 years prior in 2006.

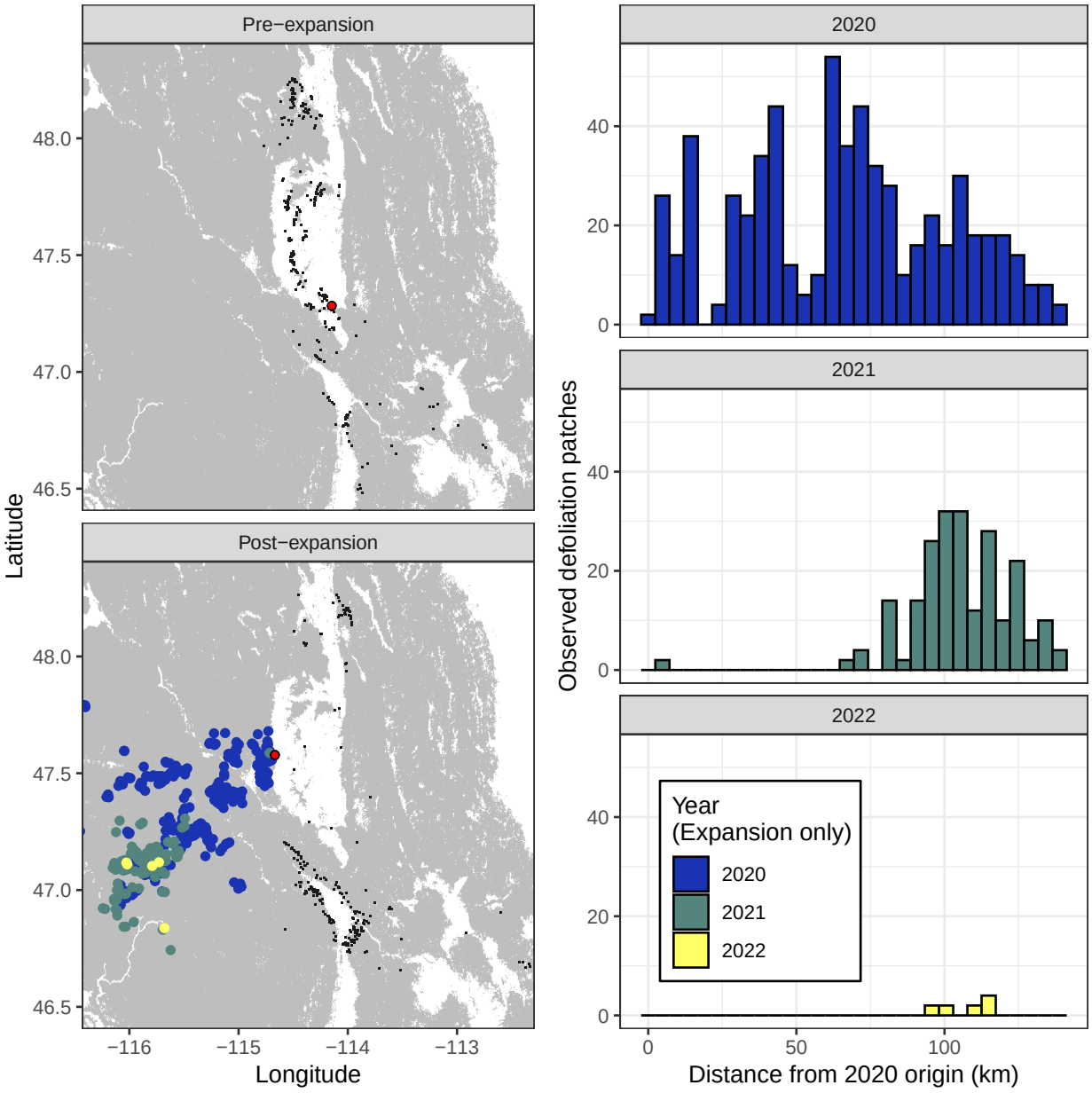

Figure D.7: The new establishment of populations in areas without any defoliation history. Left panels show defoliation before (top) and after (bottom) the range expansion, with black dots representing areas with defoliation history and colored dots representing areas that are novel invasions. Habitable forest cover is shown in grey while uninhabitable non-forest cover is shown in white. The right panels show distances from the putative 2020 origin, the nearest defoliation to previously defoliated areas, as histograms. Clustered distances show possible cycling patterns that were below the threshold for causing defoliation damage but then later emerged as outbreaking densities.

Despite spatial clustering, the timing of spread is still uncertain because defoliation is only a proxy for actual insect density during the expansion. Further, it is possible that the dampened oscillations of lower values of heritability $b = 0.002$ may lead to synchrony in the wake of invasion, and thus our estimates of heritability may be overly high. Extending models to allow for mechanisms that vary population dynamics, as discussed in Chapter 3, may provide insight into these novel expansions, but ultimately population surveillance and infection risk experiments will be necessary to draw meaningful conclusions.

APPENDIX E

NUMERICAL METHODS FOR SPATIAL SIMULATIONS

E.1 Method of lines integration for PDEs

We discretized our continuous space reaction diffusion equations using method of lines. The second derivative with respect to x is

$$\frac{\partial S(x,t)}{\partial t} = D\frac{\partial^2 S(x,t)}{\partial x^2} \tag{E.1}$$

$$\frac{dS_x(t)}{dt} = D\left[-S_x + \frac{1}{n}\sum_{y=1}^{n} S_y\right] \tag{E.2}$$

where location x has n neighbors. In one dimension, $n = 2$, while in a 2D hexagonal grid lattice, $n = 6$.

The discretization of the cross-product of the two first derivatives might be of a similar form to equation E.2 but, in order to avoid it, we can rearrange $\frac{\partial \nu(x,t)}{\partial t}$ to have only second derivatives with respect to x. We do this by reintroducing s_1. As before, we derive the expressions for $m_1 \equiv \bar{\nu}$

$$\frac{\partial \nu(x,t)}{\partial t} = -\nu^2 C^2 P + D\left[\frac{\partial^2 \nu}{\partial x^2} + \frac{2}{S}\frac{\partial \nu}{\partial x}\frac{\partial S}{\partial x}\right] \tag{E.3}$$

$$\frac{\partial m_1}{\partial t} = -m_1^2 C^2 P + \frac{D}{s_0}\left[s_0\frac{\partial^2 m_1}{\partial x^2} + 2\frac{\partial m_1}{\partial x}\frac{\partial s_0}{\partial x}\right] \tag{E.4}$$

Taking the identity from equation A.44, where

$$\frac{\partial^2 s_1}{\partial x^2} = \frac{\partial(s_0, m_1)}{\partial x^2} = 2\frac{\partial(m_1, s_0)}{\partial x^2} + m_1\frac{\partial^2 s_0}{\partial x^2} + s_0\frac{\partial^2 m_1}{\partial x^2} \tag{E.5}$$

we can see that the component inside the brackets of equation E.4 is related to the second central spatial moment by

$$\frac{1}{s_0}\left[s_0\frac{\partial^2 m_1}{\partial x^2}+2\frac{\partial m_1\partial s_0}{\partial x^2}\right]=\frac{1}{s_0}\left[\frac{\partial^2 s_1}{\partial x^2}-m_1\frac{\partial^2 s_0}{\partial x^2}\right]. \tag{E.6}$$

Now we can proceed as in equation E.1 and substitute the definition $s_1 = m_1 s_0 = \nu S$ after we discretize.

$$\frac{\partial m_1}{\partial t}=-m_1^2C^2P+\frac{D}{s_0}\left[\frac{\partial^2 s_1}{\partial x^2}-m_1\frac{\partial^2 s_0}{\partial x^2}\right] \tag{E.7}$$

$$\frac{dm_1}{dt}=-m_1^2C^2P+\frac{D}{s_0}\left[-s_{1,x}+\frac{1}{n}\sum_{y=1}^{n}s_{1,y}\right]-\frac{Dm_1}{s_0}\left[-s_{0,x}+\frac{1}{n}\sum_{y=1}^{n}s_{0,y}\right] \tag{E.8}$$

$$\frac{d\nu_x}{dt}=-\nu_x^2C^2P_x+\frac{D}{S_x}\left[-\nu_xS_x+\frac{1}{n}\sum_{y=1}^{n}\nu_yS_y\right]-\frac{D\nu_x}{S_x}\left[-S_x+\frac{1}{n}\sum_{y=1}^{n}S_y\right] \tag{E.9}$$

$$=-\nu_x^2C^2P_x+\frac{D}{S_x}\left[\frac{1}{n}\sum_{y=1}^{n}\nu_yS_y-\frac{\nu_x}{n}\sum_{y=1}^{n}S_y\right] \tag{E.10}$$

$$=-\nu_x^2C^2P_x+\frac{D}{nS_x}\sum_{y=1}^{n}S_y(\nu_y-\nu_x) \tag{E.11}$$

The factor of 2 in the left hand side of equation E.6 goes away, so that we only have parameters and classes that have explicit biological meaning in our final discretized ODE system

$$\frac{dS_x(t)}{dt} = -\nu_x P_x S_x + \frac{D}{n}\sum_{y=1}^{n}(S_y - S_x) \tag{E.12}$$

$$\frac{d\nu_x(t)}{dt} = -\nu_x^2 C^2 P_x + \frac{D}{nS_x}\sum_{y=1}^{n} S_y(\nu_y - \nu_x) \tag{E.13}$$

$$\frac{dE_{1,x}(t)}{dt} = \nu_x P_x S_x - m\delta E_{1,x} + \frac{D}{n}\sum_{y=1}^{n}(E_{1,y} - E_{1,x}) \tag{E.14}$$

$$\frac{dE_{i,x}(t)}{dt} = m\delta E_{i-1} - m\delta E_i + \frac{D}{n}\sum_{y=1}^{n}(E_{i,y} - E_{i,x}) \quad (i \in [2, m]) \tag{E.15}$$

$$\frac{dP_x(t)}{dt} = m\delta E_{m,x} - \mu P_x \tag{E.16}$$

E.2 Exact stochastic simulation algorithms

Agent-based simulations typically implement an algorithm that produces an exact stochastic simulation, often referred to in biology as the Gillespie algorithm (algorithm 3, Gillespie [1977]). Briefly, the exact stochastic simulation algorithm computes the rate $\alpha_\omega(t)$ at which each interaction or "event" ω in a model is occurring at time t. We calculate the total rate at which events are occurring at time t by summing all of these event rates

$$\alpha_\Omega(t) = \sum_{\omega=1}^{\Omega} \alpha_\omega(t). \tag{E.17}$$

The time to the next event is exponentially distributed according to the total rate $\alpha_\Omega(t)$ and the probability of a particular event ω occurring at the specified time is taken to be the relative proportion of its rate $\alpha_\omega(t)$ to the total rate of all events occurring.

The first issue in using the exact stochastic algorithm 3 for our spatial model is that it assumes a homogeneously mixing population. A simple fix for this issue is to assign local rates of each event type of interest, meaning that rates of transmission, mortality, and

Algorithm 3: Exact stochastic simulation

$\Omega \equiv$ set of all possible events (e.g. exposure, mortality, decay);
while $[E(t) + P(t)] > 0$ *and* $t < t_f$ **do**
  Initialize $\alpha_\Omega(t) = 0$;
  for *event* ω *in* Ω **do**
    compute event rate $\alpha_\omega(t)$;
    $\alpha_\Omega(t)$ += $\alpha_\omega(t)$;
  end
  generate $\tau \sim \text{Exp}\left(\alpha_\Omega(t)^{-1}\right)$;
  select event ω with probability $\frac{\alpha_\omega(t)}{\alpha_\Omega(t)}$;
  execute ω;
  t += τ;
end

cadaver decay are based on local populations in each patch grid cell, not the global population size, familiar as the household model of statistical epidemics Andersson and Britton [1998], Britton et al. [2011, 2020]. We denote the rate at which event ω occurs in patch x at time t as $\alpha_\omega(x, t)$. This yields more frequent events that stem from more agent types, but avoids violating the homogeneous mixing assumption.

However, these simulations become more computationally-intensive from this workaround. In order to fit our model to data, we need to execute many events rapidly and reduce computation time. To do this, we use a hybrid τ-selection routine (algorithm 4) Cao et al. [2007], Simoni et al. [2019]. This routine assigns events $\alpha_\omega(x, t)$ into two sets: the "leap" set and the "exact" set. These two sets aim to approximate the exact stochastic algorithm by selecting time steps that are small enough to not considerably alter the dynamics of the system.

Events belong to the exact set if they involve a class of agents (susceptible larvae, infected larvae, or infectious cadavers) that have fewer than some threshold θ individuals. Events in this set are chosen to occur in a manner similar to algorithm 3 but are described in full by algorithm 4. The exact event set deals with cases where even one or two events have a relatively large impact on the fate of a population. The leap event set includes those events that involve only populations above our specified threshold, meaning that multiple events

will have a relatively smaller impact on the overall dynamics. Leap events $\alpha_\omega(x,t) \in \vec{\alpha}_{\text{leap}}$ occur according to Poisson distribution with expectation $\tau\alpha_\omega(x,t)$, where time step τ is chosen to minimize changes to system dynamics Cao et al. [2007].

If the local effective transmission rate $\alpha_\nu(x,t)$ is a leap event, meaning that the susceptible population $S(x,t)$ is greater than threshold θ, then we select the new value of $\nu(x,t+\tau)$ in a non-random fashion that depends on a random number of stochastic events by setting

$$\nu(x,t+\tau) = \nu(x,t)\left[\frac{S(x,t)-k_x}{S(x,t)}\right]^{C_V^2} \tag{E.18}$$

where k_x is the Poisson-distributed number of infection events that occurred during leap τ. We always consider movement between two locations to be in the exact set, regardless of population size, to avoid violating homogeneity assumptions of leap events.

Infection risk heterogeneity across individuals and across space is simulated by tracking the total, local effective transmission risk $\nu(x,t)$, as in the PDE system. We initialized $\nu(x,0)$ for each discretized grid point in space as a gamma-distributed random variable with shape parameter $S(x,0)C^{-2}$ and scale parameter $\nu(x,0)C^2$. The total transmission risk is the sum across all individual transmission risks. To account for the change in total effective transmission after an infection takes place, we borrow the deterministic moment closure approximation equation A.1.

If fewer than threshold $\theta = 20$ susceptible individuals remain in patch x (Cao et al. [2006, 2007]), we assign individual infection risks ν_i for each agent host i. The values of ν_i are gamma-distributed with shape parameter C^{-2} and scale parameter $\nu(x,t)C^2$ and sum to $S(x,t)\nu(x,t)$. If the exact transmission event affecting one individual $\alpha_\nu(x,t)$ is selected to occur under algorithm 4, we remove one individual i with probability

$$p_\nu(i) = \frac{\nu_i}{\sum_j^S \nu_j} \tag{E.19}$$

Algorithm 4: Hybrid τ-selection

$\theta \equiv$ threshold population for exact stochastic algorithm;
$\epsilon \equiv$ bound on population size change;
$\Omega \equiv$ events (e.g. exposure, mortality, decay);
while $[E(t) + P(t)] > 0$ *and* $t < t_f$ **do**
  for *patch* $x \in (1, X]$ **do**
    for *local event* ω_x *in* Ω_x **do**
      if $N_i > \theta$ **then**
        calculate $\tau_\omega(x,t)$: max τ allowing $\Delta N_x < \epsilon$ given $\alpha_\omega(x,t)$);
        append $\tau_\omega(x,t)$ to list $\vec{\tau}_{\text{leap}}$;
        append $\alpha_\omega(x,t)$ to list $\vec{\alpha}_{\text{leap}}$;
      else
        append $\alpha_\omega(x,t)$ to list $\vec{\alpha}_{\text{exact}}$;
      end
    end
    if *movement allowed* **then**
      append $\alpha_{\omega=M}(x,t)$ to list $\vec{\alpha}_{\text{exact}}$;
    end
  end
  set $\tau_{\text{leap}} = \min(\vec{\tau}_{\text{leap}})$;
  calculate $\alpha_\Omega = \sum \vec{\alpha}_{\text{exact}}$;
  generate $\tau_{\text{exact}} \sim \text{Exp}\left(\alpha_\Omega^{-1}\right)$;
  if $\tau_{leap} < \tau_{exact}$ **then**
    take $\tau = \tau_{\text{leap}}$;
  else
    take $\tau = \tau_{\text{exact}}$;
    select 1 exact event $\omega_x \in \vec{\alpha}_{\text{exact}}$ with probability $\frac{\alpha_\omega(x,t)}{\alpha_\Omega}$;
    execute ω_x once
  end
  for $\alpha_\omega(x,t)$ *in* $\vec{\alpha}_{leap}$ **do**
    generate $k_x \sim \text{Pois}(\tau\alpha_\omega(x,t))$;
    execute ω_x k_x times;
  end
  $t \mathrel{+}= \tau$;
end

and then subtract the individual infection risk from the total effective transmission rate. We then add the individual to the exposed class, where it has no identifying characteristics besides time to mortality. We set time to death of an exposed individual as the constant $\delta^{-1} + t_\nu$, with t_ν being the time of exposure. This is equivalent to setting the number of exposed classes m in equations (A.52-A.56) equal to ∞, although in practice $m \in (50, 100)$ exposure classes also have almost zero variance in time to mortality (Lloyd [2001]). We used $m = 100$ in our differential equations models to closely approximate our zero-variance mortality times in the agent-based model.

E.3 Environmental stochasticity

We incorporate environmental stochasticity by randomly fluctuating coefficients in the transmission term by a factor of $\exp(\epsilon_\tau)$. Specifically, for each day τ, we drew a new value of the random variable ϵ_τ from a normal distribution with variance σ^2 and mean $-\frac{\sigma^2}{2}$. We then exponentiated each value ϵ_τ, yielding parameter fluctuations that followed a log-normal distribution that is strictly positive with an expectation of one. An expectation of one, generated by the adjustment term $-\frac{\sigma^2}{2}$, allowed the estimated average transmission rate to be consistent across models incorporating environmental stochasticity and models lacking such fluctuations. The effects on the transmission rate are strictly positive as negative values would lead to cadaver-host interactions producing healthy hosts from infected individuals. Therefore for each day $\tau \in (1, T)$

$$\frac{dS_\tau}{dt} = -\bar{\nu} S_\tau P_\tau e^{\epsilon_\tau} \left(\frac{S_\tau(t)}{S_1(0)} \right)^{C^2} \tag{E.20}$$

This is essentially an assumption that each day in the simulation has random unknowable effects on transmission that either reduce transmission rate to 0 or inflate it to much higher values modulated by σ^2. The mode of this distribution becomes greatly shifted toward

zero with increasing variance in ϵ_τ. This case yields few days with high transmission and many days with very low transmission, in contrast to an un-adjusted distribution that would otherwise produce many days of transmission in the neighborhood of $\bar{\nu}\exp(\sigma^2)$ and some days with incredibly high transmission rates. This is important to note because we use the same priors in fitting $\bar{\nu}$ and C, regardless of whether we incorporate environmental stochasticity. But if the mean transmission is inflated we will have misspecified posteriors, particularly on $\bar{\nu}$, which interact differently with each model. The adjustment therefore serves a dual purpose of maintaining consistency of the effect from priors and of preventing model crashout for the extreme values of σ.

E.4 Grid lattices, diffusion, and travelling waves

We initialized host and pathogen densities with a multinomial distribution at each point in space by calculating the total size of the population and then distributing individual densities. Specifically, we multiplied the average density by the number of grid points to be initialized and assigned integer densities of hosts and cadavers to each location according to a multinomial distribution. Because mean densities were fit separately for each study population and each grid point had equal probability in the multinomial distribution, the initial distribution of hosts and pathogens reflected the observed larval densities of our study populations and assumed no initial overdispersion.

"Periodic" boundaries, which we use across the simulations in this study, bring any individuals that leave the grid to wrap around to another point in the grid. Periodic boundaries have the advantage that they reduce aberrant behavior at the boundaries of the grid compared to the center and do not alter the total population size. We can imagine then that our 2D hexagonal grid lattice with periodic boundaries represents a sample from a level in the forest canopy where exposed and susceptible hosts can move with equal efficiency. If an individual leaves the grid, we therefore are assuming that an individual of the same

type replaces it on the opposite side of the grid instead of the individual itself being able to transport to that area.

It is convenient for many reasons to have consistent rules about storing population sizes and other features of the grid. We use a one-dimensional array in C to track grid points and use indexing geometry and simple mod rules for calculating the indices of neighboring grid points in a periodic hexagonal lattice.

```
switch (direction_of_travel)
{
 case 0: destination = modulo(origin + 1, gridsize);
  break;
 case 1: destination = modulo(origin + 2 - 3 * length, gridsize);
  break;
 case 2: destination = modulo(origin + 3 * length - 1, gridsize);
  break;
 case 3: destination = modulo(origin - 1, cells);
  break;
 case 4: destination = modulo(origin + 3 * length - 2, gridsize);
  break;
 case 5: destination = modulo(origin + 1 - 3 * length, gridsize);
  break;
}
```

where length is our parameter l that denotes the grid points along a single side of the simulation and grid size n is calculated from that using

$$n = 3l(l-1) + 1 \tag{E.21}$$

The destination mod grid size ensures that destination indices are strictly positive and work for periodic boundaries. The indexing is laid out so that the mod movement arithmetic can be followed according to figure E.1.

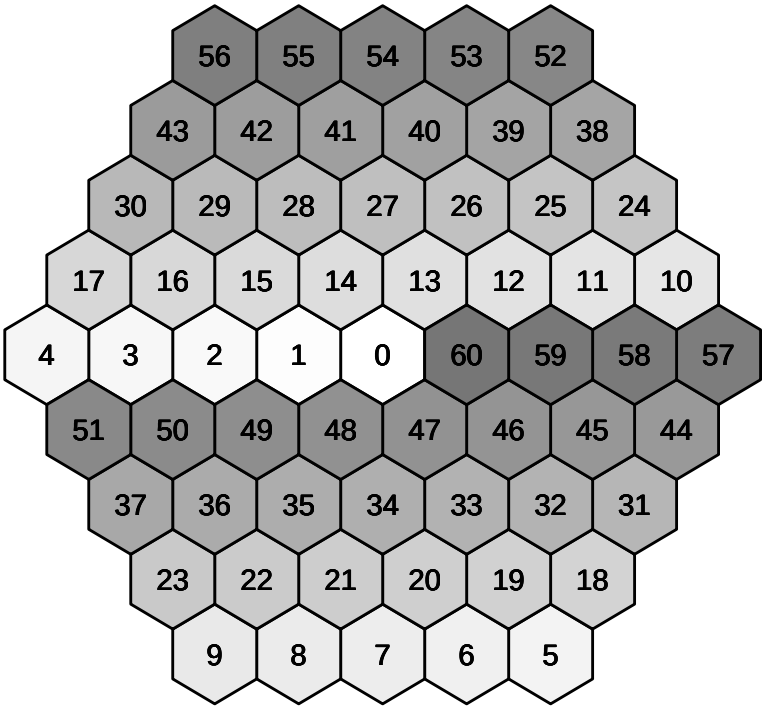

Figure E.1: Orientation of indexing so that direction of travel is easily selected with mod rules.

Due to the lack of assumptions about nearest neighbor movements, hexagonal grids have the further advantage of being a stable discretization of the diffusion process, meaning simple rules for translating distance between grid points into the diffusion constant Wood and Thomas [1996]. If we denote the densities of a particular class $F(x, y)$ and we denote the discretized populations f_{1-6} as six neighbors of a central grid point f_C, then

$$\frac{\partial^2 F}{\partial x^2} + \frac{\partial^2 F}{\partial y^2} \approx \frac{1}{3(\Delta x)^2} \left(\sum_{i=1}^{6} f_i - 6 f_C \right) \tag{E.22}$$

We can set the patch width Δx equal to l^{-1}, where l is the number of hexagons that make up a single side of a hexagonal grid. This fixes the absolute length of the grid for different grid sizes and takes the distance between centers of each hexagon as the width. The scale-free spatial grid allows us to assume that the densities in the simulation align with our data upon model fitting and provides consistency across spatial grid sizes while simulating the models.

Movement rates are set in units of inter-patch transitions per larva per day. These rates increase to saturation over the course of the epizootic, modelling larval growth and increasing movement propensity. The movement rate as a function of larval development, and therefore time, is a Michaelis-Menten function, where the terminal rate of movement, k_1, is determined by the relationship between the diffusion coefficient and the width of a patch in the hexagonal grid lattice following equation E.22.

$$\frac{k_1 t}{k_2 + t} = \frac{D l^2 t}{3(k_2 + t)} \tag{E.23}$$

In practice we are only fitting k_1 and k_2 while we calculate real-time movement probabilities according to the Michaelis-Menten calculation as a function of grid size.

In models that allow for the diffusion of infectious cadavers, we assume that pathogen diffusion occurs due to first instar exposed movement and simplify by including these in the infectious class P. Instead of a Michaelis-Menten saturating function, we assume that "cadaver diffusion" is either constant, meaning the continuous dispersal of first instars and occlusion bodies over foliage, or the rate decays according to the incubation period parameter δ, meaning that we only consider first instar larvae to diffuse and then die of infection.

The expression for change in pathogen over time then is

$$\frac{\partial P}{\partial t} = -\mu P + (1 - \mathrm{CDF}(E|m, \delta)) D \nabla P \tag{E.24}$$

Travelling waves from pathogen point releases stopped in the fitted agent-based model but continued when pathogens were represented as infinitesimal densities in the best spatial model, which only allowed for host diffusion (Figure E.2). Waves stopped due to extinction by drift, where exposed individuals with low diffusion rates did not tend to leave the patch in which they were infected. For faster diffusion rates, travelling waves continued in both models, but these faster rates were orders of magnitude above our point estimates for the reaction-diffusion model (figure B.7.

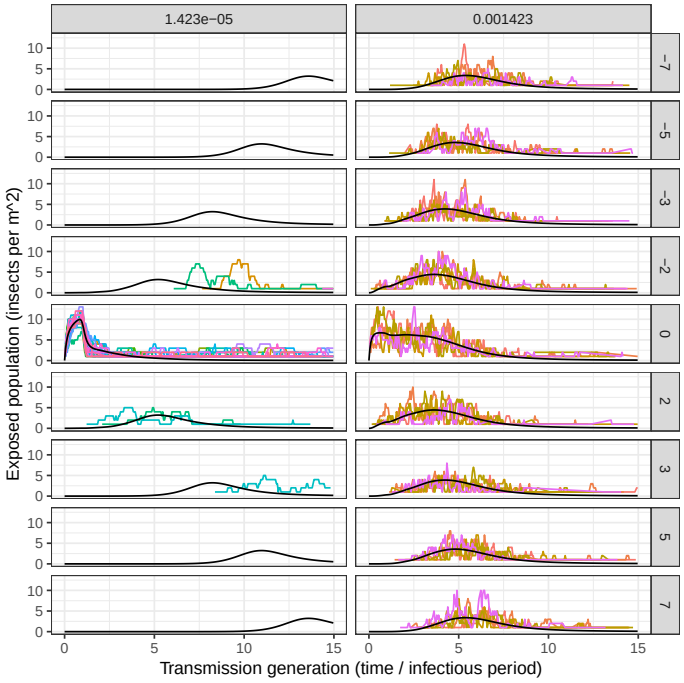

Figure E.2: Comparison of agent-based and PDE exposed class waves from point release of infectious cadavers. Facet rows show x-position distance from the origin in a 2D lattice. The column at left shows the mean posterior fitted agent-based parameter values. The column at right shows a diffusion constant two standard deviations above the mean (100-fold increase) while holding densities and other epizootic parameters constant. Solid black lines show the PDE solutions given the same parameters of each column. The agent-based simulation can only match the PDE for considerably high movement speeds of exposed individuals.

E.5 Time step calculations in integrodifference equations

The integration of continuous spatial domains is prone to numerical error. To reduce that error, we used Simpson's integration rule over space and used a high number of discretized grid point steps. Simpson's rule,

$$\int_a^b f(x)dx \approx \frac{b-a}{6}\left[f(a)+4f\left(\frac{a+b}{2}\right)+f(b)\right] \tag{E.25}$$

$$= \frac{1}{3}h\left[f(a)+4f\left(a+h\right)+f(b)\right], \tag{E.26}$$

allows for more robust integration when functions contain both high and low values, as is naturally the case when densities of hosts are invading empty landscapes and particularly the case when dispersal kernels are fat-tailed. We used $2 \times 10^{18} + 1$ integration steps using the observed moments of $S_n(\nu, x)$ directly followed by calculation of $V_n(x)$ and $\bar{\nu}_n(x)$.

REFERENCES

Karen C. Abbott and Greg Dwyer. Using Mechanistic Models to Understand Synchrony in Forest Insect Populations: The North American Gypsy Moth as a Case Study. *The American Naturalist*, 172(5):613–624, November 2008. ISSN 0003-0147, 1537-5323. doi:10.1086/591679. URL https://www.journals.uchicago.edu/doi/10.1086/591679.

René I. Alfaro and Roy F. Shepherd. Tree-Ring Growth of Interior Douglas-Fir After One Year's Defoliation by Douglas-Fir Tussock Moth. *Forest Science*, 37(3):959–964, August 1991. ISSN 0015-749X. doi:10.1093/forestscience/37.3.959. URL https://doi.org/10.1093/forestscience/37.3.959.

Linda J.S. Allen. A primer on stochastic epidemic models: Formulation, numerical simulation, and analysis. *Infectious Disease Modelling*, 2(2):128–142, 2017. ISSN 24680427. doi:10.1016/j.idm.2017.03.001. URL http://dx.doi.org/10.1016/j.idm.2017.03.001. Publisher: Elsevier Ltd.

Linda JS Allen, Ben M. Bolker, Yuan Lou, and Andrew L. Nevai. Asymptotic profiles of the steady states for an SIS epidemic reaction-diffusion model. 2008. URL https://pdfs.semanticscholar.org/3916/90733c81a774f3bafabd93c142ab92f59ec3.pdf. Publisher: AIMS PRESS.

David Alonso, Alan J McKane, and Mercedes Pascual. Stochastic amplification in epidemics. *Journal of The Royal Society Interface*, 4(14):575–582, December 2006. doi:10.1098/rsif.2006.0192. URL https://royalsocietypublishing.org/doi/full/10.1098/rsif.2006.0192. Publisher: Royal Society.

R. M. Anderson, H. C. Jackson, R. M. May, and A. M. Smith. Population dynamics of fox rabies in Europe. *Nature*, 289(5800):765–771, February 1981. ISSN 0028-0836. doi:10.1038/289765a0.

Håkan Andersson and Tom Britton. Heterogeneity in epidemic models and its effect on the spread of infection. *Journal of Applied Probability*, 35(3):651–661, 1998. ISSN 00219002. doi:10.1239/jap/1032265213.

Shweta Bansal, Bryan T Grenfell, and Lauren Ancel Meyers. When individual behaviour matters: homogeneous and network models in epidemiology. *Journal of The Royal Society Interface*, 4(16):879–891, October 2007. ISSN 1742-5689, 1742-5662. doi:10.1098/rsif.2007.1100. URL https://royalsocietypublishing.org/doi/10.1098/rsif.2007.1100.

Roy C. Beckwith. Influence of host foliage on the Douglas-fir tussock moth. *Environmental Entomology*, 5(1):73–77, 1976. URL https://academic.oup.com/ee/article-abstract/5/1/73/2395704. Publisher: Oxford University Press Oxford, UK.

Craig W. Benkman. The Selection Mosaic and Diversifying Coevolution between Crossbills and Lodgepole Pine. *The American Naturalist*, 153(S5):S75–S91, May 1999. ISSN 1537-5323. doi:10.1086/303213.

Jamie J.R. Bennett and Jonathan A. Sherratt. How do dispersal rates affect the transition from periodic to irregular spatio-temporal oscillations in invasive predator–prey systems? *Applied Mathematics Letters*, 94:80–86, August 2019. ISSN 08939659. doi:10.1016/j.aml.2019.02.013. URL https://linkinghub.elsevier.com/retrieve/pii/S0893965919300709.

Ottar N. Bjørnstad, Mikko Peltonen, Andrew M. Liebhold, and Werner Baltensweiler. Waves of Larch Budmoth Outbreaks in the European Alps. *Science*, 298(5595):1020–1023, November 2002. ISSN 0036-8075, 1095-9203. doi:10.1126/science.1075182. URL https://www.science.org/doi/10.1126/science.1075182.

Ottar N. Bjørnstad, Andrew M. Liebhold, and Derek M. Johnson. Transient synchronization following invasion: revisiting Moran's model and a case study. *Population Ecology*, 50(4):379–389, October 2008. ISSN 1438-3896, 1438-390X. doi:10.1007/s10144-008-0105-5. URL https://esj-journals.onlinelibrary.wiley.com/doi/10.1007/s10144-008-0105-5.

Gert Jan Boender, Rob van den Hengel, Herman J. W. van Roermund, and Thomas J. Hagenaars. The Influence of Between-Farm Distance and Farm Size on the Spread of Classical Swine Fever during the 1997–1998 Epidemic in The Netherlands. *PLOS ONE*, 9(4):e95278, April 2014. ISSN 1932-6203. doi:10.1371/journal.pone.0095278. URL https://journals.plos.org/plosone/article?id=10.1371/journal.pone.0095278. Publisher: Public Library of Science.

Benjamin Bolker and Stephen W Pacala. Using Moment Equations to Understand Stochastically Driven Spatial Pattern Formation in Ecological Systems. *Theoretical Population Biology*, 52(3):179–197, December 1997. ISSN 0040-5809. doi:10.1006/tpbi.1997.1331. URL https://www.sciencedirect.com/science/article/pii/S0040580997913319.

Tyler R. Bonnell, Ria R. Ghai, Tony L. Goldberg, Raja Sengupta, and Colin A. Chapman. Spatial patterns of persistence for environmentally transmitted parasites: Effects of regional climate and local landscape. *Ecological Modelling*, 338:78–89, 2016. ISSN 03043800. doi:10.1016/j.ecolmodel.2016.07.018. URL http://dx.doi.org/10.1016/j.ecolmodel.2016.07.018. Publisher: Elsevier B.V.

Romulus Breban, John M. Drake, David E. Stallknecht, and Pejman Rohani. The role of environmental transmission in recurrent avian influenza epidemics. *PLoS computational biology*, 5(4):e1000346, 2009. URL https://journals.plos.org/ploscompbiol/article?id=10.1371/journal.pcbi.1000346. Publisher: Public Library of Science San Francisco, USA.

Carles Bretó, Daihai He, Edward L. Ionides, and Aaron A. King. Time series analysis via mechanistic models. *The Annals of Applied Statistics*, pages 319–348, 2009. URL https://www.jstor.org/stable/30244243. Publisher: JSTOR.

Tom Britton. Stochastic epidemic models: A survey. *Mathematical Biosciences*, 225(1): 24–35, 2010. ISSN 00255564. doi:10.1016/j.mbs.2010.01.006. URL http://dx.doi.org/10.1016/j.mbs.2010.01.006. Publisher: Elsevier Inc. _eprint: 0910.4443.

Tom Britton, Theodore Kypraios, and Philip D. O'Neill. Inference for Epidemics with Three Levels of Mixing: Methodology and Application to a Measles Outbreak. *Scandinavian Journal of Statistics*, 38(3):578–599, 2011. ISSN 03036898. doi:10.1111/j.1467-9469.2010.00726.x.

Tom Britton, Frank Ball, and Pieter Trapman. A mathematical model reveals the influence of population heterogeneity on herd immunity to SARS-CoV-2. *Science*, 369(6505):846–849, 2020. ISSN 10959203. doi:10.1126/science.abc6810.

Martha H. Brookes, R.W. Stark, and Robert W. Campbell, editors. *The Douglas-fir Tussock Moth: A Synthesis*, volume 1585 of *Technical Bulletin*. U.S. Forest Service Scicence and Education Agency, 1978.

Gregory Brown, Crystal Kelehear, and Richard Shine. The early toad gets the worm: Cane toads at an invasion front benefit from higher prey availability. *The Journal of animal ecology*, 82, January 2013a. doi:10.1111/1365-2656.12048.

V. L. Brown, J. M. Drake, D. E. Stallknecht, J. D. Brown, K. Pedersen, and P. Rohani. Dissecting a wildlife disease hotspot: the impact of multiple host species, environmental transmission and seasonality in migration, breeding and mortality. *Journal of The Royal Society Interface*, 10(79):20120804, February 2013b. ISSN 1742-5689, 1742-5662. doi:10.1098/rsif.2012.0804. URL https://royalsocietypublishing.org/doi/10.1098/rsif.2012.0804.

Olivia J. Burton, Ben L. Phillips, and Justin M. J. Travis. Trade-offs and the evolution of life-histories during range expansion. *Ecology Letters*, 13(10):1210–1220, October 2010. ISSN 1461-0248. doi:10.1111/j.1461-0248.2010.01505.x.

Oihana Cabodevilla, Itxaso Ibañez, Oihane Simón, Rosa Murillo, Primitivo Caballero, and Trevor Williams. Occlusion body pathogenicity, virulence and productivity traits vary with transmission strategy in a nucleopolyhedrovirus. *Biological Control*, 56(2):184–192, February 2011. ISSN 1049-9644. doi:10.1016/j.biocontrol.2010.10.007. URL https://www.sciencedirect.com/science/article/pii/S1049964410002240.

Yang Cao, Daniel T. Gillespie, and Linda R. Petzold. Efficient step size selection for the tau-leaping simulation method. *Journal of Chemical Physics*, 124(4), 2006. ISSN 00219606. doi:10.1063/1.2159468.

Yang Cao, Daniel T. Gillespie, and Linda R. Petzold. Adaptive explicit-implicit tau-leaping method with automatic tau selection. *Journal of Chemical Physics*, 126(22), 2007. ISSN 00219606. doi:10.1063/1.2745299.

Jérôme Chave. The problem of pattern and scale in ecology: what have we learned in 20 years? *Ecology Letters*, 16(s1):4–16, 2013. ISSN 1461-0248. doi:10.1111/ele.12048. URL https://onlinelibrary.wiley.com/doi/abs/10.1111/ele.12048. _eprint: https://onlinelibrary.wiley.com/doi/pdf/10.1111/ele.12048.

Song Xi Chen. Beta kernel estimators for density functions. *Computational Statistics and Data Analysis*, 31(2):131–145, 1999. ISSN 01679473. doi:10.1016/S0167-9473(99)00010-9.

Peter Chesson. Mechanisms of Maintenance of Species Diversity. *Annual Review of Ecology, Evolution, and Systematics*, 31(Volume 31, 2000):343–366, November 2000. ISSN 1543-592X, 1545-2069. doi:10.1146/annurev.ecolsys.31.1.343. URL https://www.annualreviews.org/content/journals/10.1146/annurev.ecolsys.31.1.343. Publisher: Annual Reviews.

Peter L. Chesson and William W. Murdoch. Aggregation of Risk: Relationships Among Host-Parasitoid Models. *The American Naturalist*, 127(5):696–715, May 1986. ISSN 0003-0147. doi:10.1086/284514. URL https://www.journals.uchicago.edu/doi/abs/10.1086/284514. Publisher: The University of Chicago Press.

Sarah Cobey. Modeling infectious disease dynamics. *Science*, 368(6492):713–714, May 2020. ISSN 0036-8075, 1095-9203. doi:10.1126/science.abb5659. URL https://www.science.org/doi/10.1126/science.abb5659.

Tom W. Coleman, Michael I. Jones, Beatrice Courtial, Andrew D. Graves, Meghan Woods, Alain Roques, and Steven J. Seybold. Impact of the first recorded outbreak of the Douglas-fir tussock moth, Orgyia pseudotsugata, in southern California and the extent of its distribution in the Pacific Southwest region. *Forest Ecology and Management. 329: 295-305*, 329:295–305, 2014. doi:10.1016/j.foreco.2014.06.027. URL https://research.fs.usda.gov/treesearch/49342.

Jenny S. Cory and Kelli Hoover. Plant-mediated effects in insect–pathogen interactions. *Trends in ecology & evolution*, 21(5):278–286, 2006. URL https://www.cell.com/AJHG/fulltext/S0169-5347(06)00057-7. Publisher: Elsevier.

Jenny S. Cory and Judith H. Myers. The Ecology and Evolution of Insect Baculoviruses. *Annual Review of Ecology, Evolution, and Systematics*, 34(1):239–272, November 2003. ISSN 1543-592X, 1545-2069. doi:10.1146/annurev.ecolsys.34.011802.132402. URL https://www.annualreviews.org/doi/10.1146/annurev.ecolsys.34.011802.132402.

Jenny S. Cory, Bernadette M. Green, Robin K. Paul, and Frances Hunter-Fujita. Genotypic and phenotypic diversity of a baculovirus population within an individual insect host. *Journal of Invertebrate Pathology*, 89(2):101–111, 2005. URL https://www.sciencedirect.com/science/article/pii/S0022201105000595. Publisher: Elsevier.

Philip H. Crowley. Dispersal and the Stability of Predator-Prey Interactions. *The American Naturalist*, 118(5):673–701, November 1981. ISSN 0003-0147. doi:10.1086/283861. URL

https://www.journals.uchicago.edu/doi/abs/10.1086/283861. Publisher: The University of Chicago Press.

R.I. Cukier, C.M. Fortuin, K.E. Shuler, A.G. Petschek, and J.H. Schaibly. Study of the sensitivity of coupled reaction systems to uncertainties in rate coefficients. I Theory. *Journal of Chemical Physics*, 59(8):3873–3878, 1973. doi:10.1063/1.1680571.

Jacob Curran-Sebastian, Lorenzo Pellis, Ian Hall, and Thomas House. Calculation of Epidemic First Passage and Peak Time Probability Distributions, January 2023. URL http://arxiv.org/abs/2301.07058. arXiv:2301.07058 [math, q-bio].

Maxime Dahirel, Aline Bertin, Marjorie Haond, Aurélie Blin, Vincent Calcagno, Simon Fellous, Ludovic Mailleret, Thibaut Malausa, and Elodie Vercken. Shifts from pulled to pushed range expansions caused by reduction of landscape connectivity. *PEER COMMUNITY IN EVOLUTIONARY BIOLOGY*.

Maxime Dahirel, Chloé Guicharnaud, and Elodie Vercken. Individual variation in dispersal, and its sources, shape the fate of pushed vs. pulled range expansions, January 2022. URL http://biorxiv.org/lookup/doi/10.1101/2022.01.12.476009.

D. L. Dahlsten, R. F. Luck, E. I. Schlinger, J. M. Wenz, and W. A. Copper. PARASITOIDS AND PREDATORS OF THE DOUGLAS-FIR TUSSOCK MOTH,. *The Canadian Entomologist*, 109(5):727–746, May 1977. ISSN 1918-3240, 0008-347X. doi:10.4039/Ent109727-5. URL https://www.cambridge.org/core/journals/canadian-entomologist/article/abs/parasitoids-and-predators-of-the-douglasfir-tussock-moth-orgyia-pseudotsugata-lepidoptera-lymantridae-in-low-to-moderate-populations-in-central-california1/BC2B85243D3B5B05C28118348364C081.

Vincent D'Amico and Joseph S. Elkinton. Rainfall effects on transmission of gypsy moth (Lepidoptera: Lymantriidae) nuclear polyhedrosis virus. *Environmental Entomology*, 24 (5):1144–1149, 1995. URL https://academic.oup.com/ee/article-abstract/24/5/1144/2480838. Publisher: Oxford University Press Oxford, UK.

Francisco De Castro and Benjamin Bolker. Mechanisms of disease-induced extinction. *Ecology Letters*, 8(1):117–126, January 2005. ISSN 1461-023X, 1461-0248. doi:10.1111/j.1461-0248.2004.00693.x. URL https://onlinelibrary.wiley.com/doi/10.1111/j.1461-0248.2004.00693.x.

Donald L. DeAngelis and Volker Grimm. Individual-based models in ecology after four decades. *F1000Prime Reports*, 6:39, June 2014. ISSN 2051-7599. doi:10.12703/P6-39. URL https://www.ncbi.nlm.nih.gov/pmc/articles/PMC4047944/.

Lorna E. Deeth and Rob Deardon. Spatial data aggregation for spatio-temporal individual-level models of infectious disease transmission. *Spatial and Spatio-temporal Epidemiology*, 17:95–104, 2016. ISSN 18775853. doi:10.1016/j.sste.2016.04.013. URL http://dx.doi.org/10.1016/j.sste.2016.04.013. Publisher: Elsevier Ltd.

Maxime Deforet, Carlos Carmona-Fontaine, Kirill S. Korolev, and Joao B. Xavier. Evolution at the Edge of Expanding Populations. *The American Naturalist*, 194(3):291–305, September 2019. ISSN 0003-0147. doi:10.1086/704594. URL https://www.journals.uchicago.edu/doi/full/10.1086/704594. Publisher: The University of Chicago Press.

Brian Dennis, William P. Kemp, and Roy C. Beckwith. Stochastic model of insect phenology: estimation and testing. *Environmental Entomology*, 15(3):540–546, 1986. URL https://academic.oup.com/ee/article-abstract/15/3/540/2480371. Publisher: Oxford University Press Oxford, UK.

Sarah E. Diamond. Contemporary climate-driven range shifts: Putting evolution back on the table. *Functional Ecology*, 32(7):1652–1665, July 2018. ISSN 0269-8463, 1365-2435. doi:10.1111/1365-2435.13095. URL https://besjournals.onlinelibrary.wiley.com/doi/10.1111/1365-2435.13095.

Katherine P. Dixon. *Interacting Effects of Host-Pathogen Ecology and Evolution and Climate Change on Outbreaks of a Forest Pest Insect*. PhD thesis, University of Chicago, August 2024.

David W. Dowdy, Jonathan E. Golub, Richard E. Chaisson, and Valeria Saraceni. Heterogeneity in tuberculosis transmission and the role of geographic hotspots in propagating epidemics. *Proceedings of the National Academy of Sciences*, 109(24):9557–9562, June 2012. ISSN 0027-8424, 1091-6490. doi:10.1073/pnas.1203517109. URL https://pnas.org/doi/full/10.1073/pnas.1203517109.

Eric Dumonteil, Satya N. Majumdar, Alberto Rosso, and Andrea Zoia. Spatial extent of an outbreak in animal epidemics. *Proceedings of the National Academy of Sciences of the United States of America*, 110(11):4239–4244, 2013. ISSN 00278424. doi:10.1073/pnas.1213237110.

R. Durrett and S. Levin. The Importance of Being Discrete (and Spatial). *Theoretical Population Biology*, 46(3):363–394, December 1994. ISSN 0040-5809. doi:10.1006/tpbi.1994.1032. URL https://www.sciencedirect.com/science/article/pii/S004058098471032X.

Greg Dwyer. On the Spatial Spread of Insect Pathogens: Theory and Experiment. *Ecology*, 73(2):479–494, April 1992. ISSN 0012-9658, 1939-9170. doi:10.2307/1940754. URL https://esajournals.onlinelibrary.wiley.com/doi/10.2307/1940754.

Greg Dwyer and Joseph S. Elkinton. Host Dispersal and the Spatial Spread of Insect Pathogens. *Ecology*, 76(4):1262–1275, June 1995. ISSN 0012-9658, 1939-9170. doi:10.2307/1940933. URL https://esajournals.onlinelibrary.wiley.com/doi/10.2307/1940933.

Greg Dwyer, Jonathan Dushoff, Joseph S Elkinton, and Simon A Levin. Pathogen-Driven Outbreaks in Forest Defoliators Revisited: Building Models from Experimental Data.

Greg Dwyer, Jonathan Dushoff, Joseph S. Elkinton, and Simon A. Levin. Pathogen-Driven Outbreaks in Forest Defoliators Revisited: Building Models from Experimental Data. *The American Naturalist*, 156(2):105–120, August 2000. ISSN 0003-0147, 1537-5323. doi:10.1086/303379. URL https://www.journals.uchicago.edu/doi/10.1086/303379.

Greg Dwyer, Jonathan Dushoff, and Susan Harrell Yee. The combined effects of pathogens and predators on insect outbreaks. *Nature*, 430(6997):341–345, July 2004. ISSN 0028-0836, 1476-4687. doi:10.1038/nature02569. URL https://www.nature.com/articles/nature02569.

Greg Dwyer, Jeffrey Firestone, and T. Emiko Stevens. Should models of disease dynamics in herbivorous insects include the effects of variability in host-plant foliage quality? *The American Naturalist*, 165(1):16–31, January 2005. ISSN 1537-5323. doi:10.1086/426603.

Greg Dwyer, Joseph R. Mihaljevic, and Vanja Dukic. Can Eco-Evo Theory Explain Population Cycles in the Field? *The American Naturalist*, 199(1):108–125, January 2022. ISSN 0003-0147, 1537-5323. doi:10.1086/717178. URL https://www.journals.uchicago.edu/doi/10.1086/717178.

Ken T.D. Eames and Matt J. Keeling. Modeling dynamic and network heterogeneities in the spread of sexually transmitted diseases. *Proceedings of the National Academy of Sciences of the United States of America*, 99(20):13330–13335, 2002. ISSN 00278424. doi:10.1073/pnas.202244299.

Christopher Edmonds, Anita Lillie, and L Cavalli-Sforza. Mutations arising in the wave front of an expanding population. *Proceedings of the National Academy of Sciences of the United States of America*, 101:975–9, February 2004. doi:10.1073/pnas.0308064100.

Bret D. Elderd and Greg Dwyer. Using insect baculoviruses to understand how population structure affects disease spread. In Andy Fenton, Dan Tompkins, and Kenneth Wilson, editors, *Wildlife Disease Ecology: Linking Theory to Data and Application*, Ecological Reviews, pages 225–261. Cambridge University Press, Cambridge, 2019. ISBN 978-1-107-13656-4. doi:10.1017/9781316479964.008. URL https://www.cambridge.org/core/books/wildlife-disease-ecology/using-insect-baculoviruses-to-understand-how-population-structure-affects-disease-spread/E379DA1CEDD208B9CBCBCF98AC021AFF.

Bret D. Elderd, Nicole Mideo, and Meghan A. Duffy. Looking across Scales in Disease Ecology and Evolution. *The American Naturalist*, 199(1):51–58, January 2022. ISSN 0003-0147. doi:10.1086/717176. URL https://www.journals.uchicago.edu/doi/abs/10.1086/717176. Publisher: The University of Chicago Press.

Bret D. Elderd, Jonathan Dushoff, and Greg Dwyer. Host-Pathogen Interactions, Insect Outbreaks, and Natural Selection for Disease Resistance. *The American Naturalist*, 172 (6):829–842, December 2008. ISSN 0003-0147, 1537-5323. doi:10.1086/592403. URL https://www.journals.uchicago.edu/doi/10.1086/592403.

Chellafe Ensoy, Marc Aerts, Sarah Welby, Yves Van der Stede, and Christel Faes. A Dynamic Spatio-Temporal Model to Investigate the Effect of Cattle Movements on the Spread of Bluetongue BTV-8 in Belgium. *PLOS ONE*, 8(11):e78591, November 2013. ISSN 1932-6203. doi:10.1371/journal.pone.0078591. URL `https://journals.plos.org/plosone/article?id=10.1371/journal.pone.0078591`. Publisher: Public Library of Science.

Philip Erm and Ben L Phillips. Evolution Transforms Pushed Waves into Pulled Waves.

Philip Erm and Ben L. Phillips. Evolution Transforms Pushed Waves into Pulled Waves. *The American Naturalist*, March 2020. ISSN 0003-0147. doi:10.1086/707324. URL `https://www.journals.uchicago.edu/doi/10.1086/707324`. Publisher: The University of Chicago PressChicago, IL.

Tamara L Fetters and Joel W McGlothlin. Life histories and invasions: accelerated laying rate and incubation time in an invasive lizard, Anolis sagrei. *Biological Journal of the Linnean Society*, 122(3):635–642, October 2017. ISSN 0024-4066, 1095-8312. doi:10.1093/biolinnean/blx102. URL `http://academic.oup.com/biolinnean/article/122/3/635/4160407/Life-histories-and-invasions-accelerated-laying`.

Arietta E. Fleming-Davies, Vanja Dukic, Viggo Andreasen, and Greg Dwyer. Effects of host heterogeneity on pathogen diversity and evolution. *Ecology Letters*, 18(11):1252–1261, November 2015. ISSN 1461-023X, 1461-0248. doi:10.1111/ele.12506. URL `https://onlinelibrary.wiley.com/doi/10.1111/ele.12506`.

A. C. Fowler. Atto-Foxes and Other Minutiae. *Bulletin of Mathematical Biology*, 83(10):104, 2021. ISSN 0092-8240. doi:10.1007/s11538-021-00936-x. URL `https://www.ncbi.nlm.nih.gov/pmc/articles/PMC8408093/`.

Emanuel A. Fronhofer and Florian Altermatt. Eco-evolutionary feedbacks during experimental range expansions. *Nature Communications*, 6(1):6844, April 2015. ISSN 2041-1723. doi:10.1038/ncomms7844. URL `https://www.nature.com/articles/ncomms7844`. Publisher: Nature Publishing Group.

Sebastian Funk and Aaron A. King. Choices and trade-offs in inference with infectious disease models. *Epidemics*, 30(March 2019):100383, 2020. ISSN 18780067. doi:10.1016/j.epidem.2019.100383. URL `https://doi.org/10.1016/j.epidem.2019.100383`. Publisher: Elsevier.

John R. Giles, Elisabeth Zu Erbach-Schoenberg, Andrew J. Tatem, Lauren Gardner, Ottar N. Bjørnstad, C. J. E. Metcalf, and Amy Wesolowski. The duration of travel impacts the spatial dynamics of infectious diseases. *Proceedings of the National Academy of Sciences of the United States of America*, 117(36):22572–22579, September 2020. ISSN 1091-6490. doi:10.1073/pnas.1922663117.

Daniel T Gillespie. Exact stochastic simulation of coupled chemical reactions. *The Journal of Physical Chemistry*, 81(25):2340–2361, December 1977. ISSN 0022-3654.

doi:10.1021/j100540a008. URL https://doi.org/10.1021/j100540a008. Publisher: American Chemical Society.

Julia R. Gog and Bryan T. Grenfell. Dynamics and selection of many-strain pathogens. *Proceedings of the National Academy of Sciences*, 99(26):17209–17214, December 2002. doi:10.1073/pnas.252512799. URL https://www.pnas.org/doi/full/10.1073/pnas.252512799. Publisher: Proceedings of the National Academy of Sciences.

Ana R. Gouveia, Ottar N. Bjørnstad, and Emil Tkadlec. Dissecting geographic variation in population synchrony using the common vole in central Europe as a test bed. *Ecology and Evolution*, 6(1):212–218, January 2016. ISSN 2045-7758, 2045-7758. doi:10.1002/ece3.1863. URL https://onlinelibrary.wiley.com/doi/10.1002/ece3.1863.

B. T. Grenfell, O. N. Bjørnstad, and J. Kappey. Travelling waves and spatial hierarchies in measles epidemics. *Nature*, 414(6865):716–723, December 2001. ISSN 0028-0836. doi:10.1038/414716a.

Bryan T. Grenfell, Oliver G. Pybus, Julia R. Gog, James L. N. Wood, Janet M. Daly, Jenny A. Mumford, and Edward C. Holmes. Unifying the Epidemiological and Evolutionary Dynamics of Pathogens. *Science*, 303(5656):327–332, January 2004. ISSN 0036-8075, 1095-9203. doi:10.1126/science.1090727. URL https://www.science.org/doi/10.1126/science.1090727.

S. Gupta, N. Ferguson, and R. Anderson. Chaos, persistence, and evolution of strain structure in antigenically diverse infectious agents. *Science (New York, N.Y.)*, 280(5365): 912–915, May 1998. ISSN 0036-8075. doi:10.1126/science.280.5365.912.

Samniqueka J. Halsey and James R. Miller. A spatial agent-based model of the disease vector Ixodes scapularis to explore host-tick associations. *Ecological Modelling*, 387(August):96–106, 2018. ISSN 03043800. doi:10.1016/j.ecolmodel.2018.09.005. URL https://doi.org/10.1016/j.ecolmodel.2018.09.005. Publisher: Elsevier.

Ilkka Hanski. A practical model of metapopulation dynamics. *Journal of animal ecology*, pages 151–162, 1994. URL https://www.jstor.org/stable/5591. Publisher: JSTOR.

Ilkka Hanski and Otso Ovaskainen. The metapopulation capacity of a fragmented landscape. *Nature*, 404(6779):755–758, 2000. URL https://www.nature.com/articles/35008063. Publisher: Nature Publishing Group UK London.

Ilkka Hanski and Daniel Simberloff. The metapopulation approach, its history, conceptual domain, and application to conservation. *Metapopulation biology*, pages 5–26, 1997. URL https://www.sciencedirect.com/science/article/pii/B9780123234452500031. Publisher: Elsevier.

Vinyas Harish, Felipe J. Colón-González, Filipe R. R. Moreira, Rory Gibb, Moritz U. G. Kraemer, Megan Davis, Robert C. Reiner, David M. Pigott, T. Alex Perkins, Daniel J. Weiss, Isaac I. Bogoch, Gonzalo Vazquez-Prokopec, Pablo Manrique Saide, Gerson L.

Barbosa, Ester C. Sabino, Kamran Khan, Nuno R. Faria, Simon I. Hay, Fabián Correa-Morales, Francisco Chiaravalloti-Neto, and Oliver J. Brady. Human movement and environmental barriers shape the emergence of dengue. *Nature Communications*, 15 (1):4205, May 2024. ISSN 2041-1723. doi:10.1038/s41467-024-48465-0. URL https://www.nature.com/articles/s41467-024-48465-0. Publisher: Nature Publishing Group.

Daihai He, Edward L. Ionides, and Aaron A. King. Plug-and-play inference for disease dynamics: measles in large and small populations as a case study. *Journal of The Royal Society Interface*, 7(43):271–283, February 2010. ISSN 1742-5689, 1742-5662. doi:10.1098/rsif.2009.0151. URL https://royalsocietypublishing.org/doi/10.1098/rsif.2009.0151.

J. K. Hill, C. D. Thomas, and B. Huntley. Climate and habitat availability determine 20th century changes in a butterfly's range margin. *PROCEEDINGS OF THE ROYAL SOCIETY B-BIOLOGICAL SCIENCES*, 266(1425):1197–1206, June 1999. ISSN 0962-8452. doi:10.1098/rspb.1999.0763. URL https://royalsocietypublishing.org/doi/10.1098/rspb.1999.0763. Num Pages: 10 Place: London Publisher: Royal Soc Web of Science ID: WOS:000081155500001.

A. I. Hudson, A. E. Fleming-Davies, D. J. Páez, and G. Dwyer. Genotype-by-genotype interactions between an insect and its pathogen. *Journal of Evolutionary Biology*, 29(12): 2480–2490, December 2016. ISSN 1010-061X, 1420-9101. doi:10.1111/jeb.12977. URL https://academic.oup.com/jeb/article/29/12/2480-2490/7381400.

Peter J. Hudson, Annapaola Rizzoli, Bryan T. Grenfell, Hans Heesterbeek, and Andy P. Dobson. *The ecology of wildlife diseases*, volume 501. Oxford University Press Oxford, 2002. URL https://www.researchgate.net/profile/Annapaola-Rizzoli/publication/375275449_The_Ecology_of_Wildlife_Diseases/links/02e7e517a5c62dcc2f000000/The-Ecology-of-Wildlife-Diseases.pdf.

Josie S. Hughes, Christina A. Cobbold, Kyle Haynes, and Greg Dwyer. Effects of Forest Spatial Structure on Insect Outbreaks: Insights from a Host-Parasitoid Model. *The American Naturalist*, 185(5):E130–E152, May 2015. ISSN 0003-0147, 1537-5323. doi:10.1086/680860. URL https://www.journals.uchicago.edu/doi/10.1086/680860.

Kenneth M. Hughes and R. B. Addison. Two nuclear polyhedrosis viruses of the Douglas-fir tussock moth. *Journal of Invertebrate Pathology*, 16(2):196–204, September 1970. ISSN 0022-2011. doi:10.1016/0022-2011(70)90060-1. URL https://www.sciencedirect.com/science/article/pii/0022201170900601.

Alison F. Hunter. Ecology, life history, and phylogeny of outbreak and nonoutbreak species. *Population dynamics: new approaches and synthesis*, pages 41–64, 1995. Publisher: Academic Press San Diego.

Michael A. Irvine and T. Déirdre Hollingsworth. Kernel-density estimation and approximate Bayesian computation for flexible epidemiological model fitting in Python. *Epidemics*, 25 (May 2018):80–88, 2018. ISSN 18780067. doi:10.1016/j.epidem.2018.05.009. URL https://doi.org/10.1016/j.epidem.2018.05.009. Publisher: Elsevier.

Chris P. Jewell, Theodore Kypraios, Peter Neal, and Gareth O. Roberts. Bayesian analysis for emerging infectious diseases. *Bayesian Analysis*, 4(3):465–498, 2009. ISSN 19360975. doi:10.1214/09-BA417.

Rowland R. Kao, Darren M. Green, Jethro Johnson, and Istvan Z. Kiss. Disease dynamics over very different time-scales: Foot-and-mouth disease and scrapie on the network of livestock movements in the UK. *Journal of the Royal Society Interface*, 4(16):907–916, 2007. ISSN 17425689. doi:10.1098/rsif.2007.1129.

Matt J. Keeling and Pejman Rohani. *Modeling Infectious Diseases in Humans and Animals*. Princeton University Press, 2008. ISBN 978-0-691-11617-4. doi:10.2307/j.ctvcm4gk0. URL https://www.jstor.org/stable/j.ctvcm4gk0.

David A. Kennedy and Greg Dwyer. Effects of multiple sources of genetic drift on pathogen variation within hosts. *PLoS Biology*, 16(3):1–17, 2018. ISSN 15457885. doi:10.1371/journal.pbio.2004444. ISBN: 1111111111.

Aline A. de Koeijer, Thomas J. Hagenaars, Jeroen P. G. van Leuken, Arno N. Swart, and Gert Jan Boender. Spatial transmission risk during the 2007-2010 Q fever epidemic in The Netherlands: Analysis of the farm-to-farm and farm-to-resident transmission. *PLOS ONE*, 15(2):e0227491, February 2020. ISSN 1932-6203. doi:10.1371/journal.pone.0227491. URL https://journals.plos.org/plosone/article?id=10.1371/journal.pone.0227491. Publisher: Public Library of Science.

Jason J. Kolbe, Richard E. Glor, Lourdes Rodríguez Schettino, Ada Chamizo Lara, Allan Larson, and Jonathan B. Losos. Genetic variation increases during biological invasion by a Cuban lizard. *Nature*, 431(7005):177–181, September 2004. ISSN 1476-4687. doi:10.1038/nature02807. URL https://www.nature.com/articles/nature02807. Publisher: Nature Publishing Group.

Mark Kot, Mark A. Lewis, and P. Van Den Driessche. Dispersal Data and the Spread of Invading Organisms. *Ecology*, 77(7):2027–2042, October 1996. ISSN 0012-9658, 1939-9170. doi:10.2307/2265698. URL https://esajournals.onlinelibrary.wiley.com/doi/10.2307/2265698.

Steven P. Lalley. Spatial epidemics: Critical behavior in one dimension. *Probability Theory and Related Fields*, 144(3-4):429–469, 2009. ISSN 01788051. doi:10.1007/s00440-008-0151-0. _eprint: 0701698.

Russell Lande. Genetics and Demography in Biological Conservation. *Science*, 241(4872): 1455–1460, September 1988. doi:10.1126/science.3420403. URL https://www.science.

org/doi/10.1126/science.3420403. Publisher: American Association for the Advancement of Science.

Kelly E. Lane-deGraaf, Ryan C. Kennedy, SM M.N. Arifin, Gregory R. Madey, Agustin Fuentes, and Hope Hollocher. A test of agent-based models as a tool for predicting patterns of pathogen transmission in complex landscapes. *BMC Ecology*, 13, 2013. ISSN 14726785. doi:10.1186/1472-6785-13-35.

K.P Lee, J.S Cory, K Wilson, D Raubenheimer, and S.J Simpson. Flexible diet choice offsets protein costs of pathogen resistance in a caterpillar. *Proceedings of the Royal Society B: Biological Sciences*, 273(1588):823–829, April 2006. ISSN 0962-8452, 1471-2954. doi:10.1098/rspb.2005.3385. URL https://royalsocietypublishing.org/doi/10.1098/rspb.2005.3385.

Phenyo E. Lekone and Bärbel F. Finkenstädt. Statistical inference in a stochastic epidemic SEIR model with control intervention: Ebola as a case study. *Biometrics*, 62(4):1170–1177, 2006. ISSN 15410420. doi:10.1111/j.1541-0420.2006.00609.x.

Justin Lessler, Andrew S. Azman, Heather S. McKay, and Sean M. Moore. What is a Hotspot Anyway? *The American Journal of Tropical Medicine and Hygiene*, 96(6):1270–1273, June 2017. ISSN 0002-9637. doi:10.4269/ajtmh.16-0427. URL https://www.ncbi.nlm.nih.gov/pmc/articles/PMC5462559/.

M. R. Leung and M. Kot. Models for the spread of white pine blister rust. *Journal of Theoretical Biology*, 382:328–336, October 2015. ISSN 0022-5193. doi:10.1016/j.jtbi.2015.07.018. URL https://www.sciencedirect.com/science/article/pii/S0022519315003550.

Simon A. Levin. The Problem of Pattern and Scale in Ecology: The Robert H. MacArthur Award Lecture. *Ecology*, 73(6):1943–1967, 1992. ISSN 1939-9170. doi:10.2307/1941447. URL https://onlinelibrary.wiley.com/doi/abs/10.2307/1941447. _eprint: https://onlinelibrary.wiley.com/doi/pdf/10.2307/1941447.

Jana Lipková, Georgios Arampatzis, Philippe Chatelain, Bjoern Menze, and Petros Koumoutsakos. S-Leaping: An Adaptive, Accelerated Stochastic Simulation Algorithm, Bridging Tau -Leaping and R-Leaping. *Bulletin of Mathematical Biology*, 81(8):3074–3096, 2019. ISSN 15229602. doi:10.1007/s11538-018-0464-9. _eprint: 1802.00296.

Karen R. Lips, Forrest Brem, Roberto Brenes, John D. Reeve, Ross A. Alford, Jamie Voyles, Cynthia Carey, Lauren Livo, Allan P. Pessier, and James P. Collins. Emerging infectious disease and the loss of biodiversity in a Neotropical amphibian community. *Proceedings of the National Academy of Sciences*, 103(9):3165–3170, February 2006. ISSN 0027-8424, 1091-6490. doi:10.1073/pnas.0506889103. URL https://pnas.org/doi/full/10.1073/pnas.0506889103.

Benjamin R. Liu and Mark Kot. Accelerating invasions and the asymptotics of fat-tailed dispersal. *Journal of Theoretical Biology*, 471:22–41, June 2019. ISSN 00225193.

doi:10.1016/j.jtbi.2019.03.016. URL https://linkinghub.elsevier.com/retrieve/pii/S0022519319301237.

Jiawei Liu, Colin Kyle, Jiali Wang, Rao Kotamarthi, William Koval, and Greg Dwyer. Climate-Change Driven Decline of an Insect Pathogen Increases the Risk of Defoliation by a Forest Pest Insect, November 2023. URL https://www.biorxiv.org/content/10.1101/2023.11.01.564627v1. Pages: 2023.11.01.564627 Section: New Results.

A. L. Lloyd. Destabilization of epidemic models with the inclusion of realistic distributions of infectious periods. *Proceedings of the Royal Society of London. Series B: Biological Sciences*, 268(1470):985–993, May 2001. ISSN 0962-8452, 1471-2954. doi:10.1098/rspb.2001.1599. URL https://royalsocietypublishing.org/doi/10.1098/rspb.2001.1599.

J. O. Lloyd-Smith, S. J. Schreiber, P. E. Kopp, and W. M. Getz. Superspreading and the effect of individual variation on disease emergence. *Nature*, 438(7066):355–359, November 2005a. ISSN 1476-4687. doi:10.1038/nature04153. URL https://www.nature.com/articles/nature04153. Number: 7066 Publisher: Nature Publishing Group.

James O. Lloyd-Smith, Paul C. Cross, Cheryl J. Briggs, Matt Daugherty, Wayne M. Getz, John Latto, Maria S. Sanchez, Adam B. Smith, and Andrea Swei. Should we expect population thresholds for wildlife disease? *Trends in Ecology & Evolution*, 20(9):511–519, September 2005b. ISSN 0169-5347. doi:10.1016/j.tree.2005.07.004. URL https://www.sciencedirect.com/science/article/pii/S0169534705002077.

Claude Lobry and Tewfik Sari. Migrations in the Rosenzweig-MacArthur model and the "atto-fox" problem. *Revue Africaine de Recherche en Informatique et Mathématiques Appliquées*, Volume 20 - 2015 - Special issue - Colloquium in Honor of Éric Benoît:95, November 2015. doi:10.46298/arima.1990. URL https://inria.hal.science/hal-01235211.

Ana V. Longo, Karen R. Lips, and Kelly R. Zamudio. Evolutionary ecology of host competence after a chytrid outbreak in a naive amphibian community. *Philosophical Transactions of the Royal Society B: Biological Sciences*, 378(1882):20220130, July 2023. ISSN 0962-8436, 1471-2970. doi:10.1098/rstb.2022.0130. URL https://royalsocietypublishing.org/doi/10.1098/rstb.2022.0130.

Robert H. MacArthur. *Geographical ecology: patterns in the distribution of species*. Princeton University Press, Princeton, N.J, 1972. ISBN 978-0-691-08353-7 978-0-691-02382-3.

Rebecca Mancy, Malavika Rajeev, Ahmed Lugelo, Kirstyn Brunker, Sarah Cleaveland, Elaine A. Ferguson, Karen Hotopp, Rudovick Kazwala, Matthias Magoto, Kristyna Rysava, Daniel T. Haydon, and Katie Hampson. Rabies shows how scale of transmission can enable acute infections to persist at low prevalence. *Science*, 376(6592):512–516, April 2022. doi:10.1126/science.abn0713. URL https://www.science.org/doi/10.1126/science.abn0713. Publisher: American Association for the Advancement of Science.

Richard R. Mason. DEVELOPMENT OF SAMPLING METHODS FOR THE DOUGLAS-FIR TUSSOCK MOTH, HEMEROCAMPA PSEUDOTSUGATA (LEPIDOPTERA: LYMANTRIIDAE). *The Canadian Entomologist*, 102(7):836–845, July 1970. ISSN 1918-3240, 0008-347X. doi:10.4039/Ent102836-7. URL https://www.cambridge.org/core/journals/canadian-entomologist/article/abs/development-of-sampling-methods-for-the-douglasfir-tussock-moth-hemerocampa-pseudotsugata-lepidoptera-lymantriidae/26A638C5973C4641F93F958D3255D079.

Richard R. Mason. Sampling low density populations of the Douglas-fir tussock moth by frequency of occurrence in the lower tree crown, 1977. ISSN: 17401267 Pages: 7–8.

Richard R. Mason. Frequency Sampling to Predict Densities in Sparse Populations of the Douglas-Fir Tussock Moth. *Forest Science*, 33(1):145–156, March 1987. ISSN 0015-749X. doi:10.1093/forestscience/33.1.145. URL https://doi.org/10.1093/forestscience/33.1.145.

Richard R. Mason. Dynamic Behavior of Douglas-Fir Tussock Moth Populations in the Pacific Northwest. *Forest Science*, 42(2):182–191, May 1996. ISSN 0015-749X, 1938-3738. doi:10.1093/forestscience/42.2.182. URL https://academic.oup.com/forestscience/article/42/2/182/4627302.

Richard R. Mason, R. C. Beckwith, and H. Gene Paul. Fecundity Reduction During Collapse of a Douglas-fir Tussock Moth 12 Outbreak in Northeast Oregon 4. *Environmental Entomology*, 6(5):623–626, October 1977. ISSN 0046-225X. doi:10.1093/ee/6.5.623. URL https://doi.org/10.1093/ee/6.5.623.

Richard R. Mason, Boyd E. Wickman, and H. Gene Paul. Radial Growth Response of Douglas-fir and Grand Fir to Larval Densities of the Douglas-fir Tussock Moth and the Western Spruce Budworm. *Forest Science*, 43(2):194–205, May 1997. ISSN 0015-749X, 1938-3738. doi:10.1093/forestscience/43.2.194. URL https://academic.oup.com/forestscience/article/43/2/194/4627346.

Robert A. B. Mason, Julia Cooke, Angela T. Moles, and Michelle R. Leishman. Reproductive output of invasive versus native plants. *Global Ecology and Biogeography*, 17(5):633–640, 2008. ISSN 1466-8238. doi:10.1111/j.1466-8238.2008.00402.x. URL https://onlinelibrary.wiley.com/doi/abs/10.1111/j.1466-8238.2008.00402.x. _eprint: https://onlinelibrary.wiley.com/doi/pdf/10.1111/j.1466-8238.2008.00402.x.

Robert May and Roy Anderson. Population biology of infectious diseases. *Nature*, 280: 455–61, September 1979. doi:10.1038/280455a0.

Lauren McGough and Sarah Cobey. A speed limit on serial strain replacement from original antigenic sin. *Proceedings of the National Academy of Sciences*, 121(25):e2400202121, June 2024. ISSN 0027-8424, 1091-6490. doi:10.1073/pnas.2400202121. URL https://pnas.org/doi/10.1073/pnas.2400202121.

Trevelyan McKinley, Alex R. Cook, and Robert Deardon. Inference in epidemic models without likelihoods. *International Journal of Biostatistics*, 5(1), 2009. ISSN 15574679. doi:10.2202/1557-4679.1171.

Brett A. Melbourne and Alan Hastings. Highly variable spread rates in replicated biological invasions: fundamental limits to predictability. *Science (New York, N.Y.)*, 325(5947): 1536–1539, September 2009. ISSN 1095-9203. doi:10.1126/science.1176138.

Joseph R. Mihaljevic, Carlos M. Polivka, Constance J. Mehmel, Chentong Li, Vanja Dukic, and Greg Dwyer. An Empirical Test of the Role of Small-Scale Transmission in Large-Scale Disease Dynamics. *The American Naturalist*, 195(4):616–635, April 2020. ISSN 0003-0147. doi:10.1086/707457. URL https://www.journals.uchicago.edu/doi/full/10.1086/707457. Publisher: The University of Chicago Press.

Tom E. X. Miller, Amy L. Angert, Carissa D. Brown, Julie A. Lee-Yaw, Mark Lewis, Frithjof Lutscher, Nathan G. Marculis, Brett A. Melbourne, Allison K. Shaw, Marianna Szűcs, Olivia Tabares, Takuji Usui, Christopher Weiss-Lehman, and Jennifer L. Williams. Eco-evolutionary dynamics of range expansion. *Ecology*, 101(10):e03139, October 2020. ISSN 0012-9658, 1939-9170. doi:10.1002/ecy.3139. URL https://esajournals.onlinelibrary.wiley.com/doi/10.1002/ecy.3139.

Rg Mitchell. Dispersal of Early Instars of the Douglas-Fir Tussock Moth Orgyia-Pseudotsugata (mcdunnough) (lepidoptera, Lymantriidae). *ANNALS OF THE ENTOMOLOGICAL SOCIETY OF AMERICA*, 72(2):291–297, 1979. ISSN 0013-8746, 1938-2901. doi:10.1093/aesa/72.2.291. URL https://www.webofscience.com/wos/woscc/summary/b34ce978-3129-49ca-a861-76f57a8125d5-0102183ddc/relevance/1. Num Pages: 7 Place: Cary Publisher: Oxford Univ Press Inc Web of Science ID: WOS:A1979GP80600024.

D. Mollison. Dependence of epidemic and population velocities on basic parameters. *Mathematical Biosciences*, 107(2):255–287, December 1991. ISSN 0025-5564. doi:10.1016/0025-5564(91)90009-8.

Denis Mollison. *Epidemic Models: Their Structure and Relation to Data*. Cambridge University Press, July 1995. ISBN 978-0-521-47536-5. Google-Books-ID: MZRkdfOBylYC.

Ja Moore and Cr Hatch. A Simulation Approach for Predicting the Effect of Douglas-Fir Tussock Moth Defoliation on Juvenile Tree Growth and Stand Dynamics. *FOREST SCIENCE*, 27(4):685–700, 1981. ISSN 0015-749X, 1938-3738. URL https://www.webofscience.com/wos/woscc/full-record/WOS:A1981MY52400007. Num Pages: 16 Place: Cary Publisher: Oxford Univ Press Inc Web of Science ID: WOS:A1981MY52400007.

R. Moss, D. A. Elston, and A. Watson. SPATIAL ASYNCHRONY AND DEMOGRAPHIC TRAVELING WAVES DURING RED GROUSE POPULATION CYCLES. *Ecology*, 81(4):981–989, April 2000. ISSN 0012-9658. doi:10.1890/0012-9658(2000)081[0981:SAADTW]2.0.CO;2. URL http://doi.wiley.com/10.1890/0012-9658(2000)081[0981:SAADTW]2.0.CO;2.

Christopher C. Mundt, Kathryn E. Sackett, LaRae D. Wallace, Christina Cowger, and Joseph P. Dudley. Long-distance dispersal and accelerating waves of disease: empirical relationships. *The American Naturalist*, 173(4):456–466, April 2009. ISSN 1537-5323. doi:10.1086/597220.

J. D. Murray, E. A. Stanley, and D. L. Brown. On the spatial spread of rabies among foxes. *Proceedings of the Royal Society of London. Series B, Biological Sciences*, 229(1255):111–150, November 1986. ISSN 0950-1193. doi:10.1098/rspb.1986.0078.

Judith H. Myers and Jenny S. Cory. Population Cycles in Forest Lepidoptera Revisited. *Annual Review of Ecology, Evolution, and Systematics*, 44(1):565–592, November 2013. ISSN 1543-592X, 1545-2069. doi:10.1146/annurev-ecolsys-110512-135858. URL `https://www.annualreviews.org/doi/10.1146/annurev-ecolsys-110512-135858`.

Judith H. Myers and Jenny S. Cory. Ecology and evolution of pathogens in natural populations of Lepidoptera. *Evolutionary Applications*, 9(1):231–247, November 2015. ISSN 1752-4571. doi:10.1111/eva.12328. URL `https://www.ncbi.nlm.nih.gov/pmc/articles/PMC4780379/`.

Claudia Nassuato, Gert Jan Boender, Phaedra L. Eblé, Loris Alborali, Silvia Bellini, and Thomas J. Hagenaars. Spatial Transmission of Swine Vesicular Disease Virus in the 2006–2007 Epidemic in Lombardy. *PLOS ONE*, 8(5):e62878, May 2013. ISSN 1932-6203. doi:10.1371/journal.pone.0062878. URL `https://journals.plos.org/plosone/article?id=10.1371/journal.pone.0062878`. Publisher: Public Library of Science.

Peter Neal and Thitiya Theparod. The basic reproduction number, R0, in structured populations. *Mathematical Biosciences*, 315, 2019. ISSN 18793134. doi:10.1016/j.mbs.2019.108224. _eprint: 1903.10353.

Michael G. Neubert, Mark Kot, and Mark A. Lewis. Invasion speeds in fluctuating environments. *Proceedings of the Royal Society of London. Series B: Biological Sciences*, 267 (1453):1603–1610, August 2000. ISSN 0962-8452, 1471-2954. doi:10.1098/rspb.2000.1185. URL `https://royalsocietypublishing.org/doi/10.1098/rspb.2000.1185`.

Charles L. Nunn, Peter H. Thrall, and Peter M. Kappeler. Shared resources and disease dynamics in spatially structured populations. *Ecological Modelling*, 272:198–207, 2014. ISSN 03043800. doi:10.1016/j.ecolmodel.2013.10.004. URL `http://dx.doi.org/10.1016/j.ecolmodel.2013.10.004`. Publisher: Elsevier B.V.

Akira Okubo and Simon A. Levin. *Diffusion and Ecological Problems: Modern Perspectives*, volume 14 of *Interdisciplinary Applied Mathematics*. Springer, New York, NY, 2001. ISBN 978-1-4419-3151-1 978-1-4757-4978-6. doi:10.1007/978-1-4757-4978-6. URL `http://link.springer.com/10.1007/978-1-4757-4978-6`.

Isabelle Olivieri, Yannis Michalakis, and Pierre-Henri Gouyon. Metapopulation Genetics and the Evolution of Dispersal. *The American Naturalist*, 146(2):202–228, August 1995.

ISSN 0003-0147. doi:10.1086/285795. URL https://www.journals.uchicago.edu/doi/10.1086/285795. Publisher: The University of Chicago Press.

Philip D. O'Neill, David J. Balding, Niels G. Becker, Mervi Eerola, and Denis Mollison. Analyses of infectious disease data from household outbreaks by Markov chain Monte Carlo methods. *Journal of the Royal Statistical Society. Series C: Applied Statistics*, 49 (4):517–542, 2000. ISSN 00359254. doi:10.1111/1467-9876.00210.

Matthew M. Osmond and Graham Coop. Estimating dispersal rates and locating genetic ancestors with genome-wide genealogies, July 2021. URL https://www.biorxiv.org/content/10.1101/2021.07.13.452277v1. Pages: 2021.07.13.452277 Section: New Results.

I. S. Otvos, J. C. Cunningham, and W. J. Kaupp. Aerial application of two baculoviruses against the western spruce budworm, Choristoneura occidentalis Freeman (Lepidoptera: Tortricidae), in British Columbia. *The Canadian Entomologist*, 121(3):209–217, 1989. URL https://www.cambridge.org/core/journals/canadian-entomologist/article/aerial-application-of-two-baculoviruses-against-the-western-spruce-budworm-choristoneura-occidentalis-freeman-lepidoptera-tortricidae-in-british-columbia/A789877DB0DE8CAFAC6D33F0DAACAE7F. Publisher: Cambridge University Press.

Benjamin J. Parker, Bret D. Elderd, and Greg Dwyer. Host behaviour and exposure risk in an insect–pathogen interaction. *Journal of Animal Ecology*, 79(4):863–870, July 2010. ISSN 0021-8790, 1365-2656. doi:10.1111/j.1365-2656.2010.01690.x. URL https://besjournals.onlinelibrary.wiley.com/doi/10.1111/j.1365-2656.2010.01690.x.

Camille Parmesan and Gary Yohe. A globally coherent fingerprint of climate change impacts across natural systems. *Nature*, 421(6918):37–42, January 2003. ISSN 1476-4687. doi:10.1038/nature01286. URL https://www.nature.com/articles/nature01286. Publisher: Nature Publishing Group.

Mikko Peltonen, Andrew M. Liebhold, Ottar N. Bjørnstad, and David W. Williams. Spatial synchrony in forest insect outbreaks: roles of regional stochasticity and dispersal. *Ecology*, 83(11):3120–3129, November 2002. ISSN 0012-9658. doi:10.1890/0012-9658(2002)083[3120:SSIFIO]2.0.CO;2. URL http://doi.wiley.com/10.1890/0012-9658(2002)083[3120:SSIFIO]2.0.CO;2.

T. Alex Perkins. Evolutionarily Labile Species Interactions and Spatial Spread of Invasive Species. *The American Naturalist*, 179(2):E37–E54, February 2012. ISSN 0003-0147, 1537-5323. doi:10.1086/663682. URL https://www.journals.uchicago.edu/doi/10.1086/663682.

T. Alex Perkins, Benjamin L. Phillips, Marissa L. Baskett, and Alan Hastings. Evolution of dispersal and life history interact to drive accelerating spread of an invasive species. *Ecology Letters*, 16(8):1079–1087, August 2013. ISSN 1461-023X, 1461-0248. doi:10.1111/ele.12136. URL https://onlinelibrary.wiley.com/doi/10.1111/ele.12136.

Sergei V. Petrovskii, Horst Malchow, Frank M. Hilker, and Ezio Venturino. Patterns of Patchy Spread in Deterministic and Stochastic Models of Biological Invasion and Biological Control. *Biological Invasions*, 7(5):771–793, September 2005. ISSN 1387-3547, 1573-1464. doi:10.1007/s10530-005-5217-7. URL http://link.springer.com/10.1007/s10530-005-5217-7.

Ben L. Phillips, Crystal Kelehear, Lígia Pizzatto, Gregory P. Brown, Di Barton, and Richard Shine. Parasites and pathogens lag behind their host during periods of host range advance. *Ecology*, 91(3):872–881, 2010. ISSN 1939-9170. doi:10.1890/09-0530.1. URL https://onlinelibrary.wiley.com/doi/abs/10.1890/09-0530.1. _eprint: https://onlinelibrary.wiley.com/doi/pdf/10.1890/09-0530.1.

Juho Piironen, Markus Paasiniemi, and Aki Vehtari. Projective inference in high-dimensional problems: Prediction and feature selection. *Electronic Journal of Statistics*, 14(1):2155–2197, January 2020. ISSN 1935-7524, 1935-7524. doi:10.1214/20-EJS1711. URL https://projecteuclid.org/journals/electronic-journal-of-statistics/volume-14/issue-1/Projective-inference-in-high-dimensional-problems--Prediction-and-feature/10.1214/20-EJS1711.full. Publisher: Institute of Mathematical Statistics and Bernoulli Society.

David J Páez, Vanja Dukic, Jonathan Dushoff, Arietta Fleming-Davies, and Greg Dwyer. Eco-Evolutionary Theory and Insect Outbreaks. *The American Naturalist*, 189(6):616–629, June 2017. ISSN 1537-5323. doi:10.1086/691537.

Leslie A Real and Roman Biek. Spatial dynamics and genetics of infectious diseases on heterogeneous landscapes. *Journal of The Royal Society Interface*, 4(16):935–948, October 2007. ISSN 1742-5689, 1742-5662. doi:10.1098/rsif.2007.1041. URL https://royalsocietypublishing.org/doi/10.1098/rsif.2007.1041.

Lee A. Rollins, Mark F. Richardson, and Richard Shine. A genetic perspective on rapid evolution in cane toads (Rhinella marina). *Molecular Ecology*, 24(9):2264–2276, 2015. ISSN 1365-294X. doi:10.1111/mec.13184. URL https://onlinelibrary.wiley.com/doi/abs/10.1111/mec.13184. _eprint: https://onlinelibrary.wiley.com/doi/pdf/10.1111/mec.13184.

Sebastian J Schreiber and Noelle G Beckman. Individual variation in dispersal and fecundity increases rates of spatial spread. *AoB PLANTS*, 12(3):plaa001, May 2020. ISSN 2041-2851. doi:10.1093/aobpla/plaa001. URL https://academic.oup.com/aobpla/article/doi/10.1093/aobpla/plaa001/5851646.

United States Forest Service. *The Douglas-fir Tussock Moth: A Synthesis*. Department of Agriculture, Forest Service, 1978. Google-Books-ID: BWEWAAAAYAAJ.

Paul M. Severns, Kathryn E. Sackett, Daniel H. Farber, and Christopher C. Mundt. Consequences of Long-Distance Dispersal for Epidemic Spread: Patterns, Scaling, and Mitigation. *Plant Disease*, 103(2):177–191, February 2019. ISSN 0191-2917, 1943-7692.

doi:10.1094/PDIS-03-18-0505-FE. URL https://apsjournals.apsnet.org/doi/10.1094/PDIS-03-18-0505-FE.

Roy F. Shepherd, Dayle D. Bennett, John W. Dale, Scott Tunnock, Robert E. Dolph, and Ralph W. Thier. EVIDENCE OF SYNCHRONIZED CYCLES IN OUTBREAK PATTERNS OF DOUGLAS-FIR TUSSOCK MOTH, ORGYIA PSEUDOTSUGATA (McDUNNOUGH) (LEPIDOPTERA: LYMANTRIIDAE). *The Memoirs of the Entomological Society of Canada*, 120(S146):107–121, January 1988. ISSN 0071-075X. doi:10.4039/entm120146107-1. URL https://www.cambridge.org/core/journals/memoirs-of-the-entomological-society-of-canada/article/abs/evidence-of-synchronized-cycles-in-outbreak-patterns-of-douglasfir-tussock-moth-orgyia-pseudotsugata-mcdunnough-lepidoptera-lymantriidae/38DEB2566939995A603A652A7FBE756C.

J A Sherratt, M A Lewis, and A C Fowler. Ecological chaos in the wake of invasion. *Proceedings of the National Academy of Sciences*, 92(7):2524–2528, March 1995. ISSN 0027-8424, 1091-6490. doi:10.1073/pnas.92.7.2524. URL https://pnas.org/doi/full/10.1073/pnas.92.7.2524.

J.A. Sherratt. Periodic travelling waves in cyclic predator–prey systems. *Ecology Letters*, 4(1):30–37, January 2001. ISSN 1461-023X, 1461-0248. doi:10.1046/j.1461-0248.2001.00193.x. URL https://onlinelibrary.wiley.com/doi/10.1046/j.1461-0248.2001.00193.x.

Jonathan A Sherratt and Matthew J Smith. Periodic travelling waves in cyclic populations: field studies and reaction–diffusion models. *Journal of The Royal Society Interface*, 5 (22):483–505, May 2008. ISSN 1742-5689, 1742-5662. doi:10.1098/rsif.2007.1327. URL https://royalsocietypublishing.org/doi/10.1098/rsif.2007.1327.

Nanako Shigesada. Spatial distribution of dispersing animals. *Journal of mathematical biology*, 9:85–96, April 1980. doi:10.1007/BF00276037.

Nanako Shigesada and Kohkichi Kawasaki. *Biological Invasions: Theory and Practice*. Oxford University Press, UK, February 1997. ISBN 978-0-19-158982-9.

Giulia Simoni, Federico Reali, Corrado Priami, and Luca Marchetti. Stochastic simulation algorithms for computational systems biology: Exact, approximate, and hybrid methods. *Wiley Interdisciplinary Reviews: Systems Biology and Medicine*, 11(6):1–20, 2019. ISSN 1939005X. doi:10.1002/wsbm.1459.

J. G. Skellam. Random dispersal in theoretical populations. *Biometrika*, 38(1-2):196–218, June 1951. ISSN 0006-3444.

D. Smitley, Leah Bauer, Ann Hajek, F. Sapio, and Richard Humber. Introduction and Establishment of Entomophaga maimaiga, a Fungal Pathogen of Gypsy Moth (Lepidoptera: Lymantriidae) in Michigan. *Environmental Entomology*, 24:1685–1695, December 1995. doi:10.1093/ee/24.6.1685.

A. J. M. Tack, P. H. Thrall, L. G. Barrett, J. J. Burdon, and A.-L. Laine. Variation in infectivity and aggressiveness in space and time in wild host-pathogen systems: causes and consequences. *Journal of Evolutionary Biology*, 25(10):1918–1936, October 2012. ISSN 1420-9101. doi:10.1111/j.1420-9101.2012.02588.x.

Boon-Teong Teoh, Sing-Sin Sam, Kim-Kee Tan, Jefree Johari, Meng-Hooi Shu, Mohammed Bashar Danlami, Juraina Abd-Jamil, NorAziyah MatRahim, Nor Muhammad Mahadi, and Sazaly AbuBakar. Dengue virus type 1 clade replacement in recurring homotypic outbreaks. *BMC Evolutionary Biology*, 13(1):213, December 2013. ISSN 1471-2148. doi:10.1186/1471-2148-13-213. URL `https://bmcevolbiol.biomedcentral.com/articles/10.1186/1471-2148-13-213`.

Julien Thézé, Carlos Lopez-Vaamonde, Jenny S. Cory, and Elisabeth A. Herniou. Biodiversity, Evolution and Ecological Specialization of Baculoviruses: A Treasure Trove for Future Applied Research. *Viruses*, 10(7):366, July 2018. ISSN 1999-4915. doi:10.3390/v10070366.

Huaiyu Tian, Yun Feng, Bram Vrancken, Bernard Cazelles, Hua Tan, Mandev S. Gill, Qiqi Yang, Yidan Li, Weihong Yang, Yuzhen Zhang, Yunzhi Zhang, Philippe Lemey, Oliver G. Pybus, Nils Chr Stenseth, Hailin Zhang, and Simon Dellicour. Transmission dynamics of re-emerging rabies in domestic dogs of rural China. *PLOS Pathogens*, 14(12):e1007392, December 2018. ISSN 1553-7374. doi:10.1371/journal.ppat.1007392. URL `https://journals.plos.org/plospathogens/article?id=10.1371/journal.ppat.1007392`. Publisher: Public Library of Science.

Alexei V. Tkachenko, Sergei Maslov, Ahmed Elbanna, George N. Wong, Zachary J. Weiner, and Nigel Goldenfeld. Time-dependent heterogeneity leads to transient suppression of the COVID-19 epidemic, not herd immunity. *Proceedings of the National Academy of Sciences*, 118(17):e2015972118, April 2021. doi:10.1073/pnas.2015972118. URL `https://www.pnas.org/doi/10.1073/pnas.2015972118`. Publisher: Proceedings of the National Academy of Sciences.

Panayiota Touloupou, Barbel Finkenstadt, Thomas E. Besser, Nigel P. French, and Simon E. F. Spencer. Bayesian inference for multi-strain epidemics with application to Escherichia coli O157: H7 in feedlot cattle. *Annals of Applied Statistics*, 14(4):1925–1944, December 2020. ISSN 1932-6157. doi:10.1214/20-AOAS1366.

Joanne Turner, Roger G. Bowers, and Matthew Baylis. Modelling bluetongue virus transmission between farms using animal and vector movements. *Scientific Reports*, 2(1):319, March 2012. ISSN 2045-2322. doi:10.1038/srep00319. URL `https://www.nature.com/articles/srep00319`. Publisher: Nature Publishing Group.

Carla A. Urquhart and Jennifer L. Williams. Trait correlations and landscape fragmentation jointly alter expansion speed via evolution at the leading edge in simulated range expansions. *Theoretical Ecology*, 14(3):381–394, September 2021. ISSN 1874-1738, 1874-1746. doi:10.1007/s12080-021-00503-z. URL `https://link.springer.com/10.1007/s12080-021-00503-z`.

Gonzalo M. Vazquez-Prokopec, Amy C. Morrison, Valerie Paz-Soldan, Steven T. Stoddard, William Koval, Lance A. Waller, T. Alex Perkins, Alun L. Lloyd, Helvio Astete, and John Elder. Inapparent infections shape the transmission heterogeneity of dengue. *PNAS nexus*, 2(3):pgad024, 2023. URL https://academic.oup.com/pnasnexus/article-abstract/2/3/pgad024/7010769. Publisher: Oxford University Press US.

Aki Vehtari, Andrew Gelman, and Jonah Gabry. Practical Bayesian model evaluation using leave-one-out cross-validation and WAIC. *Statistics and Computing*, 27(5):1413–1432, September 2017. ISSN 1573-1375. doi:10.1007/s11222-016-9696-4. URL https://doi.org/10.1007/s11222-016-9696-4.

Aki Vehtari, Jonah Gabry, Måns Magnusson, Yuling Yao, Paul-Christian Bürkner, Topi Paananen, and Andrew Gelman. loo: Efficient leave-one-out cross-validation and WAIC for Bayesian models, 2024a. URL https://mc-stan.org/loo/.

Aki Vehtari, Daniel Simpson, Andrew Gelman, Yuling Yao, and Jonah Gabry. Pareto Smoothed Importance Sampling, March 2024b. URL http://arxiv.org/abs/1507.02646. arXiv:1507.02646 [stat].

Cécile Viboud, Ottar N. Bjørnstad, David L. Smith, Lone Simonsen, Mark A. Miller, and Bryan T. Grenfell. Synchrony, Waves, and Spatial Hierarchies in the Spread of Influenza. *Science*, 312(5772):447–451, April 2006. ISSN 0036-8075, 1095-9203. doi:10.1126/science.1125237. URL https://www.science.org/doi/10.1126/science.1125237.

Jonathan A. Walter, Lawrence W. Sheppard, Thomas L. Anderson, Jude H. Kastens, Ottar N. Bjørnstad, Andrew M. Liebhold, and Daniel C. Reuman. The geography of spatial synchrony. *Ecology Letters*, 20(7):801–814, July 2017. ISSN 1461-023X, 1461-0248. doi:10.1111/ele.12782. URL https://onlinelibrary.wiley.com/doi/10.1111/ele.12782.

Jacob Weiner and Paul T. Conte. Dispersal and neighborhood effects in an annual plant competition model. *Ecological Modelling*, 13(3):131–147, August 1981. ISSN 0304-3800. doi:10.1016/0304-3800(81)90048-X. URL https://www.sciencedirect.com/science/article/pii/030438008190048X.

Christopher Weiss-Lehman, Ruth A Hufbauer, and Brett A Melbourne. Rapid trait evolution drives increased speed and variance in experimental range expansions. *Nature Communications*, 8(1):14303, January 2017. ISSN 2041-1723. doi:10.1038/ncomms14303. URL https://www.nature.com/articles/ncomms14303.

Lauren A. White, James D. Forester, and Meggan E. Craft. Dynamic, spatial models of parasite transmission in wildlife: Their structure, applications and remaining challenges. *Journal of Animal Ecology*, 87(3):559–580, May 2018. ISSN 0021-8790, 1365-2656. doi:10.1111/1365-2656.12761. URL https://besjournals.onlinelibrary.wiley.com/doi/10.1111/1365-2656.12761.

Holly L. Williams and Imre S Otvos. Genotypic variation and presence of rare genotypes among Douglas-fir tussock moth multicapsid nucleopolyhedrovirus (OpMNPV) isolates in British Columbia. *Journal of Invertebrate Pathology*, 88(3):190–200, 2005. ISSN 00222011. doi:10.1016/j.jip.2005.02.002.

Jennifer L. Williams, Bruce E. Kendall, and Jonathan M. Levine. Rapid evolution accelerates plant population spread in fragmented experimental landscapes. *Science*, 353(6298):482–485, July 2016. ISSN 0036-8075, 1095-9203. doi:10.1126/science.aaf6268. URL https://www.science.org/doi/10.1126/science.aaf6268.

Jennifer L. Williams, Ruth A. Hufbauer, and Tom E. X. Miller. How Evolution Modifies the Variability of Range Expansion. *Trends in Ecology & Evolution*, 34(10):903–913, October 2019. ISSN 0169-5347. doi:10.1016/j.tree.2019.05.012. URL https://www.sciencedirect.com/science/article/pii/S0169534719301648.

M. Williamson. *Biological Invasions*. Springer Science & Business Media, 1996. ISBN 978-0-412-59190-7. Google-Books-ID: eWUdzI6j3V8C.

Kenneth Wilson, Andy Fenton, and Dan Tompkins, editors. *Wildlife Disease Ecology: Linking Theory to Data and Application*. Ecological Reviews. Cambridge University Press, Cambridge, 2019. ISBN 978-1-107-13656-4. doi:10.1017/9781316479964. URL https://www.cambridge.org/core/books/wildlife-disease-ecology/D3750098BDFE4A82175C90C07DED5589.

Luzie U Wingen, James K M Brown, and Michael W Shaw. The Population Genetic Structure of Clonal Organisms Generated by Exponentially Bounded and Fat-Tailed Dispersal. *Genetics*, 177(1):435–448, September 2007. ISSN 1943-2631. doi:10.1534/genetics.107.077206. URL https://academic.oup.com/genetics/article/177/1/435/6062248.

Simon N Wood and Matthew B Thomas. Space, time and persistence of virulent pathogens. *Proceedings of the Royal Society of London. Series B: Biological Sciences*, 263(1371):673–680, June 1996. ISSN 0962-8452, 1471-2954. doi:10.1098/rspb.1996.0101. URL https://royalsocietypublishing.org/doi/10.1098/rspb.1996.0101.

S. A. Woods and J. S. Elkinton. Bimodal patterns of mortality from nuclear polyhedrosis virus in gypsy moth (Lymantria dispar) populations. *Journal of Invertebrate Pathology*, 50(2):151–157, 1987. URL https://www.sciencedirect.com/science/article/pii/0022201187901157. Publisher: Elsevier.

S. A. Woods, J. S. Elkinton, K. D. Murray, A. M. Liebhold, J. R. Gould, and J. D. Podgwaite. Transmission dynamics of a nuclear polyhedrosis virus and predicting mortality in gypsy moth (Lepidoptera: Lymantriidae) populations. *Journal of Economic Entomology*, 84(2):423–430, 1991. URL https://academic.oup.com/jee/article-abstract/84/2/423/802403. Publisher: Oxford University Press Oxford, UK.

Kai Wu, Bing Yang, Wuren Huang, Leonard Dobens, Hongsheng Song, and Erjun Ling. Gut immunity in Lepidopteran insects. *Developmental & Comparative Immunology*, 64: 65–74, November 2016. ISSN 0145-305X. doi:10.1016/j.dci.2016.02.010. URL https://www.sciencedirect.com/science/article/pii/S0145305X16300349.

Yuling Yao, Aki Vehtari, Daniel Simpson, and Andrew Gelman. Using Stacking to Average Bayesian Predictive Distributions (with Discussion). *Bayesian Analysis*, 13(3):917–1007, September 2018. ISSN 1936-0975, 1931-6690. doi:10.1214/17-BA1091. URL https://projecteuclid.org/journals/bayesian-analysis/volume-13/issue-3/Using-Stacking-to-Average-Bayesian-Predictive-Distributions-with-Discussion/10.1214/17-BA1091.full. Publisher: International Society for Bayesian Analysis.

Luke A. Yates, Zach Aandahl, Shane A. Richards, and Barry W. Brook. Cross validation for model selection: A review with examples from ecology. *Ecological Monographs*, 93(1):e1557, 2023. ISSN 1557-7015. doi:10.1002/ecm.1557. URL https://onlinelibrary.wiley.com/doi/abs/10.1002/ecm.1557. _eprint: https://onlinelibrary.wiley.com/doi/pdf/10.1002/ecm.1557.

Yinong Young-Xu and K. Arnold Chan. Pooling overdispersed binomial data to estimate event rate. *BMC Medical Research Methodology*, 8(1):58, August 2008. ISSN 1471-2288. doi:10.1186/1471-2288-8-58. URL https://doi.org/10.1186/1471-2288-8-58.

QinQin Yu, Joao Ascensao, Takashi Okada, The COVID-19 Genomics UK (COG-UK) consortium, Olivia Boyd, Erik Volz, and Oskar Hallatschek. Lineage frequency time series reveal elevated levels of genetic drift in SARS-CoV-2 transmission in England. preprint, Evolutionary Biology, November 2022. URL http://biorxiv.org/lookup/doi/10.1101/2022.11.21.517390.